Super-Kamiokande Atmospheric Neutrino Analysis
of Matter-Dependent Neutrino Oscillation Models

Kiyoshi Keola Shiraishi

A dissertation submitted in partial fulfillment
of the requirements for the degree of

Doctor of Philosophy

University of Washington

2006

Program Authorized to Offer Degree: Physics

University of Washington
Graduate School

This is to certify that I have examined this copy of a doctoral dissertation by

Kiyoshi Keola Shiraishi

and have found that it is complete and satisfactory in all respects,
and that any and all revisions required by the final
examining committee have been made.

Chair of the Supervisory Committee:

_____

R. Jeffrey Wilkes

Reading Committee:

_____

R. Jeffrey Wilkes

_____

Thompson Burnett

_____

Ann Nelson

_____

Cecilia Lunardini

Date: _____

In presenting this dissertation in partial fulfillment of the requirements for the doctoral degree at the University of Washington, I agree that the Library shall make its copies freely available for inspection. I further agree that extensive copying of this dissertation is allowable only for scholarly purposes, consistent with "fair use" as prescribed in the U.S. Copyright Law. Requests for copying or reproduction of this dissertation may be referred to Proquest Information and Learning, 300 North Zeeb Road, Ann Arbor, MI 48106-1346, 1-800-521-0600, to whom the author has granted "the right to reproduce and sell (a) copies of the manuscript in microform and/or (b) printed copies of the manuscript made from microform."

Signature_____

Date_____

University of Washington

Abstract

Super-Kamiokande Atmospheric Neutrino Analysis
of Matter-Dependent Neutrino Oscillation Models

Kiyoshi Keola Shiraishi

Chair of the Supervisory Committee:
Professor R. Jeffrey Wilkes
Physics

Current data finds that the atmospheric neutrino anomaly is best explained with $\nu_\mu - \nu_\tau$ neutrino oscillations. However, there is motivation for the Mass Varying Neutrino (MaVaN) model as an explanation for the presence of dark energy and the results of LSND. A possible consequence of said model is a bias in the neutrino mass from the electron density ρ_e of the matter a neutrino passes through. Using the data from Super-Kamiokande-I, $\nu_\mu - \nu_\tau$ oscillation models whose mass differences are proportional to $(\rho_e)^n$ are applied to the Monte Carlo predictions for several different n values. A constant mixing angle in all densities is assumed. For each density dependence hypothesis, two sets of models are applied, which do not or do account for the air pathlength. In all of the specific models tested, the density dependent oscillations are disfavored at greater than a 3σ level compared with 2-flavor oscillations with a fixed mass in all environments. In addition, a separate analysis which assumes maximal mixing finds that a best-fit 2-flavor oscillation of varying density dependence is consistent with no dependence on electron density within 1σ.

TABLE OF CONTENTS

LIST OF FIGURES

LIST OF TABLES

GLOSSARY

BARTOL: A common model of the atmospheric neutrino flux, also referenced in here as "Gaisser".

CMB: Cosmic Microwave Background. Microwave radiation that permeates the universe believed to be left from the Big Bang.

FC: Fully-Contained event in Super-K, defined by the initial and stopping vertex of the neutrino event being within the fiducial volume.

FLUKA: Another common model of the atmospheric neutrino flux.

FV: Fiducial Volume, the effective volume for the contained events. It is defined such that the initial vertex is at least 2 meters from the inner detector wall. In Super-K this amounts to 22.5 kiltons.

GEANT: A program developed at Cern to describe elementary particles through matter.

GZK: Greisen-Zatsepin-Kuzmin limit. A theoretical cutoff for cosmic rays with energies greater than 5×10^{19} eV produced outside the galaxy.

HDM: High-Density Material. A loose term used to encompass solids and liquids, referring to the environment of the neutrino pathlength.

HONDA: Another common model of the atmospheric neutrino flux.

ID: Inner Detector of Super-K. It is a concentric cylinder within the tank whose structure is 38.2 meters high by 35.8 meter diameter.

IMB: Irvine-Michigan-Brookhaven detector, an earlier water Cherenkov neutrino detector.

KAMIOKANDE: Kamioka Nucleon (Neutrino) Decay (Detector) Experiment. The predecessor to Super-K which was a smaller water Cherenkov detector.

MACRO: Monopole and Cosmic Ray Observatory, a multipurpose detector which included atmospheric muon neutrinos.

NEUT: The primary program used by Super-K, designed to simulate nuclear interactions.

NUANCE: Another program designed to simulate nuclear interactions.

OD: Outer Detector of Super-K. The shell structure surrounding the inner detector with about a 2 meter thickness.

PC: Partially-Contained event in Super-K, defined by the initial vertex of the neutrino interaction being within the fiducial volume, with enough energy to leave the inner detector volume.

PMT: Photomultiplier tube. A type of extremely sensitive light detector used by Super-K to detect Cherenkov light.

PREM: Preliminary Reference Earth Model.

PULL METHOD: A chi-squared hypothesis testing method which separates the systematic error terms in order to see which error has significant "pull" on the chi-squared value.

QTC: Charge-to-Time Converter. A module that transformed the PMT signals into ones readable by TDCs.

SK/SUPER-K: Super-Kamiokande.

SK-I: Super-Kamiokande data period lasting from April 1996 until July 2001.

"STANDARD" OSCILLATIONS: Refers to 2 flavor $\nu_\mu - \nu_\tau$ oscillations with a fixed mass-squared difference in all environments, including air.]

STOPMU: A muon created outside of the inner detector which comes to a stop within it.

TDC: Time-to-Digital Converter. A module used for reading PMT signal information.

THRUMU: A muon created outside of the inner detector with enough energy enter and exit the ID.

UPMU: A muon created outside of the inner detector that traverses into the ID with an upward direction coming from below the horizon. Super-K data only uses upmus to eliminate cosmic ray muon contamination.

USGS: United States Geological Survey.

WMAP: Wilkinson Microwave Anisotropy Probe. A NASA satellite that measures radiant heat from the Big Bang.

ACKNOWLEDGMENTS

It is impossible to record every person who deserves an acknowledgement within the confines of this space. Given the chance, this section would probably be the longest and most detailed among the entire dissertation, while at the same time surely be missing some key figures. Although I only highlight a few, believe me when I write that there have been many others whose contributions, however small and forgettable they may seem, have been noted and appreciated by me.

I would like to start by thanking my advisor, Jeff Wilkes, who has done more for me than he probably realizes. He took a local boy from Hawaii and gave him a chance to do physics and much, much more. His teachings, both direct and indirect, have been instrumental to becoming the researcher I am today. Without his encouragement this dissertation would not have been finished.

John Learned was in many ways, my second advisor. My physics growth has benefited significantly from his aid, and I always enjoyed his physics stories and dedication for doing good science. He and the Hawaii group welcomed me whenever I was in Oahu, and to all of whom I give thanks.

I am obliged to the members of my committee for their challenging questions and useful feedback: Jeff, Toby Burnett, Ann Nelson, Paula Heron, and especially Cecilia Lunardini, who taught me more neutrino physics than I could retain, sadly. Neal Weiner, Rob Fardon, Kathryn Zurek, and Kregg Philpott have also contributed valuable aspects to this analysis.

All of the members of the Super-K group have been great to work with and I must thank them for the constant help and information. Takaaki Kajita and Ed Kearns were crucial sources of guidance and understanding the analysis and results. Choji Saji and Hyun Kwan Seo were so kind to answer my many questions about the upmu reduction. Alec Habig has always been a consistent resource for Super-K and computing information. And the many graduate students (Wei Wang, Fumi Kato, Parker Cravens, the BU, SUNY, and UCI groups) were always great company for yakiniku.

Here at UW I have been fortunate enough to work with a terrific group of researchers. Rik Gran padawan'd me into a research scientist with tools I can forever take with me. Andy Stachyra gave

me a solid foundation of Unix and upmus to build on. Hans Berns is not only a great engineer to work with but also an excellent guide while traveling in Japan. Kristine Washburn had shared many same highlights and lowlights of doing research, but always pointed out the great life outside of school. Eric Thrane has been a wonderful conversationalist on every subject, and a fountain of knowledge to the physics behind the computer code. Each assisted in raising my social and research time in Seattle.

On a more personal note, my family has always been a strong source of support and love. Without them I could never have made it this far, and through them I know I have been Blessed. Although I rarely call, I never forget. Thank you.

The PC boys, UPS posse, the SJJC, and the Yahulagans who all kept me sane: They all took me in so many times and never once treated me like a physics student. I owe them an enormous debt of gratitude.

There are thousands more who should be on this list, for their kind words, homework notes, interest in my work and well-being, and pleasant distractions. Thanks to every one of them for helping me get to this point.

Lastly, I cannot forget Kym Yano for her never ending support, encouragement through the rough times, and reminders of the bigger picture. For it all, I am truly grateful.

Chapter 1

ATMOSPHERIC NEUTRINOS

1.1 Introduction to the Neutrino

It all started with beta decay.

$$n \rightarrow p + e^-$$

What should have been a simple process instead raised questions. For a neutron at rest, the emitted electron should have a monoenergetic spectrum in the two body decay. Instead, physicists measured a continuous energy spectrum for this process (Fig. 1.1). There was an additional problem with a lack of spin conservation as neutrons, protons, and electrons each have spin $\frac{1}{2}$. In 1930, W. Pauli postulated a solution: a undetected missing piece that had spin $\frac{1}{2}$ and carried away the missing energy. For it to have been undetected, it must have had no electrical charge and a negligible mass. Pauli first called this hypothesized particle a "neutron", though E. Fermi later renamed the little neutral particle the neutrino, with symbol ν. Though Pauli initially felt guilt for "making up" a solution, the neutrino was eventually found, although discovery of this particle would not occur until 1956 by C. Cowan and F. Reines [38], nearly three decades after its prediction.

1.1.1 What is a Neutrino?

Today the neutrino is known as one of the fundamental particles belonging to the lepton family. It has quantum spin number $\frac{1}{2}$, a negligible mass compared to the other elementary particles (negligible gravitational interactions), no electromagnetic charge (no Coulomb interactions), nor does it have any baryonic charge (no strong interactions). It couples with particles via the weak interaction. There are three known types, or flavors of neutrinos that are each associated with a corresponding member of the lepton family: an electron neutrino, a muon neutrino, and a tau neutrino, who each have its own antiparticle. As a lepton, it has a particular lepton number that is conserved in weak
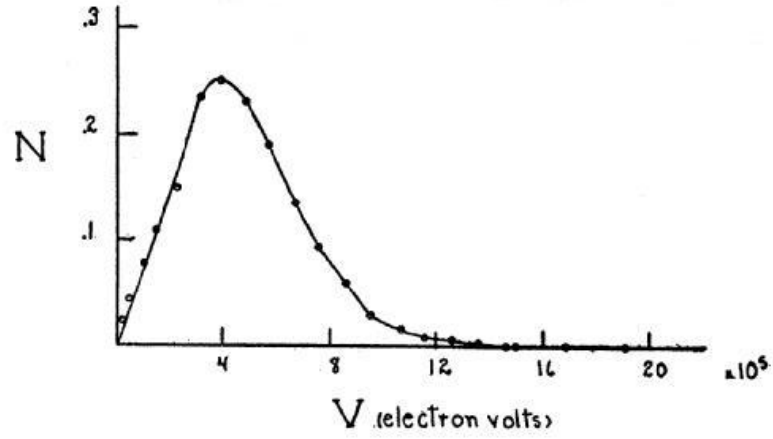
Figure 1.1: Energy distribution curve of beta rays [86]

interactions. Electrons (positrons) and electron (anti)neutrinos have electron number $L_e = +1(-1)$. For all other leptons $L_e = 0$. Muons and Taus and their neutrino counterparts have similar values for L_μ and L_τ. This means is that an electron cannot be produced without an incident electron or electron neutrino, or else additionally producing a positron or electron antineutrino, conserving the lepton numbers.

$$n \quad \rightarrow \quad p + e^- + \overline{\nu_e}$$
$$L_e = 0 \quad \rightarrow \quad 0 + 1 \quad +^- 1$$

Of the three types of neutrinos physicists now believe that at least two have non-zero masses (this will be explained more in Chapter 7). This is in contrast to the Standard Model prediction that neutrinos have zero mass. β-decay experiments that observe the distortion of the energy spectrum due to having a non-zero neutrino mass limit the electron neutrino mass to be less than 2.8 eV/c^2 [96]. Other decay-type experiments constrain the mass of a muon neutrino is less than 170 keV/c^2 [16] and the mass of the tau neutrino to be less than 15.5 MeV/c^2 [84] [1]. Cosmological results also puts a limit on the sum of the three neutrino masses. The Wilkinson Microwave Anisotropy Probe

[1] At 95% C.L.

(WMAP) has led to predictions that the sum of the neutrino masses $\sum m_\nu < 0.42$ eV [87] [1].

When Pauli first postulated the particle, he criticized himself for creating an answer he felt would never be discovered. And it took thirty years to find after it was predicted, because it is only weakly interacting and has a relatively small mass which make it difficult to detect. Yet one fact made neutrino detection physics a possible endeavor: sheer abundance.

1.1.2 *Where do neutrinos come from?*

On average, about a ten trillion neutrinos per second pass through a cubic centimeter on Earth, which come from a number of different sources [5]. Local sources include nuclear accelerators that produce neutrinos for physics experiments. Nuclear reactors are another terrestrial source of neutrinos which are a byproduct of the fission process, some reactors producing over 10^{20} neutrinos per second. Nuclear bombs also produce neutrinos and were once considered for a detector experiment (but were never used as a source). The Earth has a flux of 6×10^6 cm^{-1}s^{-1} neutrinos from geological neutrinos from natural radiation. Within the galaxy, a star (like the sun) produces a large number ($\approx 5 \times 10^6$ cm^{-1}s^{-1}) of neutrinos in fusion processes. The galaxy has relic neutrinos left over from supernova bursts (6×10^{58} over ten seconds) and the formation of the universe during the Big Bang (110 cm^{-3} density). However, this dissertation will focus on the neutrinos that are produced in the Earth's upper atmosphere as a result from cosmic rays.

1.2 **Atmospheric neutrinos**

1.2.1 *Cosmic Rays*

The Earth is constantly being bombarded with particles from outside its atmosphere, generically called cosmic rays. Discovered by Victor Hess in 1912, they are primarily protons and alpha particles, but also include heavier nuclei, electrons, positrons, photons, and neutrinos. However, their charged nature makes them subject to magnetic fields in the galaxy which make cosmic rays isotropic, which makes it impossible to locate the origin of a particular cosmic ray. The primary sources of cosmic rays from within the galaxy are believed to be supernovas: supernova explosions, magnetospheres of pulsars following an explosion, young envelopes of the supernova, and shock waves can all accelerate nuclei. They are also be accelerated by stars; and the sun is a nearby source

that creates cosmic rays. Ultrahigh energy ($10^{17} - 10^{19}$ eV) cosmic rays are thought to come from extragalactic sources, such as active galactic nuclei [27].

The cosmic ray energy range spans 14 orders of magnitude (see Figure 1.2). Energies from 10 to 10^6 eV follow a power law spectrum $I_p(E) = E^{-\gamma_P}$, where $\gamma \approx 2.7$ [89]. The spectrum changes above 3×10^6 eV, where it becomes steeper to $\gamma = 3.2$. This is known as the "knee". The spectrum changes again at the "ankle", 5×10^{18} eV, where it flattens to $\gamma = 2.8$. After this, the Greisen-Zatsepin-Kuzmin (GZK) cutoff predicts no cosmic rays above 5×10^{19} eV [52, 99]. Instead, extragalactic cosmic rays more than 50 MPc away will interact with cosmic microwave background (CMB) photons to produce pions of lower energy. No such sources of such rays are seen within that boundary, but several experiments, most notably Fly's Eye [32] and AGASA [54] have detected events above this limit.

Low energy cosmic rays ($E_{cr} \leq 10$ GeV) are affected by solar wind. High solar activity results in
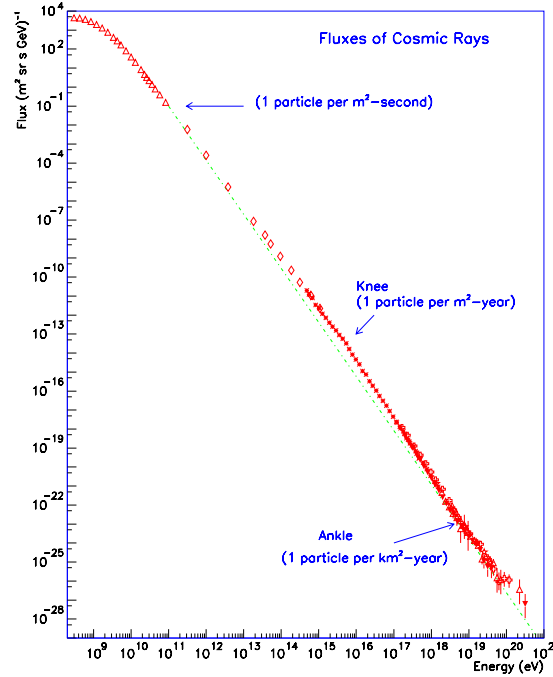
Figure 1.2: Cosmic ray spectrum [89].

a smaller primary flux, and vice versa. The Earth's magnetic field also limits the low energy flux.

To pass through to the Earth's surface, a cosmic ray must have high rigidity (momentum per unit charge) to not be deflected by the Earth's magnetic field. The deflection is higher for eastern directions than for western directions due to the Coulomb force, and a higher cosmic ray flux is expected from the west. Cosmic rays with energies greater than $100\,\mathrm{GeV}$ ($10\,\mathrm{GeV}$ neutrinos) are not affected by the rigidity cutoff or solar activity.

1.2.2 Atmospheric Neutrino Creation

The Earth's atmosphere acts as a shield against cosmic rays, and most never reach the Earth's surface. Approximately 15 km above the surface of the Earth cosmic rays collide with nuclei in the atmosphere to produce pions and kaons. The atmospheric neutrino source are these unstable mesons that eventually decay and produce neutrinos:

$$
\begin{aligned}
\pi^+ &\rightarrow \nu_\mu + \mu^+ \\
&\rightarrow \nu_\mu + (\, e^+ + \nu_e + \overline{\nu_\mu}) \\
\pi^- &\rightarrow \overline{\nu_\mu} + \mu^- \\
&\rightarrow \overline{\nu_\mu} + (\, e^- + \overline{\nu_e} + \nu_\mu)
\end{aligned}
$$

Kaons decay into pions or muons and muon antineutrinos.

The atmospheric neutrino flux falls rapidly as $KE^{-\gamma}$ for $\gamma \approx 3.8$ above $10^4\,\mathrm{GeV}$ [89] (see Fig. 1.3).

1.2.3 The Atmospheric Neutrino Ratio

The ratio of total atmospheric muon-flavor neutrinos and antineutrinos to electron-flavor neutrinos and antineutrinos near the surface of the Earth is expected to be roughly $2:1$ at low energies. Most particles with less than 10 GeV decay to neutrinos before interacting again with the atmosphere. As the energies get larger, the probability of interacting increases due to its longer spatial life. At the highest energies, the secondary decay products of a kaon with sufficient energy may not decay before reaching the surface. This may also happen with secondary muons of sufficient energy. These effects increase the expected counts of ν_μ relative to ν_e, and the muon-electron neutrino ratio gets shifted to larger than 2 (see Fig. 1.4). While there are inconsistencies between predicted flux models,
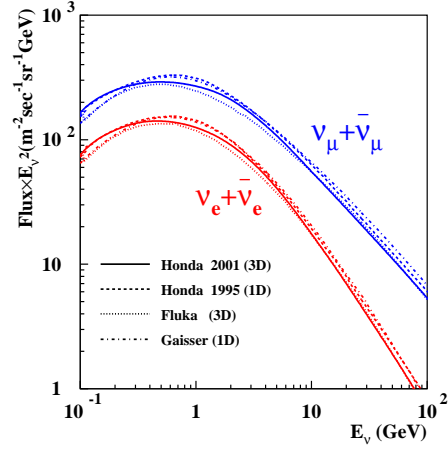
Figure 1.3: Average neutrino flux for various neutrino flux models [61, 58, 24, 22].

taking the ratio of muon neutrino / electron neutrino data over a Monte Carlo expected predictions of the ν_μ/ν_e ratio cancels some of the uncertainties. This double ratio of ratios is often referred to as R (Equation 1.1).
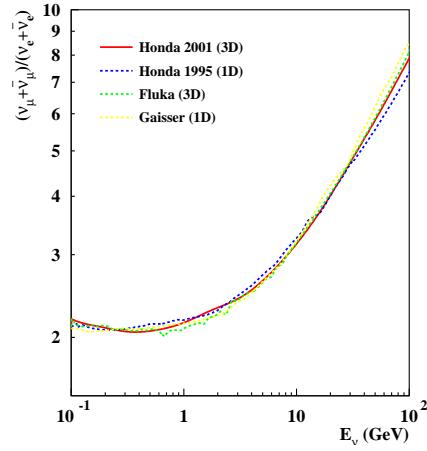
Figure 1.4: The flux ratio for several different models is shown [61, 58, 24, 22].

$$R \equiv \frac{R_{DATA}}{R_{MC}} \equiv \frac{(N_\mu/N_e)_{DATA}}{(N_\mu/N_e)_{MC}} \equiv \frac{(\nu_\mu + \overline{\nu_\mu})/(\nu_e + \overline{\nu_e})_{DATA}}{(\nu_\mu + \overline{\nu_\mu})/(\nu_e + \overline{\nu_e})_{MC}} \qquad (1.1)$$

1.3 Atmospheric neutrino experiments before Super-Kamiokande

1.3.1 The First Atmospheric Neutrino Detectors

- IMB

  The Irvine-Michigan-Brookhaven detector was a 8 kiloton water Cherenkov detector built in the Morton-Thiokol salt mine in Ohio, on the shores of Lake Erie. It began in the early 1980's and ran until 1991. Though originally designed to search for and set new limits on proton decay, it was also found to be a capable neutrino detector. It had 2048 photomultiplier tubes which,when the experiment ended, were removed and put to use in the outer detector of Super-Kamiokande.

- KamiokaNDE

  The Kamioka Nucleon Decay Experiment began in July 1983 and was a 3 kiloton water Cherenkov detector built in a mine in Mozumi, Japan. It had about 1000 photomultiplier tubes on its inner surface. Its first task was to also search for proton decay before it got into neutrino detection. After not having detected any proton decays, it re-acronymed itself the Kamioka Neutrino Detection Experiment. Eventually a desire for greater statistics and resolution led to the construction of Super-Kamiokande.

- Soudan II

  The Soudan detector was an iron calorimetry experiment in the Soudan iron mine in Soudan, Minnesota. Within a 960 ton iron calorimeter was a honeycomb array of drift tubes which provide hit reconstruction. Surrounding the entire calorimeter is an active shield veto structure. It was fully completed in 1993 and continued to run until 2002. Like the others, it began with searches for proton decay but ended up using its data for neutrino analysis.

- MACRO

  The Monopole Astrophysics and Cosmic Ray Observatory was located in the Gran Sasso underground physics laboratory(Laboratori Nazionali del Gran Sasso) in Abruzzo,Italy. The detector itself was an array of vertical and horizontal streamer tubes which allowed for particle tracking. These streamers were alternated with layers of rock and iron and surrounded by

tank of liquid scintillator. The scintillator provided the timing on each events to determine an upward or downward direction of the particle. It began its science searching for magnetic monopoles but could use its data to count upward going muons caused by neutrino interaction from underneath the detector.

1.3.2 Neutrino Ratio Results before Super-K

The neutrino double ratio results of the aforementioned experiments are shown in Table 1.1. Each detector had independently discovered that the double ratio of $\frac{\nu_\mu}{\nu_e}$ was measured to be much less than unity, meaning the prediction was too large compared to data. The experiments, using various methods, each detected too few muon-type neutrinos or too many electron type neutrinos. [2] (MACRO, which only detected muons, pointed to the former.) While there were several theories as to why there was this atmospheric neutrino anomaly, no reason was statistically significant until the evidence from Super-Kamiokande.

Table 1.1: Various double ratios R values for experiments prior to Super-Kamiokande.

Experiment	Energy Range	R (double ratio)
IMB [35] [25] [37]	Sub-GeV	$0.54 \pm 0.05 \pm 0.12$
	Multi-GeV	$1.40 \pm^{0.41}_{0.30} \pm 0.3$
Kamiokande [48] [56] [57]	Sub-Gev	$0.60 \pm^{0.06}_{0.05} \pm 0.05$
	Multi-Gev	$0.57 \pm^{0.08}_{0.07} \pm 0.07$
Soudan II [85]		$0.69 \pm 0.10 \pm 0.06$
MACRO (ν_μ's only) [7]		0.60 ± 0.07

---

[2] There were also experiments (Frejus [39], Nusex [1]) that did not find a deviation from unity in R.

Chapter 2

SUPER-KAMIOKANDE DETECTOR OVERVIEW

The Super-Kamioka Neutrino Detector Experiment (Super-K, or SK) is a water Cherenkov experiment which began its data taking on April 1st, 1996. As a true successor of Kamiokande, it has the same shape, electronics, and nearly the same custom inner detector photomultiplier tubes. It detects neutrinos via the following: A neutrino enters the detector and interacts with nuclei to generate a particle (usually a electron or muon). This charged particle moves at very high speeds and emits Cherenkov radiation. Special light sensors called photomultiplier tubes (PMTs) are situated within Super-K to detect this light cone and infer the energy and direction of the original parent neutrino. This makes it a "real-time detector", meaning the data can be seen instantly.

Super-K is used for a number of physics experiments. In addition to being a atmospheric neutrino detector, it is a solar and supernova (current and relic) neutrino detector, and also searches for proton decay. Its detection of cosmic ray muons is used to study the cosmic ray flux. Its large surface area and sensitivity is used as a neutrino telescope for astronomy. It also serves as a far neutrino detector for the KEK-to-Kamioka (K2K) experiment.

2.1 Physical Attributes of SK

It is located in the same Kamioka Mining and Smelting Company's zinc mine that its predecessor Kamiokande was built (though at a slightly different location). Deep within Mt. Ikeno in the Gifu prefecture, it has an average of 1000 meters of rock under the peak, or about 2700 meters of water equivalent (mwe), to shield it from background cosmic rays. The geographic location of the center is at $36° 25'$ N and $137° 18'$ E. The detector itself is a cylindrical tank of 41.4 meters high and a 39.3 meter diameter. The primary difference between Kamiokande and Super-K is its size; Kamiokande held only 2.14 kilotons of water but Super-Kamiokande's super bulk holds 50 kilotons with a 22.5 kiloton fiducial volume, making it the largest water Cherenkov detector at the time of this writing. The detector cavern is supported by iron rods and about 50 centimeters of concrete. The area and
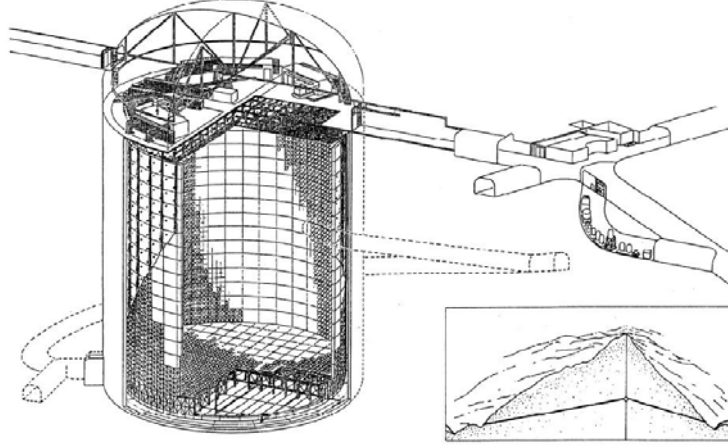
Figure 2.1: Schematic view of Super-Kamiokande. Inset shows cutaway view of the Mt. Ikeno.

tunnel are covered in a Mineguard polyurethane to help seal out radon gas from the mountain. Above the detector tank are five huts that hold the front end electronics for the inner and outer detector PMTs. Along the inner surfaces of the tank are 26 Helmholtz coils to reduce the magnetic field to 50 mG to enhance PMT performance.

2.2 Cherenkov Effect

Super-Kamiokande detects a particle by the Cherenkov light it emits in the water. This effect was discovered in 1934 by P. Cherenkov.

A moving charged particle emits electromagnetic radiation (See Fig 2.2). If the particle is moving at greater than the speed of light in the medium($v = c/n_{water} = \frac{3 \times 10^{*8}}{1.33} \approx 2.26 \times 10^8$ m/s in water,) there becomes a buildup of the radiation at an angle $\cos \theta = \frac{c/n_{water}}{\beta c}$, ($\beta = v_{particle}/c$,). This eventually becomes a radiation shockwave, much like a sonic boom or a boat's wake, but in the form of a light cone.

A neutrino, being nearly massless, is relativistic. Super-Kamiokande's large water capacity creates a medium for the Cherenkov light. When the neutrino interacts with nuclei in the water, it can generate a charged lepton with enough energy to Cherenkov radiate. When such a lepton travels
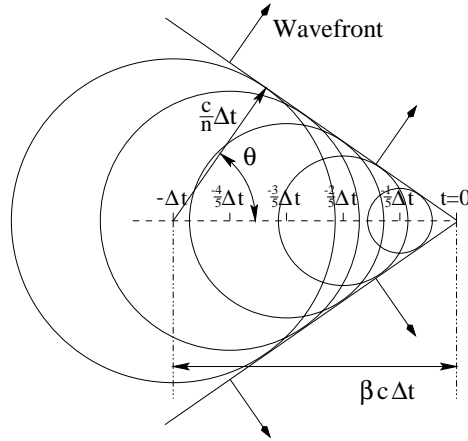
Figure 2.2: A diagram of Cherenkov light propagation [92]. The circles represent light emission from the particle at successive times, which propagate at a speed c/n. The particle is moving faster than the photons which begin to pile up on each other to form a shock front.

through Super-K, the emitted light is detected by its large, numerous PMTs. Since the cone of light is emitted at a fixed angle relative to the direction of travel, the timing and charge distribution of the PMT light map can determine the direction of a high energy charged particle's direction of travel, as well as an estimate of its energy. By knowing the direction of the moving lepton, the incoming neutrino direction can be inferred, since the scattered particle's direction is roughly parallel to the incoming neutrino. The accuracy of the direction and energy estimation depends on the neutrino's energy and detection type, and more details as to how this is modeled is in Chapter 3.

2.3 The Inner and Outer Detectors

To insure that events in Super Kamiokande are truly from neutrinos, Super-Kamiokande has a cy-clindrical structure within the water that supports the phototubes and optically divides two sections: an inner detector with PMTs that detects the light within the core of the cylinder, and an outer detector whose PMTs make up the outer boundary to detect any light surrounding the cylinder. The primary function of the outer detector is to act as a veto counter, tagging inward and outward going particles as they pass through the detector. A particle generated outside the detector will have telltale light in the outer detector before reaching the inner detector. The importance of this is discussed in

Chapter 3.
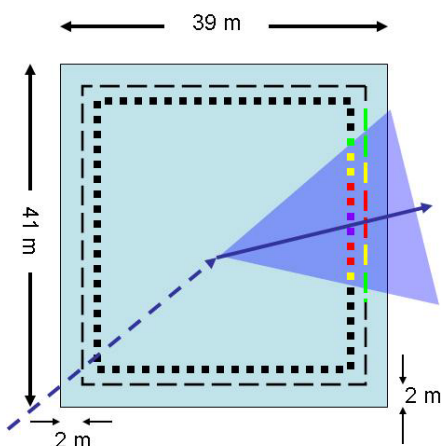
Figure 2.3: Diagram of the Super-Kamiokande detector and a neutrino event. The neutrino here (dashed blue line) comes in from the lower left. It interacts within the detector and produces a charged particle (solid blue line) and emits a light cone. The Cherenkov light is picked up from the inner detector first (dotted inner cylinder). Then, as the neutrino exits, the light is also detected in the outer detector (dashed outer cylinder) at a later time.

2.3.1   Photomultiplier Tubes

A photomultiplier tube is a very sophisticated and sensitive light detector. When a photon strikes the photocathode which lines the inside of the glass bulb, the cathode emits an electron. This electron is accelerated to a charged dynode, and upon striking the dynode it creates more electrons. There are several dynodes within the tube and this process occurs several times, amplifying the signal of the original photon.

2.3.2   The Inner Detector

The inner detector (ID) makes up the inner concentric shell of Super Kamiokande. Its volume is roughly 34 meters high and has a 36 meter diameter. The inner detector's frame holds 11146 R3600 50 cm inward facing photomultiplier tubes (Fig. 2.4). These large PMTs are custom built by the

Hamamatsu Photonics corporation for use by Super-Kamiokande. Within the ID the PMTs are evenly distributed with 7650 PMTs on the side wall and 1784 each on the top and bottom areas, amounting to a 40.41% coverage of the inner surface area. They are spaced at 70 cm intervals with a layer of black polyethylene terephthalate separating adjacent PMTs.
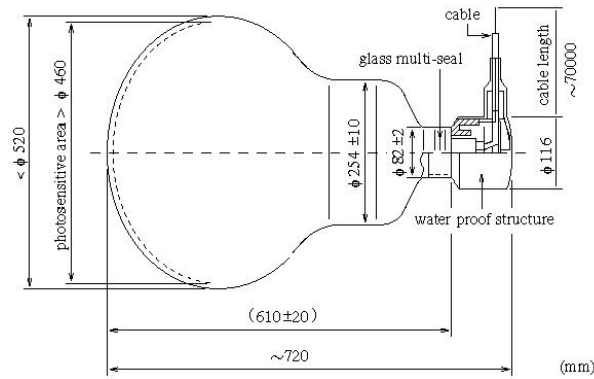
Figure 2.4: Schematic of an inner detector photomultiplier tube

Inner Detector Data Acquisition

The 11,146 PMT signals in the inner detector are connected with one of the four electronic huts that sit in each quadrant above the detector. Each hut contains 12 Tristan-KEK-Online (TKO) crates which utilize a Go/No-Go (GONG) system to distribute the PMT trigger information. The crates also house a bus-interface Super Controller Header (SCH), and 20 Analog Timing Modules (ATMs) that can each handle 12 PMT signals. The ATMs provide 1.2 μs timing with 0.3 nsecond resolution for the PMT signal.

When a PMT is hit over a threshold of about 0.32 eV, the following occurs:

- A 900 nanosecond veto is created on that channel to prevent any after pulsing.

- The PMT generates a square pulse -11 mV in height and 200 ns in width.

- In those 200 ns, the electronics calculates the total signal (called the HITSUM) by adding up any additional signals from all PMT tubes.

- The HITSUM is passed through a discriminator with a threshold of roughly 29 phototubes (about 5-6 MeV.) If successful the signal gets recorded onto the ATM's Super Memory Partner (SMP) to transfer to the online computers. (This signal corresponds to low energy neutrino studies and is a much lower trigger than needed for atmospheric neutrino studies.)

- 8 Sun workstations read this SMP signal via a Bit 3 VME-sbus adapter card. It is then sent to the host computer to be recorded as an event.

The trigger rate in the inner detector is roughly 11 Hz.

More details on the ID ATM modules can be found in [67].

2.3.3 The Outer Detector

The frame of the inner detector has a wall setback of about 2.75 meters and a top and bottom offset of 2.6 meters, making its total volume 32 kilotons. The outer surface of the cylinder consists of 1885 20 cm Hamamatsu R1408 PMTs facing outward, making up the outer detector (OD). They are also equipped with a wavelength shifter plate surrounding each OD tube to increase light coverage and change the wavelength of the radiated light to one the outer detector PMT is more efficient. These wavelength shifter plates delay the signal of the tube from 11 ns to 16 ns but increase the light collection efficiency by 60%. The PMTs are uniformly distributed with 1275 tubes on the sides, 302 tubes on the top and 308 tubes on the bottom. The outer detector is lined with a layer of Tyvek between the PMTs and is over 80% reflective to enhance the outer detector light collection. Each PMT is housed in an inner structure which holds 12 ID PMTs facing inward for every 2 OD PMTs facing outward (See Fig. 2.5).

Outer Detector Data Acquisition

Like the ID, the OD PMT signals and controls are located in the electronics huts. In each electronics hut there is a Fastbus crate which holds 5 LeCroy 1877 multi-hit time-to-digital-converters (TDC). Each TDC has 96 input channels and each of those is connected to the output of a PMT. A PMT
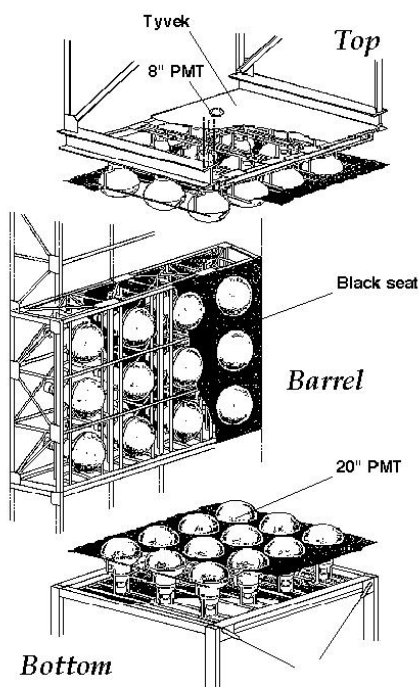
Figure 2.5: Schematic of the structure which holds Super-Kamiokande's inner detector and outer detector PMTs

is fed a high voltage from a LeCroy 1454 mainframe and analog measurements are taken. The channels are in connection to a "paddle card" that distributes high voltage and reads in the signal from 12 PMTs.

When an OD PMT is hit, the following happens:

- The OD signal from the paddle card is fed into a charge to time conversion module (QTC).

- If PMT reading exceeds a trigger of 0.25 photoelectrons (p.e.) equivalent, then the QTC generates a logic pulse which carries timing and charge information to the TDC and an additional 20 mV 200 ns wide pulse to the central hut to generate the OD trigger.

- In that 200 ns window, if the OD trigger exceeds 19 OD PMT signals, then the event gets

recorded.

- There is then a 100 ns pause to see if the ID triggers as well. If there is no ID trigger then the OD will trigger a readout of the detector.

More details can be found in [30].

2.4 Background Reduction Systems

Super-Kamiokande relies on several processes to reduce the number of background in an experiment that has a low signal to noise ratio.

2.4.1 Water Purification System

Ultra pure water in Super-K is essential to reducing background events and minimizing light attenuation in the water. The water purification system takes place over several steps, and is shown in Figure 2.6. First, the water is pumped out and pushed through a 1 μm filter to remove larger particles. It is then cooled down by a heat exchanger to minimize bacteria growth, and then passed through an ion remover. Then it is UV sterilized to kill remaining bacteria followed by the removal of extra gases by a degasifier, and then cartridge polisher then removes remaining ions. Finally, the water passes though an ultra-filter removing particles up to 10 nm. The entire process can filter at a rate of 50 m^3/hour, and keeps the water transparency greater than 70 meters.

2.4.2 Radon Hut

It is necessary that the radon levels in Super-Kamiokande are kept at an absolute minimum to prevent unwanted radiation in the tank. The radon air in the tunnel can vary from about 2000 Bq/m^3 during the summer to about 200 Bq/m^3 during the colder winter months. The difference is attributed to the amount of air flow during those periods. Super-Kamiokande requires radon levels at less than 100 Bq/m^3. Fresh air is constantly pumped at approximately 10 m^3/min from the air surrounding the mountain into the experimental area. The creates a slight overpressure in the detector area which helps minimize entering radon from the mountain rock and water. The radon hut is located at the Atotsu tunnel entrance to the mine and houses most of the mechanics used to pump the outside air.
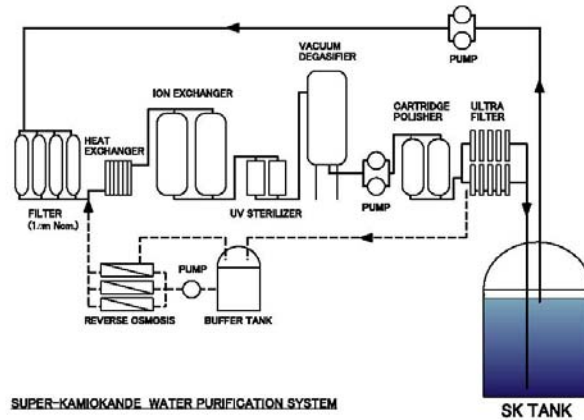
Figure 2.6: Water filtration system of Super-Kamiokande

A diagram of the original radon system is in Figure 2.7. When Super-K begin in 1996 the radon hut initially consisted of an air blower pumping air first through a dehumidifier and then a carbon filter tank before being blown into the mine. This was later changed after the data run used in this analysis.

More details can be found in [29] or in Appendix A for changes made to the radon hut.

2.4.3 Timing System

Each event has two time stamps. The absolute time of an event is measured by a Global Positioning System (GPS) receiver mounted inside the radon hut, and is accurate to within 100 nsec. The signals are sent through the mine tunnel to the center hut above the tank, which is the picked up by two different receivers to transcode the time stamps. In addition, the time between successive events are measured and stamped on events by a 48-bit counter that has an accuracy of about 20 ns. More details of the GPS system can be found in [31].

COMPRESSOR AIR FILTER BUFFER AIR DRIER CARBON HEAT CARBON AIR FILTER AIR FILTER
(0.3μm) TANK COLUMN EXCHANGER COLUMN (0.1μm) (0.01μm)

SUPER-KAMIOKANDE RADON-FREE-AIR SYSTEM
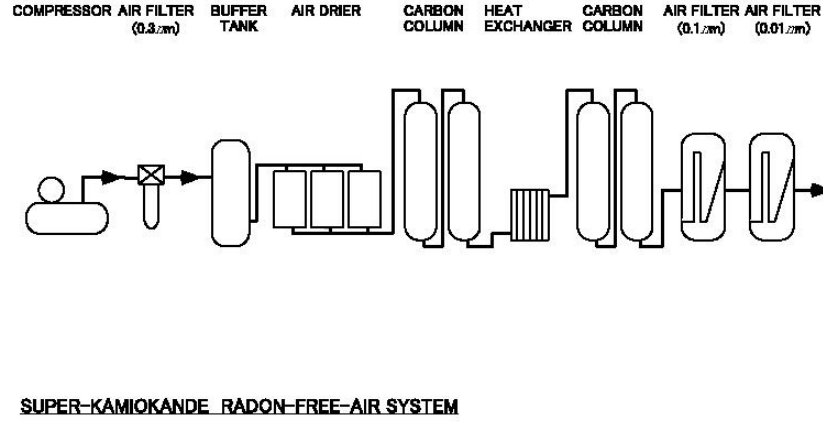
Figure 2.7: Diagram of the original Radon system.

2.5 Calibration of Super-Kamiokande

2.5.1 Relative Gain Calibration of Super-Kamiokande

The high voltage of the ID PMTs must be calibrated so that each PMT measures the same "charge", after taking into consideration the light acceptance, attenuation, and isotropy. Each PMT is initially gain measured before installation by Hamamatsu, but possible shifts in their calibration require secondary testing. A diagram of the relative gain system is in Figure 2.8. Calibration of the inner detector PMT gain is done with a Xenon lamp. Xenon light is passed through an UV filter to an acrylic ball via an optical fiber. The acrylic ball is doped with BBOT scintillator and MgO powder which allows it to absorb the UV light and re-emit in the blue-green range similar to that of Cherenkov light. The ball is lowered into Super-K and monitored with a 2-inch PMT that is used to trigger the calibration events. After being corrected for light attenuation, acceptance, and source uniformity, the high voltages for each PMT are set so that all charge acceptances are the same. Several measurements are made at differing levels of depth of the ball in the tank and high voltage used.

More details can be found in [67].
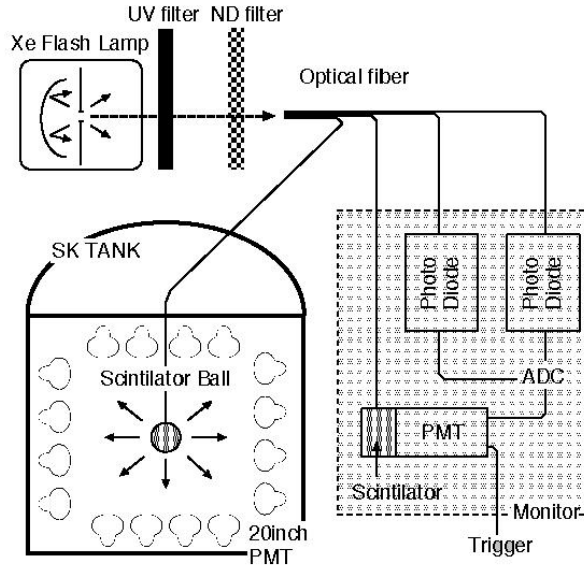
Figure 2.8: Relative gain measurement system

2.5.2 Absolute Gain Calibration of Super-Kamiokande

Super-K must also determine how much each photoelectron signal in the PMT corresponds to in terms of photon energy. To calibrate a PMT at the single photoelectron level a Nickel-Californium setup is used. A Californium source produces neutrons which interact with the Nickel and primarily produce gamma rays of 9.0 MeV. This low energy photon most commonly results in a PMT reporting a single photoelectron and so the response of each PMT can be used to calibrate the level of photoelectrons to charge. It is approximately 2 pC to 1 photoelectron.
More details can be found in [67].

2.5.3 Timing Calibration of Super-Kamiokande

There is also a system to help set up the timing of each PMT. A diagram of the timing system is in Figure 2.9. A Nitrogen laser (at wavelength $\lambda = 337$ nm) goes through a dye-module to shift the wavelength closer to that of Cherenkov light. An optical filter varies the intensity of the light, which then passes it though a beam splitter. One signal goes to a diffuser ball within the detector,

and the other goes to a monitor PMT which is used to set the trigger. The diffuser ball is made up of TiO_2 on the end of a fiber optic, and is encased by a material called LUDOX, a silica gel with tiny glass fragments. This system produces diffuse light over a small time window. Each PMT hit is recorded as a function of charge, and this method determines the average time offset. The high charge PMT hits are relatively earlier and have better timing resolution compared to their low charge counterparts. A table called a TQ (Time-Charge) map is constructed from the data and used to correct ID hit times according to the charge values.

More details can be found in [67].
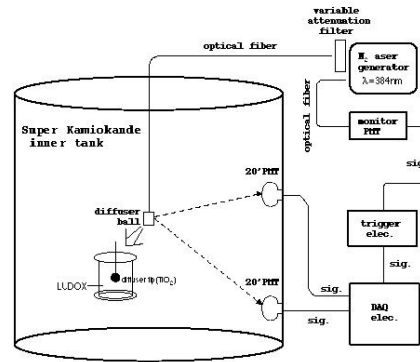
Figure 2.9: Laser timing measurement of ID PMTs

2.5.4 Water Transparency Calibration

Knowing the clarity of the water is needed to properly understand each event, because as photons travel through the water their intensity falls like an exponential. A diagram of the water transparency system is in Figure 2.10. Calibration of this attentuation is done by laser light and by cosmic ray muon events. A similar laser-dye setup like the one mentioned in the timing measurement is also used here. The light is split into two signals, where one is used for triggering and the other sent into Super-Kamiokande's tank. The light from the diffuser ball in the tank is captured using a CCD camera near the top. This is repeated for various depths of the light source in Super-Kamiokande,

and the intensity is fitted as an exponential:

$$\frac{\text{Intensity}_{CCD}}{\text{Intensity}_{MonitorPMT}} = Ae^{\left(-\frac{distance}{L(\lambda)}\right)}. \tag{2.1}$$

There is also a method that uses decay electrons and penetrating muons from cosmic rays as an indirect measurement of the water transparency, but that will not be discussed here.

Further details can be found in [67].
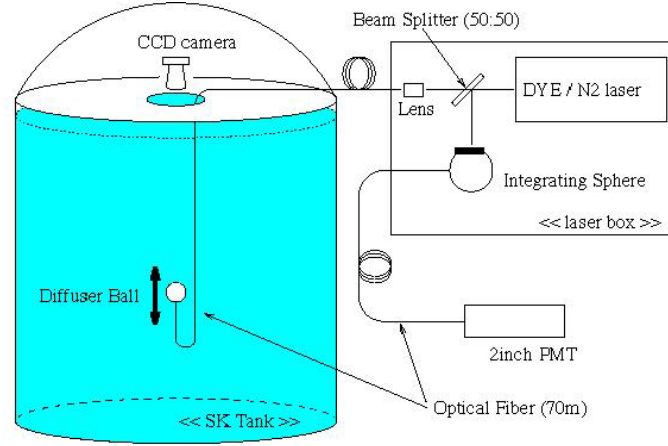
Figure 2.10: Water transparency measurement system

Details to the entire Super-Kamiokande detector, its mechanisms and calibrations are written in detail in [49].

Chapter 3

MONTE CARLO MODELING AND EVENT RECONSTRUCTION

To get accurate neutrino counts, Super-K must understand the interactions in the detector. This involves knowing how many neutrinos pass through the detector, the likelihood of a neutrino interaction within the detector, and the resulting effects of different neutrino interactions. In its analysis SK mimic neutrino events in SK by a Monte Carlo simulation with a series of programs.

3.1 Neutrino Flux

The atmospheric neutrino flux caused by the cosmic ray interactions and decay of the secondary particles is modeled by several different groups. Super-Kamiokande's primary analysis uses the 3-dimensional HONDA flux [61], which is specifically designed for the Kamioka site, but also consideres other flux models (HONDA 1D [58, 60], FLUKA 3D [24], Gaisser 1D [22]) as a cross check in its analysis. For low energies, the primary cosmic ray fluxes are calculated separately for solar minimum, solar maximum, and average to account for solar wind. A rigidity cutoff is also applied. In addition, there is a higher flux expected for neutrinos coming in from near the horizon compared to neutrinos traveling from directly above. Horizon neutrino parent mesons spend more time traveling in a less dense atmosphere in which they are more likely to decay. The effect is more significant for lower energy neutrinos and taken into account in the HONDA 3D model, which employs 3-dimensional methods that treat the secondary particles traveling at a different direction than the incident cosmic ray. (Prior 1-D flux models assumed parent mesons and child neutrinos traveled in the same direction.)

There are difficulties in knowing the exact neutrino flux. The hadronic interactions that create atmospheric neutrinos are not well understood. Agreement between the flux models is within 10% due to the 5% accuracy of the cosmic ray flux and use of different hadronic models. This agreement is worse for neutrinos above 10 GeV. A larger error comes from the normalization of the absolute flux, with an uncertainty approximately 20% [58, 2, 46]. However, calculating the flux ratio of ν_μ to

ν_e cancels out many differences between models and reduces the uncertainty. A comparison of the different flux models can be seen in Figure 1.3.

3.2 Neutrino Interactions within Super-Kamiokande's Inner Detector

As an atmospheric neutrino passes through Super-K, there is a chance that it will interact with the water in the detector by a number of methods.

3.2.1 Weak Nuclear Scattering

There are two possible neutrino weak interactions that take place within Super-Kamiokande (see Figure 3.1):

Neutral Current A neutral current (NC) interaction occurs when a neutrino exchanges an electrically neutral Z_o boson to scatter off an electron that moves relativistically and generates Cherenkov light. All three flavors of neutrinos can interact with nuclei via the neutral current.

Charged Current A charged current (CC) event occurs when a neutrino interacts with a nucleon exchanging a $W^{\pm}$ to generate a lepton. This lepton is associated with the same flavor neutrino.

Figure 3.1: Neutral Current and Electron Charged Current scattering

3.2.2 Weak Nuclear Cross Sections

There are three types of neutrino cross sections in Super-Kamiokande:

(Quasi-)Elastic Scattering (Quasi-)elastic scattering occurs when a neutrino strikes the nuclei and the scattered particle (neutrino or lepton), has nearly the same energy as the incident neutrino. It can either be CC quasi-elastic scattering, where a neutrino scatters off a nucleon generating a lepton of the same flavor, or NC elastic scattering, where any flavor neutrino scatters off an electron. This is modeled in [69] with the standard quasi-elastic scattering off free protons. Nucleons are modeled by a Fermi gas model in [91], which assumes a flat Fermi momentum distribution of 225 MeV/c.

Single Pion Production A neutrino with intermediate energies (about 1 GeV) will sometimes excite resonant states of a nucleon, which eventually decays a single meson, often a pion. While pions are the dominant decay state, there are also decays of η, K, and Δ which are incorporated into the model. The resonance productions of π, K, and η are simulated described in [82, 81]. The intermediate baryon resonance W is restricted to be less than 2 GeV/c^2. If the neutrino happens to interact with the ^{16}O nucleus, which is much heavier than Hydrogen, it can also create a coherent pion. In this case the nucleus remains the same (no change to charge or isospin) but generates a charged pion. The nucleus does not move and thus the pion is mostly in the same direction as incoming neutrino. The model used in simulations is described in [83].

Multiple Pion Production Occasionally the neutrino scattering will create multiple pions, particularly at higher energies. For low masses (W $<$ 1.3 GeV), multiple pion cross sections are calculated with the Rein and Seghal model previously mentioned. For larger masses the cross sections are found assuming deep inelastic scattering (fragmented target and transformed into other particles) using the GRV94 [51] parton distribution functions. A custom program is used to generate pions for W masses between 1.3 and 2.0 GeV/c^2. For masses larger than 2.0 GeV/c^2, PYTHIA/JETSET [90] is used to find the final state hadrons.

See Figure 3.2 for the magnitude of various cross sections.
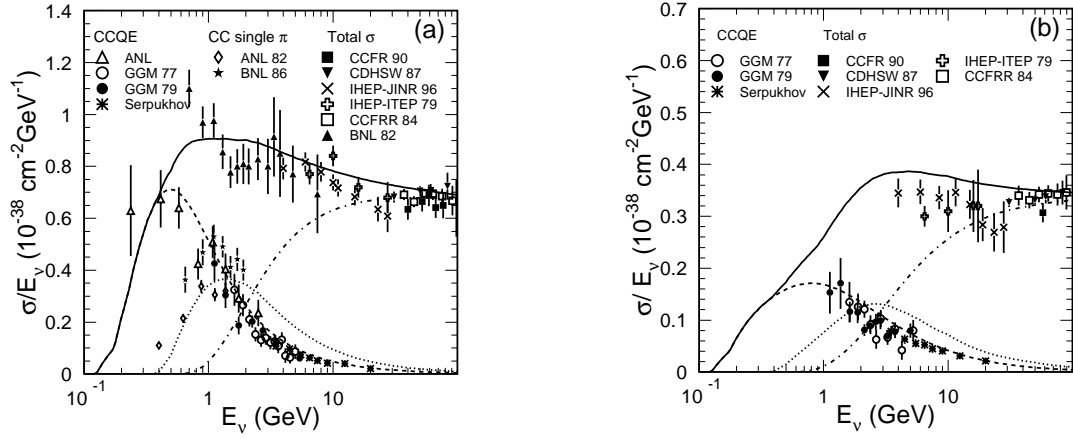
Figure 3.2: Charge current interaction cross sections for (a)neutrinos and (b)antineutrinos. The dashed lines are calculated quasi-elastic, dotted lines are single-meson, and dash-dotted are for deep-inlastic scatterings [21, 33, 36, 13, 26, 80, 66, 18, 28, 8, 94, 71, 20]. At low energies (below 1 GeV) the elastic and quasi-elastic cross sections are dominant. Above 10 GeV the multi-pion modes dominate. Single-pion mode contributions peak between 1 GeV $<$ E$_\nu$ $<$ 3 GeV.

3.2.3 Super-Kamiokande Interactions

There are eight major types of neutrino processes within Super-K.

$$\text{CC Quasi-elastic Scattering} \quad : \quad \nu_l + N \rightarrow l + N'$$

$$\text{NC elastic scattering} \quad : \quad \nu_l + N \rightarrow \nu_l + N$$

$$\text{CC single pion production} \quad : \quad \nu_l + N \rightarrow l + N' + \pi$$

$$\text{NC single pion production} \quad : \quad \nu_l + N \rightarrow \nu_l + N' + \pi$$

$$\text{CC coherent pion production} \quad : \quad \nu_l + {}^{16}O \rightarrow l^\pm + {}^{16}O + \pi^\pm$$

$$\text{NC coherent pion production} \quad : \quad \nu_l + {}^{16}O \rightarrow \nu_l + {}^{16}O + \pi^o$$

$$\text{CC multi-pion production} \quad : \quad \nu_l + N \rightarrow l + N' + m\pi (m \geq 1)$$

$$\text{NC multi-pion production} \quad : \quad \nu_l + N \rightarrow \nu_l + N' + m\pi (m \geq 1)$$

where N is a proton or a neutron (N' is a charged nucleon), l is a charged lepton, and m is an integer. In most cases, the neutrino interacts with the hydrogen nuclei unless otherwise mentioned.

Neutrino-generated pions and kaons in oxygen nuclei usually interact before escaping the nucleus. The neutrino-electron elastic scattering cross section is 10^3 times smaller than neutrino-nucleon interactions at 1 GeV, and is thus ignored the Super-K atmospheric neutrino analysis. More details of the interactions can be found in [64].

3.2.4 Neutrino-Induced Muons Entering Super-K

Neutrinos traveling through the Earth can also interact with the material surrounding the inner detector, either in the water in the outer detector or in the rock surrounding the entire detector. If so, the neutrino can generate a muon that passes through Super-K. (It may also generate an electron but they are more likely to interact again before entering the inner detector.)

3.3 Super-Kamiokande Detector Simulation

Two simulation programs (NEUT and NUANCE) are used to calculate Monte Carlo atmospheric neutrino interactions in Super-K's inner detector. A description of NEUT and NUANCE can be found in [55]and in [34], respectively. NEUT was the original package used in Kamiokande though modified for Super-K. It is used in simulating muons generated in the volume surrounding Super-K. The rock is assumed to be SiO_2, with charge $\langle Z \rangle = 11$ and mass $\langle A \rangle = 22$, with an average mass density of $\rho = 2.65\text{g/cm}^3$) [98]. Since there are only muon generated in rock only the charged-current cross sections are used and are calculated in a similar fashion as inner detector events but assume an invariant mass W > 1.4 GeV/c^2. For water interactions, the CALOR program is used for the hadronic interactions in the water above 500 MeV. At smaller energies a custom program was developed from π-^{16}O scattering and π-p scattering results.

The Cherenkov light generation and propagation is simulated by a custom program. The rest is simulated with Cern's GEANT package, which calculates the propagation of particles and PMT response. To simulate an event, the photons generated by the Cherenkov effect are distributed evenly along each track segment and azimuth until it is absorbed or detected, which depends on the wavelength. This includes both Rayleigh scattering off of water molecules and Mie scattering from particles in the water. In addition, the reflection and absorbtion of the black lining of the ID and white Tyvek of the OD are simulated, including the accumulated dust layer on the walls that

increases as a function of depth. PMT photon detection is simulated with the measured quantum efficiency and PMT reflectivity. For outside muons, the propagation in the rock is determined by a package from Lipari and Stanev [68]. Often these muons are of higher energies than those that are generated within the detector itself, whose energy range extends up to 100 TeV. This is modeled based on results from the Honda group [59] for energies up to 7 GeV, and by Volkova [93] for events at higher energies.

3.3.1 Electron and Muon-type Events

Super-Kamiokande only detects the muons and electrons induced by atmospheric neutrinos, and the leptons each have a distinct Cherenkov light pattern in Super-K.

Electron-type patterns Due to its light nature, a neutrino-produced high energy electron will "bounce around" in the water, losing some of its energy via Bremsstrahlung and emitting a photon. This photon can have enough energy generate a electron-positron pair that travel in a path similar to but not exactly the same as the original electron. If there is enough energy, the pair-produced electron and positron can emit Bremsstrahlung radiation of their own. The process repeats continuously, cascading to create an electromagnetic shower. Eventually the process comes to a rest as the resulting photons, electrons, and positrons scatter off their remaining energy. The detector result of the multiple electrons and positrons, each of which emit Cherenkov radiation is an event with a fuzzy, indistinct ring in the detector from multiple particles with overlapping light cones, as shown in figure 3.3.

Muon-type patterns In contrast, a muon is much heavier than an electron. The probability of a muon scattering and undergoing Bramsstrahlung is much smaller and to a lesser degree than electrons. Instead, the initial neutrino-produced muon is the dominant radiator of Cherenkov light, and the single source forms a nice, clear ring pattern on the detector, as shown in Figure 3.4.

A real world analogy of the difference of flavor type in the rings is explained in figure 3.5.

 It is also possible to have more than one distinct ring in an event. Multiple particle production within the detector can produce multi-ring events. Also muon bundles (parallel muons from the
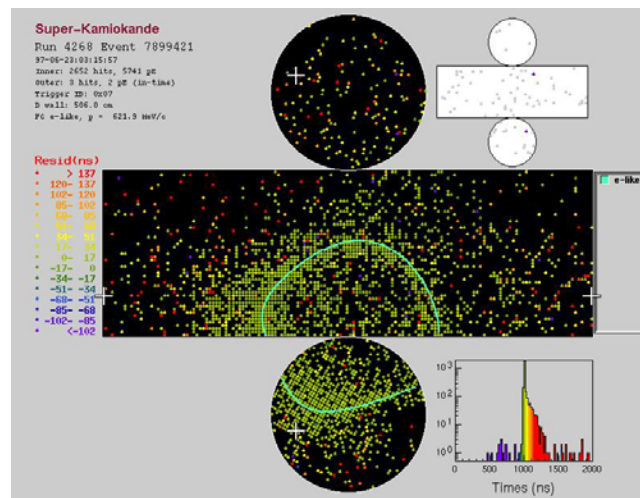
Figure 3.3: An electron-type event in Super-Kamiokande. The rectangle in the middle is the sides of Super-Kamiokande's inner detector projected, while the circles above and below is the top and bottom of the inner detector. The ring pattern here is fuzzy and indistinct.

same atmospheric cosmic ray shower,) can create two or more separate sets of rings. See Figure 3.6 for an example.
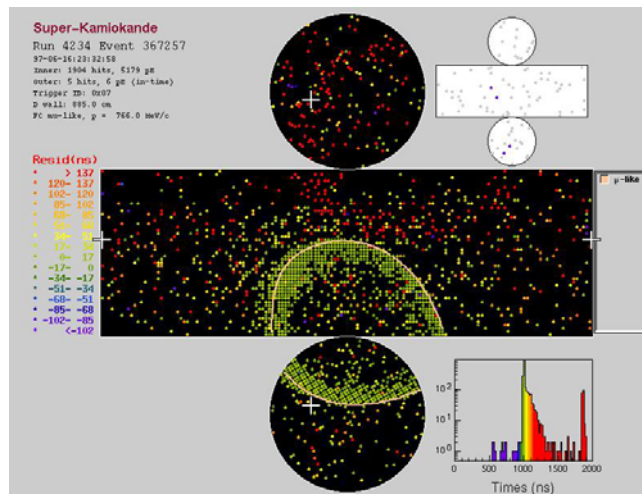
Figure 3.4: A muon-type event in Super-Kamiokande. The muon ring pattern is sharper compared to an electron event.
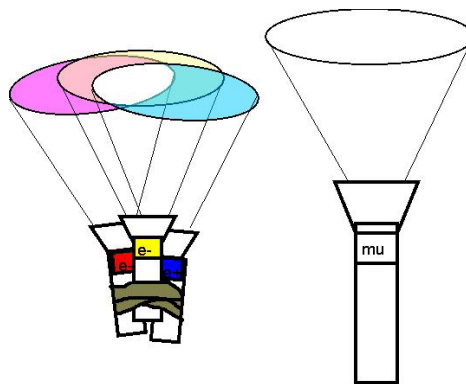
Figure 3.5: A flashlight analogy of an electron event versus a muon event. Electron type (A) has multiple light sources and has no clear ring shape. Muon type (B) has a single source and a definite ring.
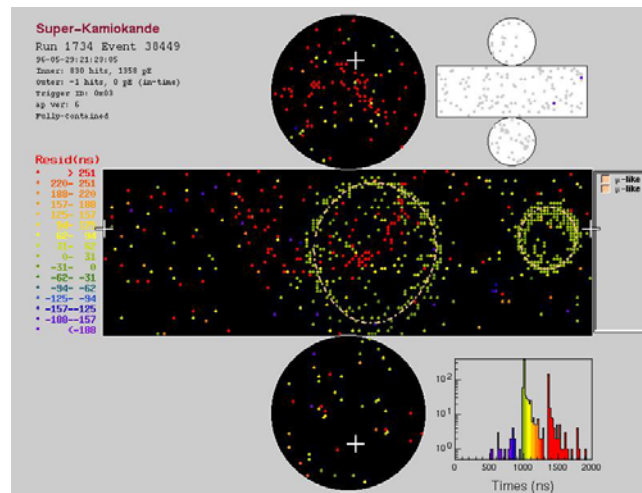
Figure 3.6: A multiple muon event in Super-Kamiokande.

Chapter 4

DETECTING SUPER-KAMIOKANDE ATMOSPHERIC NEUTRINOS

Super-Kamiokande does not observe neutrinos directly, but only the results of a neutrino interaction in the form of Cherenkov light from a particle. However, neutrino interactions are not the only causes of Cherenkov light in the detector. Nor are atmospheric neutrinos the only type of neutrinos detected in Super-K. Therefore, it is important to understand atmospheric neutrino characteristics.

4.1 Super Kamiokande Event Types

There are three major types of atmospheric neutrino events.

Fully Contained Event (FC) A fully contained event occurs when a neutrino enters Super-K and interacts with the water in the inner detector (more details on the interaction in Chapter 3). The interaction creates a charged particle that moves through the detector and generates Cherenkov light which gets captured by the PMTs. There is not enough energy to exit the ID and the particle eventually comes to a stop. The median energy for this type of event is about 1 GeV.

Partially Contained Event (PC) Similar to a FC event, a neutrino enters the inner detector and interacts, but in this case the energy is large enough to allow the particle exit the inner detector and into the outer detector. The majority of PC events are muons, as electrons in the water quickly shower their kinetic energy via further interactions or Bremmstrahlung processes mentioned earlier before exiting. These events have a median energy of about 10 GeV.

Upward Muons (Upmus) An upward muon is a muon that is generated by a muon neutrino in the rock surrounding Super-Kamiokande or in the water of the outer detector, and passes through the inner detector in an upward direction. These can either be upward through going muons (upthrumu) which have enough energy to enter and completely pass through the detector. The other case is an upward stopping muon (upstopmu), which enters the ID but comes to a stop

within the inner detector. While these muons may not be useful for calculating the double ratio R they can probe neutrinos that are higher energies than contained events. The parent energy range for an upward muon is much higher than an FC or PC events, at around 10 and 100 GeV for a upward stopper and through-goer, respectively. Note that an upward going neutrino that reacts within the detector and produces a muon is not an considered and upmu, but instead regarded as a contained-type event. About 80% of Super-K's upward going muons come from interactions with the rock near the detector, and the remaining 20% are from water interactions in the outer detector.
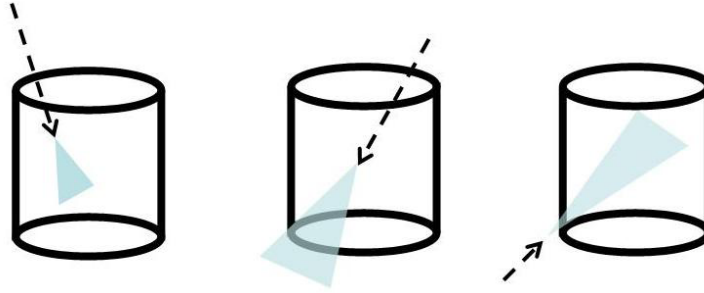
Figure 4.1: Examples of Fully-Contained, Partially-Contained, and Upward-Stopping Muon Events

4.1.1   False Events

Note that there are no upward-going electrons or downward-going electrons or muons (downmus) considered in the analysis. Upward-going electrons are not considered because an electron's cross section is so large that it is quickly absorbed within a meter of rock. It is negligibly small that the rock-generated electron would manage to pass into the detector. As for downmus, Super-K cannot count them reliably in its analysis. While there are downward going muons generated from neutrinos in the rock above Super-Kamiokande, they are indistinguishable from the cosmic ray muons that have enough energy to penetrate the mountain into the detector. These high energy downward going muons are a source of noise that create an abundance of events that have to be filtered out of the data stream for neutrino analysis. Upward going muons are accepted because no cosmic ray has

enough energy to pass through the Earth in an upward direction into the detector. Any muon coming upwards through the detector would have have been generated by a neutrino in the surrounding rock. A related source of upward going muon noise comes from near horizontal cosmic rays that creating muons in the surrounding rock with a slight upward direction. This can happen from multiple Coulomb scatterings, and is especially prevalent in the thinner wall areas of the mountain. These are not neutrino-induced muon events and are removed from the upward going muon data distributions.

Other large sources of background are "flashers"; an electric discharge in a PMT that randomly emits light, creating a false trigger. These events are filtered out of the data stream by studying consecutive events, which have similar light patterns. Another source of noise are downward going muons that enter through the cable bundles that line the quadrants of the outer detector and hold the signal and high voltage wires. These may falsely appear as a contained event because the muon passing through the cables may not deposit any light on the outer detector. This has been partially remedied by installing veto counters which are plastic scintillators installed over the cable holes. Radioactivity in the rock (such as radon) surrounding the detector also cause low energy triggers.

4.2   Data Reduction

To ensure that the information received from Super-Kamiokande is useful for the atmospheric neutrino analysis, there are a number of filtering processes done on the raw data for each of the three major types of events. These are mostly automated processes designed to be conservative and err in favor of not rejecting neutrino events. The PC and upmu event processes are followed by a human scan of remaining events to act as a final filter.

4.2.1   Fully Contained Data Reduction

A fully contained event is characterized by the Cherenkov light path starting and stopping completely within the detector. The outer detector is used as a veto counter to determine which events came from neutrino interactions in the tank, confirming that there is no significant light detected by the OD. An event must have less than 10 PMT hits in the OD to qualify as FC. As a conservative measure, the FC analysis only uses events whose initial calculated light path vertex is at least 2

meters (which represents 5.5 radiation lengths, or 3.3 nuclear interaction lengths) from the inner detector wall, making the fiducial detector volume 22,500 tons of water. This is to reduce possible contaminations of entering events and ignore poorly fitted events near PMTs, making sure that an event can be accurately reconstructed. It must also have at least 30 MeV of visible energy (the sum of all energy rings for a given event,) in order to eliminate low energy backgrounds. For muon events, the momentum is required to be $> 200 MeV/c$ for single-ring events or $> 100 MeV/c$ for single-ring electron events. In the case of a multi-ring, Super-K requires the most energetic ring is mu-like and momentum $> 600 MeV/c$ and $E_{vis} > 600 MeV$.

Below outlines the general procedure in filtering out a fully contained event candidate. The efficiency of the entire process to accept a real event is checked with Monte Carlo and estimated to be 99.4% with an uncertainty of less than 1%.

FC First Reduction

These are very basic and simple cuts to reduce large amounts of nonessential data.

- The time between the previous event and the current one must be larger than 100 μs, to eliminate decaying stopping cosmic rays which produce multiple triggers.

- The energy must be larger than 200 photoelectrons (p.e.) in the inner detector in a 300 ns time window, corresponding to roughly 23 MeV of energy. This cuts the majority of low energy events from radioactivity. Events with energies less than 30 MeV are not used in the analysis, so this is a conservative cut.

- The total number of OD PMT hits must be less than 50 in a 800 ns time window around the central trigger. This cut removes most of the cosmic ray muon events since they have activity in the OD.

Cuts are livetime and reduce the load from 10^6 triggers per day to about 3000 events per day.

FC Second Reduction

These are more specific cuts to further reduce low energy and cosmic ray events.

- There must be no OD triggers or the number of OD PMT hits must be less than 25 in a 800 ns window for a ID trigger with less than 100,000 photoelectrons. This is a tighter cut on events with activity in the outer detector.

- The ratio of single PMT p.e. to the total number of p.e must be less than 0.5 to prevent flasher-type events in a 300 ns time window. This is to remove low energy and electronic events with one large hit area.

The 2nd reduction reduces the load from 3000 events per day to 200 events per day.

FC Third Reduction

The third reduction eliminates cosmic ray muons with little activity in the OD. It also focuses on flasher events, low energy radiation events and accidental coincidences of low energy events and cosmic ray muons.

- No single ID PMT can record more than 230 photoelectrons, and a goodness-of-fit done by fitter programs cannot classify it as a through-going muon with a goodness-of-fit exceeding 0.75. In addition, there cannot be more than 10 OD PMT hits within an 8m radius of entry or exit points in a 800 ns time window. This is to cut through going muons with little activity.

- There cannot be more than 10 OD PMT hits or 5 OD PMT hits with a g.o.f. of a stopping muon fit exceeding 0.5 within an 8m radius of entry points in a 800 ns time window. This is to cut stopping muons with little activity.

- There cannot be a veto counter hit with the distance from the reconstructed vertex to a cable hole be less than 4 meters. This is to prevent cable hole muon events.

- Within a 400 and 900 nsec window after the initial trigger, the number of hit OD PMTs cannot exceed 20, and within this same window, the number of ID PMTs cannot exceed 5000 p.e., to prevent accidental coincidence events.

- The minimum number of hit ID PMTs in a sliding 100 nsec window between 300 and 800 nsec after the initial trigger cannot exceed 13, or or exceed 9 if the total number of hit ID PMTs is below 800, to help cut flasher events.

- The number of hit ID PMTs in a sliding 50 nsec window counted cannot exceed 50 after subtracting the time of flight of the initial photon assuming all are generated from a single vertex, to cut low energy events.

The 3rd reduction drops the event rate to about 45 per day.

FC Fourth Reduction

To remove flasher events a "Flashscan" algorithm was applied. It removes the "double events" that often occur when a PMT begins to malfunction as a flasher and leaves similar light patterns consecutively. Such consecutive similar looking events is unlikely to be caused by neutrinos. After "Flashscan" is applied the event rate drops from 45 to about 18 per day.

FC Fifth Reduction

After this a series of specific cuts specialized for background noise are implemented.

- The number of OD hit PMTs must be less than 5 within a sliding 200 nsec window from 400 nsec before and after the trigger within 8 meters of the vertex, to cut any remaining stopping muons.

- If the total number of p.e. in the ID is below 1000 and the maximum number of hit PMTs in the OD cluster is greater than 4 in a sliding 200 nsec window from 8800 nsec before to 100 nsec after, and the if it is greater than 9 if the distance of 2 OD PMT clusters is greater than 500 cm, or if it is less that 500 cm and the sum of the maximum number of hit PMTs in the OD cluster and the number of hit PMTs in the OD hit clusters in a fixed 500 nsec window from 100 nsec before to 400 nsec exceeds 9, is cut from the data stream. This is the "invisible muon" cut, which are caused by cosmic ray muons that do not emit Cherenkov light due to its lower energy, but its decay electron emits radiation.

- Events whose total number of p.e. is less than 300 in a 500 nsec window from 100 nsec before to 400 nsec after the trigger, and the maximum number hit OD PMTs in a 200 nsec sliding window between 400 to 1600 nsec after the trigger exceeds 20 are rejected. This cuts any remaining coincidence events.

- If the goodness of point fit is less than 0.4 and the minimum number of ID hit PMTs in a sliding 100 nsec window between 300 and 800 nsec after the trigger exceeds 5, then the event is billed as a long tail flasher cut and is removed.

This leaves about 16 events per day, with 8.3 events per day in the fiducial volume.

4.2.2   PC Event Reduction

Like FC events, PC events are characterized by Cherenkov light starting spontenously within the inner detector but instead proceeds through the outer detector and exits the entire volume. While many of the cuts used to reduce PC events are similar as FC, because of the activity in the OD for a PC event, the minimum requirements are different and the reduction process is a slightly altered. Like an FC event, PC events have a fiducial volume cut limiting the distance between the initial vertex and the wall to at least 2 meters. But the event must have at least 10 PMT hits in the OD to qualify as exiting. The total photoelectron count in the ID has to be greater than 3000 p.e. (or a visible energy of about 350 MeV). This energy cut corresponds to a momenta of 530 MeV/c, which is a conservative measure as a PC muon needs 700 MeV/c to even reach to OD.

Efficiency of the PC reduction is a trickier business. Because it requires activity in the outer detector, it is more likely for a background cosmic ray muon to enter the data stream. Monte Carlo events are used to estimate the efficiency of the PC reduction. The efficiencies are found to be 99.0, 94.2, 93.2, 87.9, and 84.6 % for the 1st, 2nd, 3rd, 4th, 5th reduction, respectively. The uncertainty is estimated at 3.2%.

PC First Reduction

These are quick and dirty cuts to get rid of obvious non-PC candidates quickly.

- The time between the previous event and the current one must be larger than 100 μs.

- The energy must be larger than 1000 p.e. in a 800 ns time window in the ID, corresponding to 120 MeV, to ensure the particle has enough energy.

- The width of the OD PMT times must be less than 260 ns.

- The number of OD PMT hit clusters found must be less than 2. These two criteria eliminates most through-going muons, which have 2 clusters at the times the muon enters and exits the OD.

This leaves about 14000 PC candidate events per day.

PC Second Reduction

This reduction focuses on the activity in the outer detector, looking at clusters of hits by dividing the wall into regions and seeing the PMT charge gradient in the neighboring patches.

- There must be less than 2 clusters of at least 6 hit PMTs found in the OD.

- The minimum number of hit PMTs in the OD cluster must be less than 7. This is to eliminate corner clipping muons.

- If there is an OD cluster it must have a corresponding ID cluster with more than 1000 p.e. in an area less than 200cm from the highest charge ID PMT. This helps to filter out stopping muons.

After the second reduction there are about 2000 events per day.

PC Third Reduction

Like with the FC third reduction, cuts are made to eliminate flasher events and cosmic ray stopping muons. The same flasher cuts are applied here. In addition, a fit algorithm called point-fit is applied that uses the light in the detector to predict a cosmic ray muon pattern if it had gone through the detector, even if there were no OD hits. Point-fit is explained in Section 5.1.1.

- Events where the minimum number of hit ID PMTs in a floating 100 nsec window from 300 to 800 nsec after the trigger exceed 14 or if they exceed 9 if the total number of hit ID PMT is less than 800 are rejected as flashers.

- If the number of OD hit PMTs within 8m from the entrance vertex in a 500 nsec window is greater than 10, it is rejected as a stopping muon.

This leaves about 100 events per day.

PC Fourth Reduction

This is a refined version of the third reduction, to reduce cosmic ray events with little activity in the OD by comparing the pattern with the earliest hit PMTs. In addition, a long track muon fitter is used in this step to cut events with tracklengths longer than 30m.

- The product of the reconstructed direction by a point fit with the direction from the reconstructed vertex to earliest hit PMT should be greater than -0.8. This is to eliminate cosmic rays which can have these direction antiparallel.

- The distance from the reconstructed vertex by the point fit to the nearest ID fringe must be greater than 150 cm. This is to remove corner clipping events; a "corner clipper" is an event the just skims through a corner of the detector but deposits enough light in the ID. These events create light patterns that are often difficult to fit.

- The estimated track length of a muon from entrance to exit point should be greater than 30 m if the g.o.f. of a through-muon fit is greater than 0.85. This is to eliminate through going muons with long tracks.

This leaves about 20 events per day.

PC Fifth Reduction

At this point, various cuts are tried to eliminate any remaining noise events. Two other fitters (MS-fit and TDC-fit) are used here, and are explained in more detail in Sections 5.1.2 and 5.1.6.

- The total number of p.e. in the inner detector must be greater than 3000. This eliminates any low energy background.

- The distance from the highest OD cluster and the next greater than 20 m, whose p.e. is greater than 10 is classified as a through-going muon and is removed.

- A new set of clusters is generated with smaller boundaries, allowing for fainter clusters. If the number of OD hit clusters that contain more than 9 PMT is greater than 2 in this new setting, it is classified as a through-going muon and is removed.

- If the maximum number of OD hits in an 8 m radius sphere centered at the top edge is greater than 7 and likewise for the bottom edge, and the number of p.e. detected in these spheres is greater than 10, and the time interval between the average hit timing of the two spheres is between 100 and 200 nsec, than it is classified as a through-going muon and is rejected. This is a case where a muon travels vertically along the wall of the detector, which may not yet be rejected due to its poor reconstruction.

- A tighter and more computationally intensive track fitter program called MS-fit is applied. If the number of hit PMTs in the OD within 8 meters of either the entrance and exit point is greater than 5, and the average hit timing between the PMTs closest to the entrance and exit points is between 100 and 200 nsec from the results of this new fitter, it is classified as a through-going muon and is rejected.

- If the number of OD hit PMTs within 8 meters of the reconstructed entrance point using MS-fit meets or exceeds 10, it is classified as a stopping muon and is rejected.

- If the opening angle between the direction of the OD cluster and the ring direction is greater than $90°$ as a result of MS-fit or TDC-fit, it is classified as a stopping muon and is rejected. A PC event expects this angle to be small.

- If the g.o.f. of a stopping muon fit is greater than 0 and the ratio of the number of PMTs in the ID within a $42°$ cone to the total number of p.e. in the ID is greater than 0.6, and the

number of hit OD PMTs within 8 m of the entrance position is greater than 6, then the event is rejected as a stopping muon.

- If there is a veto counter hit and the product of the reconstructed ring direction and direction from the hit veto counter to the vertex as found by TDC-fit is greater than -0.8, then the event is classified as a cable muon and is rejected.

This leaves about 2 events per day.

PC Eye Scanning Reduction

At this point, any remaining events are visually confirmed by two members of the PC group. These eye-scans are done independent of the other member's knowledge, and each passing event must be doubly confirmed as PC or doubly rejected. An event where there is disagreement is reviewed further by a third member of the group.

This leaves about 1 event per day, and about 0.6 after fiducial volume cuts.

4.2.3   Upward Going Muon Reduction

While the contained events are generated by neutrinos entering the detector, the upward going muons are generated by neutrinos below the detector creating muons that enter Super-K fiducial volume. The reduction scheme must be different from the contained events since here there must be at least a definite entry cluster of at least 10 OD PMT hits within 8 meters of the exit point. An upmu candidate must also have at least 8000 p.e. in the ID which corresponds to a momentum of 1 GeV/c, a safe cut and minimum for good resolution, since Super-K only considers upmus of energy greater than 1.6 GeV. Since upmus are typically high energy events, all events with a specialized low energy (lowe) or super low energy (sle) trigger are immediately vetoed and removed from the upmu data stream. An upper limit energy cut of 1750000 p.e. (about 215 GeV) is applied, and any more will saturate the inner detector with so much light no useful upmu information can be gained. Upmus must also have a fitted track length of 7 m for the muon in the detector for accurate resolution. This is to help reduce the background of upward going pions produced from downward pions, which do not penetrate the water for such distances. Corner clippers events need to be removed because it

usually fails the tracklength requirement and is usually downward. Unfortunately these events are not usually fit well and are difficult to filter out. All pedestal and multiple muon events are also removed.

To classify an upward going muon, the data must be quickly filtered to save upward and horizontal muons and reject the downward going muons. The expected few upmu events per day are eclipsed by the 200,000 downward going muon background. Yet the event displays look nearly identical except for the direction of travel of the muon. After the energy cuts, the events can only be cut by the zenith (upward) direction. The detection efficiencies are estimated to be 96.2% for upward stopping muons and 97.2% for upward through going muons, with the exception of the near-horizontal muons. The systematic errors are found to be 1.25% for upstop and 0.54% for upthru muons.

Estimates of downward going muon contamination in the horizontal is found by extrapolating the zenith angle distribution of the downward going muons.

Upmu 7 Fitters

The data is initially run through a program of seven different muon fitters designed to separate out the useful upward and horizontal events. Each of these fitters are specialized for a particular type of muon event in the detector, either classifying the type (stop, thru, corner, multiple, unknown), or the entry point and direction. Detailed information about each fitter is found in [41]

1. stopmu1st: A straightforward fitter that classifes the type of muon using the OD information.

2. muboy: A quick all purpose fitter than classifies type as well as a fit vertex and direction.

3. stopmu2nd: A specialized stopping muon fitter.

4. thrumu1st: A quick through-going muon fitter.

5. fstmu: Another fast through-going muon fitter.

6. thrumu2nd: A fitter specialized for multiple and Bremsstrahlung muons.

7. nnfit: A fitter specialized for Bremsstrahlung that have high charge.

The general data flowchart of these 7 fitters is as follows:

- If classified as upward stopping or through-going within a regulated goodness-of-fit value by muboy or stopmu1st, then the event is saved.

- If both muboy and stopmu1st classify the event as a multiple muon, then the event is rejected.

- If classified as downward within a regulated goodness of fit value, then the event is immediately rejected.

- If classified as horizontal, it is flagged as such and passed on to the next fitter.

- If a particular fitter cannot classify it within a regulated goodness of fit value, it is passed on to the next fitter.

- If an event has been run through all fitters and has at least one horizontal flag, then the event is saved.

- Else if an event has run through all fitters and was not able to be classified within a reasonable goodness-of-fit, the event is rejected.

Precise Fitter

If an event is not rejected as a downmu candidate after the seven fitter test, it is run through a precise fitter to see if can be considered an upmu. The resolution of this fitter when compared to Monte Carlo events for upward through-going muons is about $1.05\,^\circ$, and for upward stopping muons is about 1.5°. The precise fitter is designed to fit a muon's vertex and direction to a high degree of accuracy, but at the cost of computation time. It is actually a combination of three fitters called upmu-fit (modified from MS-fit), OD-fit (a fitter which primarily uses OD information), and TDC fit, and was primarily developed by K. Nitta. More details of this can be found in his thesis [76].

Expert Eyescanning

As a final check, the events that have been cleared as an upmu by the precise fitter are checked by members of the Super-Kamiokande upward going muon group. It is a double-expert eye scan and judged whether or not to be a true upward going event and a good fit by the precise fitter. Like the PC events, these members are trained to recognize what characterizes an upmu event and use a viewer to check the data event by event to insure that it is so. Most bad fit events are downward corner clipping muons which are not fit well but falsely passed by many fitters, including the precise fitter. These are easily identified by eye and are rejected as upmu data. Some events are slightly misfit as near horizontal but are truly downward. If both experts agree that the event passes, it is accepted as upmu data. In the case of a discrepancy, the event is viewed by a third member of the group, usually a more senior member who makes the final decision.

If the event eventually passes the double eyescan as a upward going muon or horizontal muon, the vertex and direction results from the precise fitter will be used as official direction and energy results.

Once a event is considered an upmu, it is determined as a stopping or through-going muon based on the following criteria:

- It is considered a stopping muon if the number of OD hits within a 500 nsec window from 800 to 1300 nsec and 8 meters from the entry point meets or exceeds 10 and the number of OD hits within a 500 nsec window from 800 and 1300 nsec and 8 meters from the exit point is less than 10.

- It is considered a through-going muon if number of OD hits within a 500 nsec window from 800 to 1300 nsec and 8 meters from the entry point meets or exceeds 10 and the number of OD hits within a 500 nsec window from 800 to 1300 nsec and 8 meters from the exit point meets or exceeds 10.

There are about 0.3 upward stopping events and 1.2 upmu through-going events per day after the reduction.

Chapter 5

RECONSTRUCTION OF CONTAINED EVENTS

After the PMTs and electronics map out the Cherenkov light pattern, Super-K needs to infer the original neutrino direction and flavor. To do so, it runs through several steps. First it needs to identify the most energetic ring in the detector and determine the type, vertex, and direction of travel of the particle based on the shape and timing of the ring. The neutrino's vertex and direction is assumed to be the same as the leading particle.

The following reconstruction is done only for the fully and partially contained events. The fitting reconstruction for the upward going muons are treated as have coming from muon neutrinos and has been described previously in Section 4.2.3.

5.1 Vertex Fitting

5.1.1 Point-Fit

The location of the neutrino interaction must be determined. It is found using the timing information from the PMT hits. An idea of the vertex is found by assuming all light comes from a single source. The vertex is determined by a point-fit algorithm which maximizes the timing residual distribution after accounting for time of flight from the vertex to the PMT. A quick estimation of the direction is determined by using the vertex and summing the direction vectors from PMT to vertex, weighted by the charge of the PMT.

With an idea of the vertex and direction another algorithm is used to determine the outer edge of the most energetic ring.

5.1.2 TDC-fit

A timing fit is used to determine the contained event vertex. The vertex position determination program (TDC-fit) finds the direction of the particle based on the outer edge of the Cherenkov ring on the PMTs. Then it calculates the time of flight of the photon in water. It takes an average of the

time interval to account for the finite resolution of the PMT and having a moving photon emitter. Vertex resolution is estimated at 64.2, 58.7, and 134.4 cm for FC e-like, FC μ-like, and PC events respectively. Once the vertex is calculated then the track direction and opening angle of the cone is determined by looking at the hit PMTs as a function of a varied angle between track and vector of the vertex. The process is iterated until a best fit is found.

5.1.3   *Ring Counting*

After the most energetic Cherenkov ring is determined, Super-K uses a program to count the total number of rings in the event(Fig. 5.1). Multiple rings can be created from a single neutrino source generating several particles. The algorithm assumes the particles travel in a common direction. A Hough transfomation is used to determine ring candidates and estimate the particle's direction. The candidates are then checked as true rings via a likelihood method.
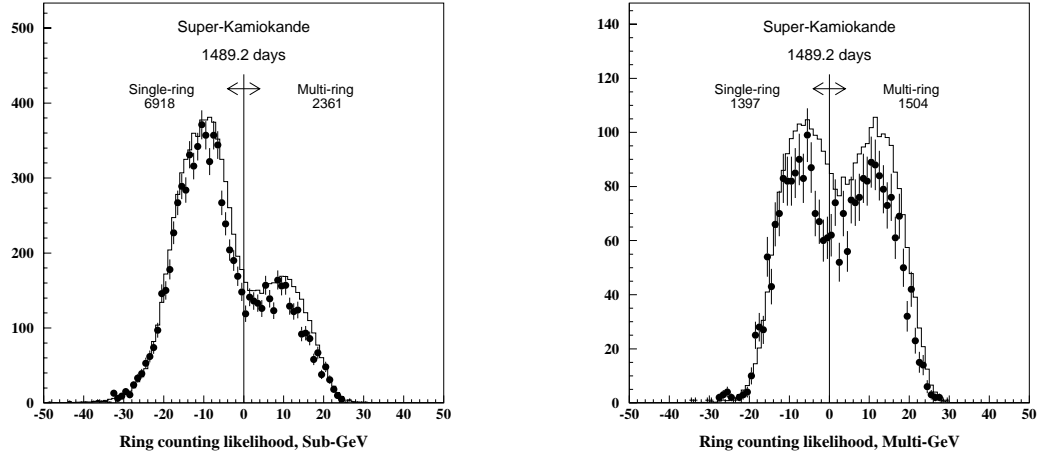
Figure 5.1: Ring counting likelihood comparison for Sub-GeV events and Multi-GeV events.

5.1.4   *Particle Identification*

For events with only a single ring, a particle identification program is used for events. As mentioned in Section 3.3.1, electron and muons create different cone patterns. The identification algorithm considers the ring pattern and the opening angle. Discernment between muon and electron rings

are determined by a likelihood statistic checking which lepton better reproduces the light shape. The likelihood is well separated and the shape of the data distribution is well reproduced by Monte Carlo (Fig. 5.2). This process is further checked with muon decay electrons and stopping cosmic ray muons, as well as the KEK experiment using the same algorithm with its smaller scale water Cherenkov detector.
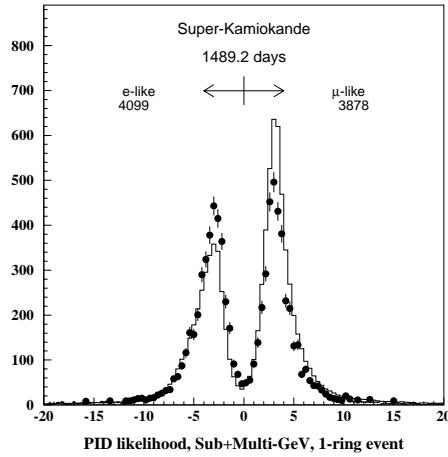
Figure 5.2: Particle identification likelihood distribution. A positive likelihood L is considered a muon events and a negative L is electron.

5.1.5 Momentum Determination

Particle momentum determination looks at the light deposited in the detector, and depends on vertex position, particle direction, and water transparency. A sum of corrected photoelectron counts, called RTOT, is derived. It adds the photoelectrons from the Cherenkov cone with a $70\,^{\circ}$ opening angle within a time window between -50 and 250 ns, after being corrected for water transparency, scattered light, and relative gains for each PMT. This corrected count is related to momentum and calculated based on MC event samples.

5.1.6   Precise Fitting

A special program called MS-fit (Meson and Shower fit) is used to more precisely determine the vertex point. TDC-fit is based purely only PMT information which is heavily biased between electron and muon events. Unlike TDC-fit, MS-fit finds a vertex where the likelihood becomes maximal by keeping the opening angle fixed based on particle ID and momenta, instead of being treated as a free parameter. The performance of the fitters are found by comparisons with Monte Carlo events. Vertex resolution is improved 20-50 cm with MS-fit, and angular resolution of the particle direction is estimated at $3.0°$ and $1.8°$ for single ring e-like and μ-like fully-contained events, respectively. The angular resolution for a PC event is estimated at $2.8°$ of the true particle direction. The resolution is defined as the width at which 68% of the events are included.

After MS-fit another ring counting check is applied. Rings can be mis-fit due to low momenta and overlapped cone patterns, and several cuts are made to reject such rings.

5.2   True Neutrino Direction

The direction of the scattered lepton is not the exact direction of the incoming neutrino. The correspondance is dependent on the energy of the particle. For the contained events, the average difference in angle between a lepton and its parent neutrino is $55°$ for $p = 400$ MeV/c. At 1.5 GeV/c this differences shrinks to $20°$. The average angle between reconstructed direction for an upward muon and its parent neutrino is about $8.7°$ for and up-stop and $3.3°$ for an up-thru. The resolutions are determined from Monte Carlo based on the models developed in Chapter 3.

Chapter 6

DATA SUMMARY

The SK-I running period runs from the beginning of the experiment on May 17, 1996 until a shutdown for refurbishing in July 16, 2001. The livetime for the FC and PC events for this time is 1489.2 days (92 kilton-year), and 1645.9 days of upward going muon events. (Upward going events are long track fitting events and thus less sensitive to detector effects.) The statistics for Monte Carlo events are over a 100 year period, and the MC data is run through the same FC,PC, and upmu reduction schemes. According to [88,53] the cosmic ray flux which affects the low energy neutrinos, was near a solar minimum until summer of 1999, at which time it rapidly changed over the course of a year, and then held consistent with a solar maximum until the end of the SK-I running period. This is reflected in the Monte Carlo.

For more information as to data taken after July 2001, see Appendix A.

6.1 Contained Event Summary

Summaries of the FC and PC reductions and event distributions are be found in Tables 6.1,6.2, and 6.3.

Table 6.1: Event Summary for FC events. Monte Carlo is based on flux in [61]

Reduction	Data	Monte Carlo
Triggers	1889599293	14013.9
First Reduction	4591659	14006.3
Second Reduction	301791	14006.1
Third Reduction	66810	13993.3
Fourth Reduction	26937	13898.1
Fifth Reduction	23984	13895.3
Fiducial Volume / $E_{visible}$ Cuts	12180	13676.7

Table 6.2: Event Summary for PC events. PC events all assumed to be μ-like. Fraction of CC $\nu_\mu, \overline{\nu_\mu}$ in PC sample estimated to be (97-98%). Monte Carlo is based on flux in [61]

Reduction	Data	Monte Carlo
Triggers	1889599293	1417.0
First Reduction	34536269	1402.8
Second Reduction	5257443	1334.7
Third Reduction	380053	1318.7
Fourth Reduction	53825	1246.2
Fifth Reduction	1483	1201.0
Fiducial Volume	911	1129.6

Table 6.3: Event Summary for Sub-GeV,Multi-GeV, and PC events after cosmic ray background subtraction.

	Sub-GeV Events		Multi-GeV Events		PC Events	
	DATA	MC	DATA	MC	DATA	MC
1-Ring	6580	7092.6	1397	1580.4		
e-like	3353	2879.8	746	680.5		
μ-like	3227	4212.8	651	899.9		
2-Rings	1614	1833.3	565	730.0		
$\geq$3-Rings	747	958.4	939	1161.6		
Totals	8941	9884.3	2901	3472.0	911	1129.6

6.2 Double Ratio Results

Fully contained event data is subdivided into two energy groups. The sub-GeV and multi-GeV groups are split by visible energies above and below 1.33 GeV. (This is the same way that the Kamiokande data was separated.) They are further divided by particle (electron or muon) type. Low energy minimum cuts of electron momentum greater than 100 MeV/c, or the muon momentum greater than 200 MeV/c are applied to single ring events.

Solving for the double ratio R from Tables 6.1 and 6.2 yields:

$$\text{Sub-GeV: } \frac{(\mu/e)_{DATA}}{(\mu/e)_{MC}} = 0.658 \pm^{0.016}_{0.016} \pm 0.032$$

$$\text{Multi-GeV: } \frac{(\mu/e)_{DATA}}{(\mu/e)_{MC}} = 0.660 \pm^{0.036}_{0.035} \pm 0.093$$

$$\text{Multi-GeV + PC: } \frac{(\mu/e)_{DATA}}{(\mu/e)_{MC}} = 0.702 \pm^{0.032}_{0.030} \pm 0.099$$

$$\text{stat.} \quad \text{syst.}$$

The flavor ratios is predicted with 3% error, and a table of the systematic uncertainties can be found in Table 6.4. If the MC prediction matched the observation, the R value would be close to unity. However, the value is less than unity, which is consistent with previous neutrino experiment measurements, but with smaller errors. A clue to the disappearance can be found by sorting the neutrinos by the vertical direction: traveling upwards or downwards.

6.2.1 Neutrino up/down ratio

A summary of the up and down neutrinos and the ratios is in Table 6.5. The electron and muon up-down distributions are expected to be symmetric. The results show the electron neutrino data matches up well with prediction, so it does not appear that the neutrino flux model is incorrect. However, it is the muon neutrino data is much smaller than predicted, which was alluded to in earlier experiments. It now appears that the muon neutrino direction plays a crucial role in its disappearance. The asymmetry seems to be depend on the neutrino energy as well.

Table 6.4: Systematic Errors in calculating R. A detailed description of the errors can be found in Section 8.2.

	Sub-GeV(%)	Multi-GeV(%)
ν_μ/ν_e Ratio	2.7	2.2
$\nu/\overline{\nu}$ Ratio	1.6	0.8
K/π Ratio	0.6	1.9
E_ν Spectral Index	0.6	2.3
Sample-by-sample	-	2.9
ν Interaction		
quasi-electron scattering	1.4	1.0
single-meson production	<0.1	0.3
deep-inelastic scattering	0.2	0.5
coherent-pion production	0.4	0.2
NC/CC ratio	0.5	2.0
Nuclear Effects	1.3	0.8
Hadron Simulation	0.7	<0.1
FC Reduction	0.1	0.1
Non-ν Background	<0.5	<0.3
μ/e Separation	1.3	0.6
Single-ring/Multi-ring Separation	3.2	13.2
Energy Calibration	0.6	1.2
MC Statistics	0.5	0.9
Total	5.3	14.4

Table 6.5: Up/Down Neutrino Ratio.

			Nup	Ndown	Nup/Ndown
DATA					
Sub-GeV	e-like		1405	1267	$1.109\pm^{0.044}_{0.042} \pm 0.005$
Multi-GeV	e-like		270	281	$0.961\pm^{0.086}_{0.079} \pm 0.009$
Sub-GeV	μ-like		1143	1476	$0.774\pm^{0.031}_{0.030} \pm 0.002$
Multi-GeV	μ-like	FC+PC	413	749	$0.551\pm^{0.035}_{0.033} \pm 0.002$
		FC	171	353	$0.484\pm^{0.047}_{0.043} \pm 0.002$
		PC	242	396	$0.611\pm^{0.052}_{0.048} \pm 0.003$
MC					
Sub-GeV	e-like		1166.6	1128.9	$1.033\pm0.009 \pm 0.12$
Multi-GeV	e-like		252.2	252.9	$0.997\pm0.018 \pm 0.015$
Sub-GeV	μ-like		1708.9	1649.7	$1.036\pm0.007 \pm 0.015$
Multi-GeV	mu-like	FC+PC	762.3	763.2	$0.999\pm0.010 \pm 0.008$
		FC	354.9	353.9	$1.003\pm0.015 \pm 0.008$
		PC	407.4	409.3	$0.995\pm0.014 \pm 0.008$

6.3   Upward going muon event summary

The upward going muon data may not have contributed to the double ratio R but it may help provide insight about the missing muon neutrinos, especially since the energy range of upmus is 1-2 orders of magnitude larger than contained events. Super-K's upward stopping and through-going muon data is summarized in Table 6.6. It is clear that there is a muon deficiency in the upmu sample as well.

Table 6.6: Event Summary for Upmu events. Monte Carlo is based on flux in [61]

	Data		Monte Carlo	
Reduction	Stop	Through	Stop	Through
Triggers	2129729843		697.1	1741.0
Reduction	89911		693.9	1722.3
Precise Fitter($\cos\theta \leq 0$)	4266		692.4	1721.7
Eye Scan	2447		-	-
Stop-through separation and $E_\mu \geq$1.6GeV	458	1856	713.5	1669.5
CR BG subtraction(subtracted events)	417.7	1841.6	-	-

6.4   Zenith Angle Distribution

Super-Kamiokande's directional information can be used to determine the mechanism or origin of the lack of muon neutrinos. There is a large variation in the typical distance an atmospheric neutrino has to travel in order to reach Super-K. Neutrinos coming up from the ground travel a much longer path length that traverses the diameter of the Earth($\tilde{1}3000$ km) compared to a neutrino coming from directly overhead which travels less than 20 km.

The distribution (Figure 6.1) of expected neutrino counts is sorted as a function of the zenith angle (the angle between the neutrino direction and the vertical axis through Super-K). The FC and PC zenith angle bins are 10 $\cos\theta_{zenith}$ bins equally separated between $\cos\theta_{zenith} = 1.0$ (neutrinos coming downward from directly above the detector) and $\cos\theta_{zenith} = -1.0$ (neutrinos coming upward from directly below the detector). The upward muons zenith angle bins are 10 $\cos\theta_{zenith}$ bins

equally separated between $\cos\theta_{zenith} = 0.0$ (horizontal neutrino coming from the horizon) and -1.0 (upward going). FC events are also subdivided by the number of reconstructed Cherenkov rings: single ring or multi-ring. For the multi-ring muon events, a momentum cut requiring greater than 600 MeV/c for the most energetic muon ring is applied. There is also a minimum visible energy cut of than 600 MeV, which can determine CC ν_μ events with 90.5% and 94.9% accuracy in subGeV and multi-GeV. Only μ-like multi-ring events are considered due to poor particle identification of overlapping rings in multi-ring CCν_e events. Upmu events are subdivided between stopping and through-going events. The horizontal excess effect is not seen in distribution due to poor correlation between incoming neutrino and fitted event direction below 1 GeV.

Consistent with the up/down ratio results, the electron neutrino data are in slight excess but agree with predictions within the error range. The shape distribution between the data and Monte Carlo appear to be fairly close to one another. The apparent excess of electron neutrinos can be explained by the large uncertainty in the total neutrino flux. However, a close inspection of the muon neutrinos find that there is a deficit which varies as both a function of energy and travel length (zenith angle). This is evident in the fully and partially-contained events as well as the upward going muon distribution. If the flux and nuclear models are accurate as they appear to be, then the muon neutrinos are disappearing, or changing into something that Super-Kamiokande does not detect. This is the fundamental idea of neutrino oscillations.
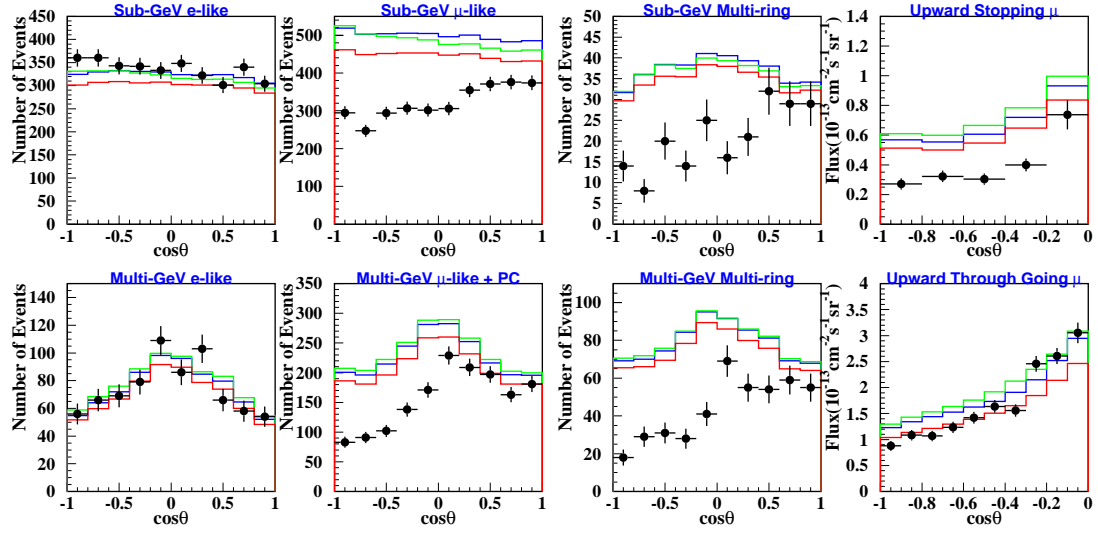
Figure 6.1: Data results for FC, PC, and upward going muons events as a function of zenith angle. The red, blue and green lines show the models from Honda3D [61], Honda1D [58], and Bartol (Gaisser et al.) [22] models respectively.

Chapter 7

NEUTRINO OSCILLATIONS AND PHENOMENOLOGY

Super-Kamiokande's atmospheric neutrino sample suffers from a glaring lack of muon neutri-
nos. Solar neutrino data from Super-K and other experiments find that there also appears to be
missing solar neutrino data as well [62, 3]. (This was discovered long before Super-K and is known
as the solar neutrino problem.) Neutrino oscillations are a favored candidate to help explain the
solar neutrino problem and this atmospheric neutrino anomaly. The idea is that a neutrino starts out
a specific flavor but has a certain time-dependent probability of being detected as a different flavor.
This probability oscillates between zero and some finite value. A corollary of neutrino oscillations
requires different masses for the neutrinos, while the Standard Model expects them to be massless.
The concept of neutrino oscillations was put forth by Bruno Pontecorvo [78, 79] in 1957, and con-
sidered oscillations between neutrinos and antineutrinos. In 1962, the idea of flavor oscillations was
considered by Maki, Nakagawa, and Sakata [72]. While the premise may sound unusual, a similar
phenomena has already been shown to happen in Kaons [50].

The mathematical background in this chapter follows [73], with parts from [5].

7.1 Neutrino Oscillations in Vacuum

Neutrinos do not interact via the strong or electromagnetic force. It has primarily one fundamental
type of interaction: the weak interaction. They have some flavor basis/eigenstates that govern all
the weak interactions of neutrinos. They must also have a basis set of kinetic energy eigenstates
determining their propagation. While it may seem reasonable, there is no reason that the weak
flavor eigenstate and mass eigenstate of a neutrino should be identical. If they are not the same, then
it is possible to have neutrino oscillations.

A flavor eigenstate is made up of a linear combination of the mass eigenstates:

$$|\nu_\alpha\rangle = \sum_i U_{\alpha i}|\nu_i\rangle \tag{7.1}$$

$$|\nu_i\rangle = \sum_\alpha U_{\alpha i}^* |\nu_\alpha\rangle \tag{7.2}$$

$|\nu_\alpha\rangle$ represents the base states for the weak interactions (a e$^-$, μ, or τ neutrino,) with greek subscripts, and $|\nu_i\rangle$ represents the base states for the kinematics (also known as the mass eigenstates) with roman subscripts. $U_{\alpha i}$ is known as the (P)MNS neutrino mixing matrix, named after its inventors: Pontecorvo,Maki,Nakagawa,Sakata. It is the lepton version of the quark CKM matrix. (If $U_{\alpha i}$ were the identity matrix, then the flavor and mass eigenstates would be the same and there would be no mixing.)

The mass eigenstates obey Einstein's relativistic energy-momentum equation which states that the time evolution propagate as:

$$\frac{d}{dt}|\nu_i\rangle = -i \sum_i H_{ij}|\nu_j\rangle \tag{7.3}$$

Solutions to this equation are in the form:

$$|\nu_i(t)\rangle = \sum_i e^{-iH_{ij}t}|\nu_j(t=0)\rangle \tag{7.4}$$

The Hamiltonian H is represented by:

$$H_{ij} = \delta_{ij}(p^2 + m_i^2)^{\frac{1}{2}} \tag{7.5}$$

where m_i is the mass of $|\nu_i\rangle$. With the relativistic approximation that $(m_i \ll p)$, this equation simplifies to:

$$H_{ij} \approx \delta_{ij}\left(p + \frac{m_i^2}{2E}\right) \tag{7.6}$$

However, if the mass eigenstates have different masses, each mass eigenstate will propagate at different velocities. The mixture of mass eigenstates a flavor neutrino started with will have a different ratio of each mass eigenstate at some later time. This results in different proportions of flavor eigenstates at a different time, and there is a chance that at the time of the detection, the neutrino flavor will have changed.

The time-dependent neutrino flavor state can be written as:

$$|\nu_\beta\rangle = A_{\alpha\beta}(t)|\nu_\alpha\rangle \tag{7.7}$$

$$A_{\alpha\beta}(t) = \sum_i U_{\alpha i}U_{i\beta}^\dagger exp(-i\frac{m_i^2}{2p}t) \tag{7.8}$$

Then the probability that a flavor state α has changed to a different flavor state β becomes:

$$P(\alpha \rightarrow \beta) = |A_{\alpha\beta}|^2 \tag{7.9}$$

7.2 Two-flavor Vacuum Oscillations

The mathematics are simplified by considering only two flavor oscillations: oscillations that only occur between two neutrino types. The mixing matrix can be simplified as:

$$U = \begin{pmatrix} \cos\theta & \sin\theta \\ -\sin\theta & \cos\theta \end{pmatrix} \tag{7.10}$$

Since there does not seem to be any deficit of electron neutrinos, the explanations here will assume two-flavor oscillations between ν_μ and ν_τ. (This is not the only possible choice, but it ends up being the simplest and correct one.) The mixing angle between muon and tau neutrino flavor eigenstates is referred to as θ_{23}. ("1" is normally associated with electron neutrinos and its corresponding mass eigenstate.) Combining Equations 7.10 and 7.8 to find the time dependent probability of going from ν_μ to ν_τ is straightforward:

$$\text{Flavor basis: } \nu_\mu = \begin{pmatrix} 1 \\ 0 \end{pmatrix} \quad : \quad \nu_\tau = \begin{pmatrix} 0 \\ 1 \end{pmatrix}$$

$$\text{Mass basis: } \nu_\mu = \begin{pmatrix} \cos\theta_{23} \\ -\sin\theta_{23} \end{pmatrix} \quad : \quad \nu_\tau = \begin{pmatrix} \sin\theta_{23} \\ \cos\theta_{23} \end{pmatrix}$$

$$U(t) = \begin{pmatrix} e^{-i\frac{m_2^2}{2E}t} & 0 \\ 0 & e^{-i\frac{m_3^2}{2E}t} \end{pmatrix}$$

$$
\begin{aligned}
A_{\nu_\mu \to \nu_\tau} &= \langle \tau | U(t) | \mu \rangle \\
&= \begin{pmatrix} -\sin\theta_{23} & \cos\theta_{23} \end{pmatrix} \begin{pmatrix} e^{-i\frac{m_2^2}{2E}t} & 0 \\ 0 & e^{-i\frac{m_3^2}{2E}t} \end{pmatrix} \begin{pmatrix} \cos\theta_{23} \\ -\sin\theta_{23} \end{pmatrix} \\
&= -\sin(\theta_{23})\cos(\theta_{23})e^{-i\left(\frac{m_2^2}{2E}t\right)} - \sin(\theta_{23})\cos(\theta_{23})e^{-i\left(\frac{m_3^2}{2E}t\right)} \\
&= -\sin(\theta_{23})\cos(\theta_{23})\left(e^{-i\left(\frac{m_2^2}{2E}t\right)} + e^{-i\left(\frac{m_3^2}{2E}t\right)} \right)
\end{aligned}
$$

$$\text{Probability} = |A_{\nu_\mu \to \nu_\tau}|^2 = \sin^2(\theta_{23})\cos^2(\theta_{23})\left(2 + e^{-i\left(\frac{m_2^2}{2E}t - \frac{m_3^2}{2E}t\right)} + e^{-i\left(-\frac{m_2^2}{2E}t + \frac{m_3^2}{2E}t\right)} \right)$$

$$
= \sin^2(\theta_{23})\cos^2(\theta_{23})\left(2 + e^{i\left(\frac{\Delta m^2}{2E}t\right)} + e^{-i\left(\frac{\Delta m^2}{2E}t\right)}\right)
$$

$$
= \sin^2(\theta_{23})\cos^2(\theta_{23})\left(2 + 2\cos\left(\frac{\Delta m^2}{2E}t\right)\right)
$$

$$
= 4\sin^2(\theta_{23})\cos^2(\theta_{23})\sin^2\left(\frac{\Delta m^2}{4E}t\right)
$$

$$
= \sin^2(2\theta_{23})\sin^2\left(\frac{\Delta m^2}{4E}t\right)
$$

where $\Delta m^2 = m_3^2 - m_2^2$ is defined as the mass squared difference between the two mass eigenstates. The probability for a two flavor oscillation for a relativistic neutrino (with all units) is:

$$
P(\nu_\mu \rightarrow \nu_\tau) = \sin^2(2\theta_{23})\sin^2\left(\frac{1.27\Delta m^2(\text{eV}^2)L(\text{km})}{E(\text{GeV})}\right) \tag{7.11}
$$

where L is the distance the neutrino has propagated, E is the energy of the neutrino, and the factor of 1.27 comes from the remaining constants $10^3/(4\hbar c)$. Here the time has been replaced with the distance the neutrino has traveled.

Two components characterize the oscillation:

Neutrino Mixing Angle θ: $\sin^2(2\theta)$ is the amplitude of the oscillation, and θ is a measurement of how much the flavor eigenstates and mass eigenstates overlap each other. $\theta = 45°$ is the maximal mixing case: an eigenstate in one base is made up by equal sized components in the other base. If θ is maximal then the probability (amplitude) can range from zero to one, completely changing the flavor into the other flavor state at a later time. (If the mixing angle is zero then the flavor basis and mass basis would be identical.)

Neutrino Mass Differences Δm^2: For the oscillation to occur, the mass of different eigenstates must be different, since the oscillation mechanism relies on the mass-squared differences between mass states. Δm^2 determines the frequency of the oscillation. If the value of Δm^2 is relatively large, then the oscillation will take place quickly and the probability of changing flavor averages to $\frac{1}{2}\sin^2(2\theta)$ (the second sine function averages to 1/2). If it is relatively small, then the oscillation takes place slowly and there may not be any sizeable oscillation.

An oscillation analysis can measure tiny ($<$ eV) mass splittings which is smaller than any current neutron decay experiment mass limit.

A Physical Analogy of Oscillations
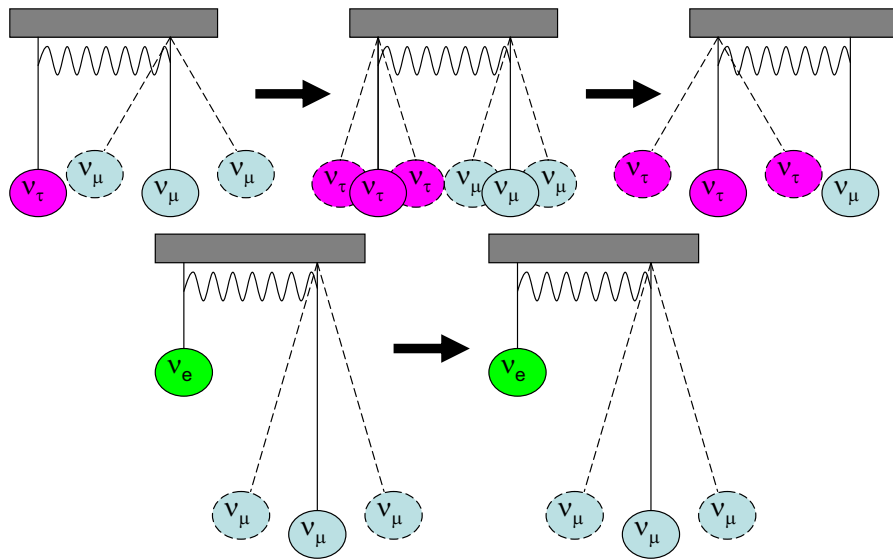
Figure 7.1: A pendula analogy of 2 flavor oscillations

2-flavor neutrino oscillations can be compared to two hanging masses [6] (See Figure 7.1. Consider two neutrinos of different flavors(pendula) have a mixing angle(connected by a spring). Movement of the pendula corresponds to existence of that flavor. If they are maximally mixed, then consider the case where the pendula are equal lengths (top of Figure 7.1). A neutrino starting as one flavor corresponds to a single pendula moving. As time goes on, the neutrino begins to oscillate to another flavor as some of the movement transfers to the other pendula. Soon both are moving with equal amplitudes and each has a 50% detection probability. As more time goes by, all of the movement is transferred to the second pendula, and now the second is 100% likely to be detected. Eventually the motion transfers back to the first pendula, and the process repeats itself between single and dual moving pendulas.

In the other case, very little mixing resembles two pendula with two very different lengths (bottom

of Figure 7.1). Even after long periods of time there will very little movement transfer, and only the original neutrino is likely to be detected.

7.2.1 Oscillations in Matter

Neutrinos can have weak interactions when traversing through matter. They can be absorbed or scattered, but this cross section is very small, proportional to square of Fermi constant. However, coherent NC and CC scattering have a terms proportional to characteristics of the matter density, which can make a noticeable effect to the vacuum neutrino oscillations. The NC channel is neutrino flavor-independent, but electron neutrinos also experience CC scattering off of electrons. Contributions to the Hamiltonian can be written as:

$$H_{e^- \text{ CC scattering}} = \sqrt{2} G_F N_{e^-} \tag{7.12}$$

$$H_{\text{NC scattering}} = \sqrt{2} G_F \frac{-N_n}{2} \tag{7.13}$$

where N_{e^-} is the electron density, N_n is the neutron density, and G_F is Fermi's constant. (The Hamiltonians have opposite signs for antineutrinos.) These Hamiltonians can create a different effective neutrino masses in matter. This is known as the MSW effect, and was postulated by both Wolfenstein [97] and Mikheyev and Smirnov [74] as a solution to the solar neutrino problem. It can create oscillations from massless neutrinos, and can change the oscillation mechanism for massive neutrinos.

However, mu and tau neutrinos both are only affected by the same NC scattering term in matter. Therefore, in the Hamiltonian the mass squared differences can be written the same as the vacuum case, and matter effects do not noticeably change 2-flavor $\nu_\mu - \nu_\tau$ oscillations. But a three flavor scenario involving mu and tau neutrinos will be altered since there are oscillations involving electron neutrinos. Additionally, if there exist sterile neutrinos which do not have NC scattering, there can be matter effects in $\nu_\mu - \nu_{sterile}$ oscillations.

The Hamiltonian for two flavor oscillations involving electron neutrinos and some other flavor (labeled χ, with corresponding mass eigenstate x) in matter after converting from flavor basis to mass basis can be written as:

$$H = \begin{pmatrix} \frac{m_1^2}{2E} + \sqrt{2} G_F N_e \cos^2 \theta_{1x} & \sqrt{2} G_F N_e \sin \theta_{1x} \cos \theta_{1x} \\ \sqrt{2} G_F N_e \sin \theta_{1x} \cos \theta_{1x} & \frac{m_x^2}{2E} + \sqrt{2} G_F N_e \cos^2 \theta_{1x} \end{pmatrix}$$

This can be diagonalized to:

$$\nu_1' = \nu_e \cos\theta_{MSW} - \nu_\chi \sin\theta_{MSW}$$

$$\nu_x' = \nu_e \sin\theta_{MSW} + \nu_\chi \cos\theta_{MSW}$$

where the mixing angle is defined as:

$$\sin^2(2\theta_{MSW}) = \frac{\sin^2(2\theta_{1x})}{(2\sqrt{2}G_F N_e \frac{E}{\Delta m^2} - \cos 2\theta_{1x})^2 + \sin^2 2\theta_{1x}} \tag{7.14}$$

Assuming a constant density this can be written in the same way as vacuum oscillations:

$$P(\nu_e \to \nu_x) = \sin^2 2\theta_{MSW} \sin^2\left(\frac{1.27\Delta M^2(\text{eV}^2)L(\text{km})}{E(\text{GeV})}\right) \tag{7.15}$$

where the effective mass difference $\Delta M^2 = \Delta m_{1x}^2 \left(2\sqrt{2}G_F N_e \frac{E}{\Delta m_{1x}^2} - \cos 2\theta_{1x}\right)^2 + \sin^2 2\theta_{1x}\right)^{1/2}$.
For small N_e ($N_e << \frac{\Delta m_{1x}^2}{2\sqrt{2}G_F E}$), the vacuum oscillation equation is restored. Large N_e ($N_e >> \frac{\Delta m_{1x}^2}{2\sqrt{2}G_F E}$) limits the amplitude of the oscillation to $1/(2\sqrt{2}G_F N_e \frac{E}{\Delta m_{1x}^2})^2$. Resonance occurs when $\sin\theta_{MSW} = 1.0$ and $\frac{\Delta m_{1x}^2}{2E}\cos 2\theta_{1x} = \sqrt{2}G_F N_e$ which enhances the oscillations. Note that for resonance to occur, $\Delta m_{1x}^2 \neq 0$.

7.2.2 *Three-Flavor Oscillations*

It will be shown in section 8.4 that the missing neutrino phenomena can be well explained by 2-flavor oscillations. However, solar neutrinos also appear to oscillate but among different neutrino flavors [62, 3]. Since there are three types of neutrinos, it seems likely that there are oscillations between the three flavor types and if there is a different oscillation mode from the solar neutrinos, then there are at least two types of neutrinos that have mass. However, 3-flavor oscillations can be written as a series of 2-flavor oscillations. This is also true for MSW effect. This is shown further in Appendix B.

Chapter 8

NEUTRINO OSCILLATIONS AND SUPER-KAMIOKANDE

Atmospheric neutrinos are generated from cosmic rays hitting our atmosphere. These cosmic rays are nearly isotropic throughout the galaxy after having their paths subject to electromagnetic and gravitational forces. Thus, the neutrinos from the atmosphere come in uniformly from all directions. Super-K's detectable neutrinos have an energy range of 200 MeV to upwards of around 100 GeV. When they arrive at SK, it may have traveled only 12 km if it came straight downwards, or 13000 km if it came directly upwards. Thus, if neutrino oscillations exist, then there is a large domain of pathlengths and energy ranges that Super-Kamiokande can look at.

Here the 2-flavor neutrino oscillation hypothesis is applied to the Super-Kamiokande Monte Carlo and tested against the data. Since there seems to be no apparent deficit of electron neutrinos, the oscillation mode is expected to be between mu and tau neutrinos. There are other analysis that presume mu-sterile neutrino oscillations [47], and also three flavor neutrino oscillations analysis [63], but will not be discussed further in this dissertation except to say that those hypothesis have been found to be less likely compared with $\nu_\mu - \nu_\tau$ oscillations.

8.1 Chi-squared Calculation

In testing the likelihood of neutrino oscillations, a chi-squared statistical analysis with the pull method is applied, looking at the differences between the data and model predictions squared for a number of histogram bins. The energy bins for FC single-ring (both e-like and μ-like,) are divided into 7 and 6 equal-spaced logarithmic bins, respectively. The FC multi-ring muon events are split by Sub-GeV (< 1330 MeV) events and Multi-GeV (≥ 1330 MeV) energies. Since there are so few PC and upward stopping and through-going muon events, they are not separated by energy but only zenith angle. A diagram of the bins is in Figure 8.1.

In addition to the 180 zenith angle bins, the analysis considers the systematic errors involved. The
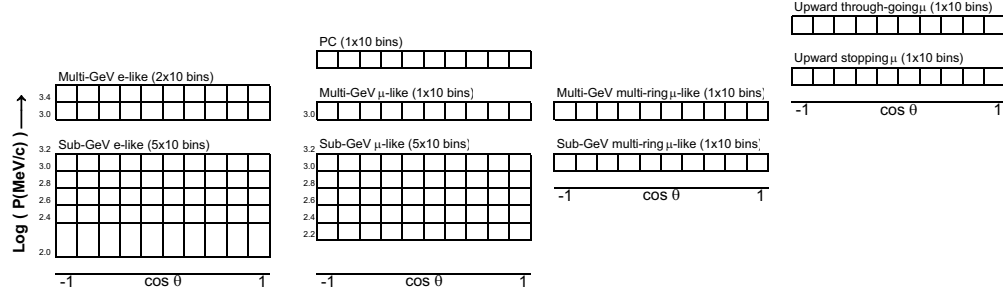
Figure 8.1: Histogram bins of the chi-squared from the zenith angle analysis.

χ^2 value with the pull method, based on a suggestion by Fogli [44], is calculated as follows:

$$\chi^2 = \sum_{i=1}^{180} \frac{(N_i^{obs} - N_i^{exp}(1 + \sum_{j=1}^{39} f_j^i \cdot \epsilon^j))^2}{(\sigma_i^{stat})^2} + \sum_{j=1}^{39} \left(\frac{\epsilon^j}{\sigma_j^{sys}} \right)^2 \tag{8.1}$$

where N_i^{obs} is the number of events observed in the ith bin, N_i^{exp} is the number expected in the $i^t h$ bin based on Monte Carlo projections, σ_i^{stat} is the combination of statistical errors for both data and MC, f_j^i is the fractional change in the predicted event rate of the ith bin due to the variation of the 39 systematic uncertainties ϵ_j. The first χ^2 sum depends greatly on the N_i^{exp} and its systematic variations, which include the neutrino flux, interactions, and the detector performance. The second sum in Equation 8.1 considers the contributions from the systematic uncertainties in the neutrino rates. The "pull method" provides insight as to which systematic errors contribute most to the chi-squared value. If a best fit ϵ_j value is significantly larger than the estimated σ value, then the results indicate that further study of that systematic is needed.

When trying to find the best fit for a given N_i^{exp} model, the 39 ϵ_j are varied until finding a minimum value for χ^2. At the minimum χ^2, $\frac{\partial \chi^2}{\partial \epsilon_j} = 0$. Then 39 linear equations need to be solved:

$$\sum_{j=1}^{39} \left[\frac{1}{(\sigma_j^{sys})^2} \delta_{jk} + \sum_{i=1}^{180} \left(\frac{N_i^{exp} \cdot N_i^{exp} \cdot f_j^i \cdot f_k^i}{(\sigma_i^{stat})^2} \right) \right] \cdot \epsilon_k = \sum_{i=1}^{180} \frac{(N_i^{obs} - N_i^{exp}) \cdot N_i^{exp} \cdot f_k^i}{(\sigma_i^{stat})^2} \tag{8.2}$$

8.2 Systematic Uncertainties

Below is a brief description of the 39 systematic uncertainties in the analysis.

Absolute normalization of the neutrino flux The absolute normalization of the flux is not well known thus it has a large error: 20% below 100 GeV and 30% above 100 GeV. When considering a best-fit, the normalization is kept free in the analysis and does not contribute to the χ^2.

Flux ratios Several different types of flux ratios are considered. The flavor ratios (muon to electron neutrinos) are calculated within 3%. The $\overline{\nu}/\nu$ ratio is considered to be within 5% for both electron and muon neutrinos. The flux uncertainties increase log-linearly from 5 GeV to 100 GeV. The up/down asymmetry ratio depends on the energy due to the rigidity cutoff. The source of the errors are due to horizontal enhancement near horizon, which are also based on energy for the horizontal/vertical neutrino ratio. For both the directional and flavor ratios the uncertainties have individual values based on energy, and in the directional cases they are also split by event type but all errors are assumed to be fully correlated.

K/π **Ratio** The Kaon to pion production ratio from cosmic ray interactions affects the number of muon to electron neutrinos in the atmosphere over the entire energy region is estimated to within 20%. This affects the flux calculations, especially for high energy neutrinos, as K decays into muons and muon neutrinos but no electron neutrinos.

Production Height and Path Length To test atmospheric neutrino oscillations it is important to accurately model the path length a neutrino has travelled before reaching the detector. For a neutrino coming up through the Earth, the flight path can be reasonably estimated with geometry within a small percentage of error. Based on the zenith angle the path length is calculated to be the altitude production height (roughly 15km) plus 2 (R $_{Earth}$+15km))cos θ_{zenith}, where the radius of the Earth R$_{Earth}$ is 6371.0 kilometers, a compromise of the polar and equatorial radii and the semimajor axis. The lifetimes of low-energy π and K are relatively short and decay to neutrinos at almost the same spot at the cosmic ray interaction. For upward going neutrinos this variance in production height minimally affects the calculation because of the long path length. However, for neutrinos arriving in Super-K from the horizon and above, the path length calculation depends greatly on the production height, which can vary as a function of energy. It is modeled by Monte Carlo method, shown in figure 8.2. The uncertainty in the

path length calculation is related to the structure of the atmosphere, which is in the MC. The size of the systematic error is found by changing the density of the atmosphere by 10% and comparing the difference in flight lengths.
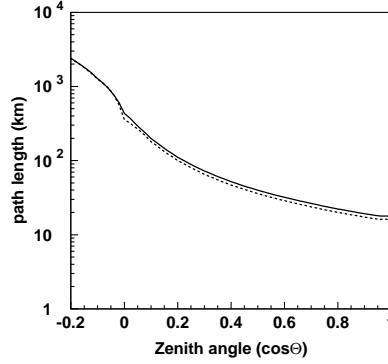
Figure 8.2: Neutrino Path Length in air. The solid line shows the predicted path length, and the dotted line shows the change in path length by compressing the air density by 10%. This effect is calculated assuming 2-flavor neutrino oscillations with parameters $(\sin^2(2\theta), \Delta m^2) = (1.0, 2.0 \times 10^{-3} \text{eV}^2)$

Energy Spectrum The primary cosmic ray energy spectrum is based on proton spectra and fitted with a power law, but the power law that fits the high energy rays is not a good fit to the low energy rays. They are treated seperately, with the flux fit to $E^{2.74}$ for energies below 100 GeV, and $E^{2.71}$ above. The uncertainty values for the spectral index above and below 100 GeV are 0.05 and 0.03 respectively, found by taking a flux weighted average of the errors by changing around a reference energy of 10 GeV. The two uncertainties are assumed to be correlated.

Sample by sample normalization A comparison of energy spectra between different flux predictions reveals a significant difference that cannot be accounted by a spectral index uncertainty and flux normalization. The sample-by-sample normalization is the relative normalization, with an uncertainty assigned 5%. It is only applied to FC Multi-GeV, PC, and upward stopping muons so not to be double counted with the absolute flux and energy spectrum systematics.

Neutrino Interaction Uncertainties (scattering, cross sections) This includes quasielastic scattering and single/multiple pion production. The kinematics and cross sections are predicted by the models described earlier whose results are confirmed by experimental data. For quasielastic and single pion modes, the axial vector mass is assumed to a 10% uncertainty. In most cases the uncertainties are a conservative fixed percentage, with the exception in the nuclear effect, which is found by comparing the difference between two independent models of the neutrino interacting with the ^{16}O nucleus. A 20% uncertainty is also considered for the NC/CC ratio. The oscillation analysis considers the possibility of CC ν_τ events in the sample, but ignores ν_μ's from tau neutrino oscillations. The uncertainty in the tau neutrino cross section is estimated at 30%.

FC/PC Reduction/Normalizations Reduction efficiencies are found by comparing data and Monte Carlo distributions on each reduction cut. The normalization errors include FC/PC separation errors, fiducial volume, hadron simulation, and non-neutrino backgrounds. These are also found by comparing data and Monte Carlo distributions.

Separation of Events(up stop/thru, ring counting, particle ID) Upward going muon classes are determined by the number of OD PMT's that have a signal 8 meters from the exit point. Errors for stopping and through-going muons are assumed to be correlated. Ring count is found by an evaluation function, and the errors for single and multi-ring separation are largely dependent on water transparency and hadron tracking in water. Errors in ring counting are also assumed as fully correlated. A likelihood method is used to identify between e and μ-like events. The uncertainty in each separation is found by comparing data and MC distributions, and are anti-correlated between e-like and μ-like. For single/multi-ring separation and particle identification, the uncertainties in the separation are assumed to be correlated.

Energy Calibration (FC events, Upmus, Up/Down symmetry) The absolute energy scale uncertainty is estimated at 2%. For upward stopping muons, events with with less than 1.6 GeV are cut for performance reasons, with a uncertainty in the cut of 1.1%. Up/down asymmetry energy scale is found by comparing decay electrons with cosmic rays, and estimated at 0.6%.

In-depth descriptions of the systematic uncertainties can be found in [64].

8.3   No Oscillation

The first test is to assume no oscillations occur and the data counts are within statistical reason. The null oscillation hypothesis yields $\chi^2_{min} = 478.7/179$ d.o.f. when analyzed with the chi-squared method. Assuming flux models and interactions are modeled correctly, no neutrino oscillations are highly unlikely.

8.4   2-flavor Neutrino Oscillation

Two-flavor $\nu_\mu - \nu_\tau$ oscillations are applied to the Super-Kamiokande I data. The best fit parameters calculate $\chi^2_{min} = 174.8/178$ degrees of freedom, with $(\sin^2(2\theta_{23}), \Delta m^2_{23}) = (1.00, 2.1 \times 10^{-3} eV^2)$. The changes to the zenith angle plots are shown in Figure 8.4. A global result which includes the nonphysical $(\sin^2(2\theta_{23}) > 1.0)$ region finds a $\chi^2_{unphys} = 174.5/178$ d.o.f. at $(\sin^2(2\theta_{23}), \Delta m^2_{23}) = (1.02, 2.1 \times 10^{-3} eV^2)$. The 90% confidence level region is bounded by $sin^2(2\theta) > 0.92$, $1.5 \times 10^{-3} < \Delta m^2 < 3.4 \times 10^{-3}$ eV^2. The contour plot is shown in Figure 8.3. A summary of the systematic error parameters is found in Tables 8.1, 8.2, 8.3, and 8.4.

The degrees of freedom are the 180 zenith angle bins plus the 38 systematic constraints, the subtracting 39 minimized parameters and the 2 oscillation parameters, $(\sin^2(2\theta_{23}), \Delta m^2_{23})$. Since the absolute normalization parameter is free, it does not count toward the systematic constraints. In the null hypothesis case, there are 179 d.o.f. because the absolute normalization is used as a constraint and there are no oscillation parameters.

As a further check, the oscillation analysis can be broken down by treating the different event types and energy as independent subsamples. The resulting contour is shown in Figure 8.5. The resulting contours are consistent with each other and the combined result.

While oscillations were previously considered as an possible explanation to the missing neutrinos, the analysis from Super-K was the first to show it to be a likely candidate. Further analysis has found it to be favored over other possible disappearance mechanisms (decay, decoherence) [14]. If neutrinos do oscillate then perhaps it can be used to explain other unknown physics phenomena.
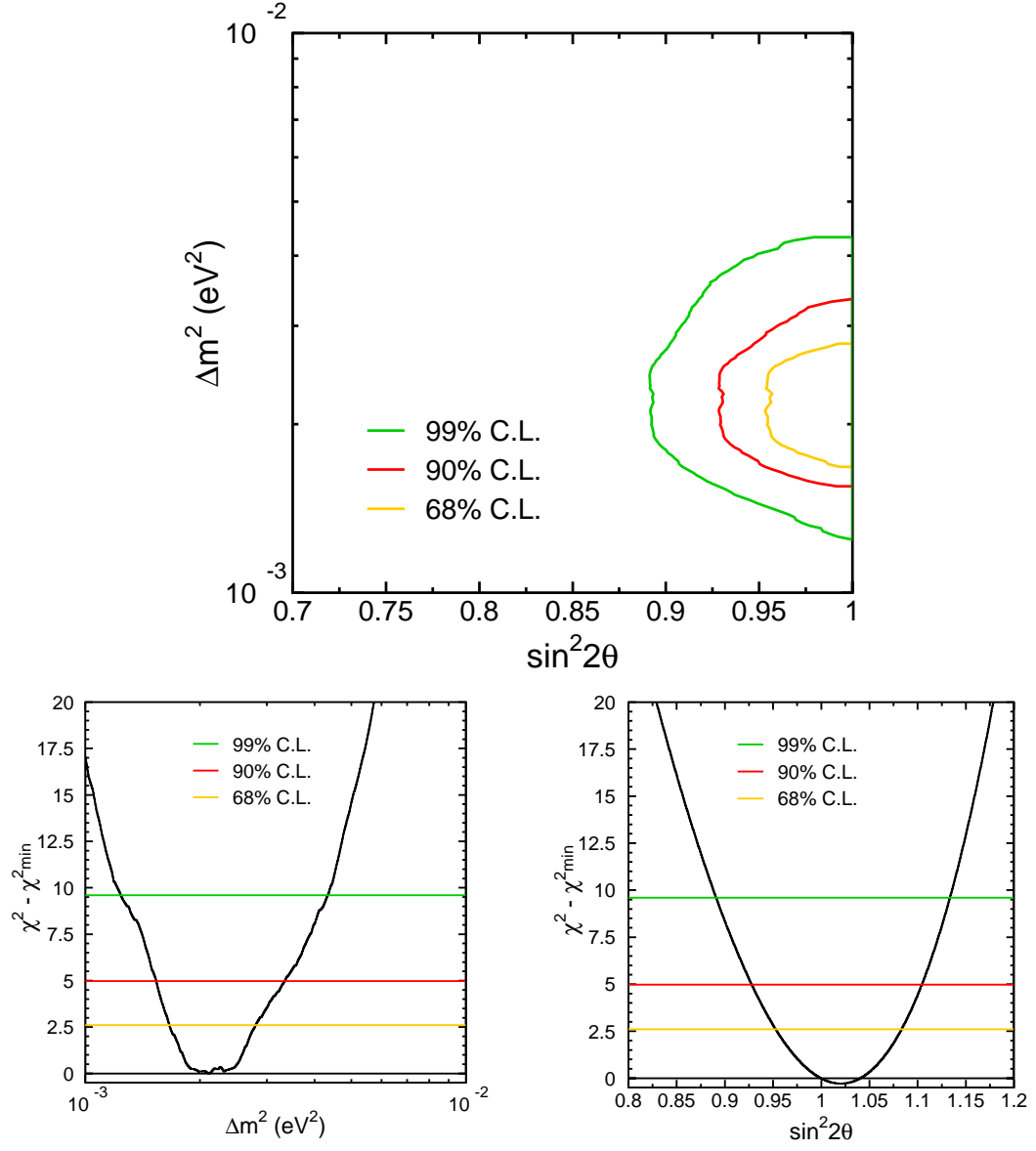
Figure 8.3: Contours of the best fit parameters. The lower plots show the cross sections of $\chi^2 - \chi^2_{min} = 174.8/178$ d.o.f. at $\sin^2(2\theta) = 1.0$, $\Delta m^2 = 2.1 \times 10^{-3} eV^2$), respectively.
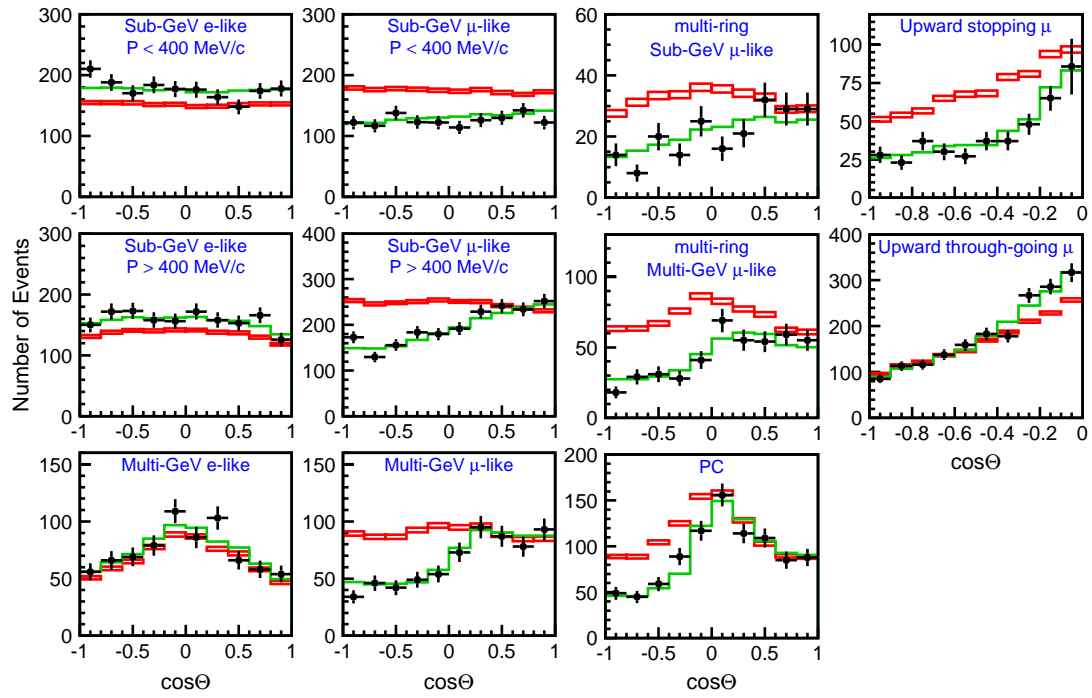
Figure 8.4: Histogram bins of the zenith angle analysis for different event types and energy. The red boxes show the non-oscillated MC prediction, green showing the oscillated MC, and crosshairs show the data. The crosshairs only reflect statistical errors.

Table 8.1: Systematic errors in neutrino flux for standard two flavor oscillations.

Chi-square Contribution			$\sigma\%$	Best-Fit
Systematic Uncertainties in neutrino flux				
Absolute Normalization			free	11.0
$(\nu_\mu + \overline{\nu_\mu})/(\nu_e + \overline{\nu_e})$	$E_\nu < 5$ GeV		3.0	-2.4
	$E_\nu > 5$ GeV		3.0	0.2
$\nu_e/\overline{\nu_e}$	$E_\nu < 10$ GeV		5.0	1.5
	$E_\nu > 10$ GeV		5.0	0.0
$\nu_\mu/\overline{\nu_\mu}$	$E_\nu < 10$ GeV		5.0	-1.3
	$E_\nu > 10$ GeV		5.0	0.9
Up/down	< 400 MeV	e-like	0.5	0.2
		μ-like	0.8	0.3
	> 400 MeV	e-like	2.1	0.9
		μ-like	1.8	0.8
	Multi-GeV	e-like	1.5	0.7
		μ-like	0.8	0.3
	PC		0.4	0.2
	Sub-GeV multi-ring μ		0.8	0.3
	Multi-GeV multi-ring μ		0.7	0.3
Horizontal / Vertical	< 400 MeV	e-like	0.3	0.0
		μ-like	0.3	0.0
	> 400 MeV	e-like	1.2	0.1
		μ-like	1.2	0.1
	Multi-GeV	e-like	2.8	0.2
		μ-like	1.9	0.1
	PC		1.4	0.1
	Sub-GeV multi-ring μ		1.5	0.1
	Multi-GeV multi-ring μ		1.3	0.1

K/π ratio		20.0	-6.3
L_ν (production height)		10	-0.6
Energy spectrum	$E_k < 100$ GeV	0.03	0.031
	$E_k > 100$ GeV	0.05	0.052
Sample-by-sample	FC Multi-GeV	5.0	-5.2
	PC + upward stopping μ	5.0	-3.9

Table 8.2: Systematic errors in the neutrino interaction for standard two flavor oscillations.

Chi-square Contribution	$\sigma\%$	Best-Fit
Systematic uncertainties in neutrino interaction		
M_A in quasi-elastic and single-π	10.0	0.5
Quasi-elastic scattering (model dependence)	1.0	-0.95
Quasi-elastic scattering (cross-section)	10.0	5.6
Single meson production (cross-section)	10.0	-4.7
Multi-pion production (model dependence)	1.0	1.47
Multi-pion production (total cross-section)	5.0	-0.2
Coherent pion production (total cross-section)	30.0	0.4
NC/CC ratio	20.0	2.9
Nuclear effect in ^{16}O	30.0	-7.2
Energy spectrum in pions	1.0	0.5
CC ν_τ interaction cross section	30.0	0.2

Table 8.3: Systematic errors in the event selection for standard two flavor oscillations.

Chi-square Contribution			$\sigma\%$	Best-Fit
Systematic uncertainties in event selection				
Reduction for Fully Contained Event			0.2	0.0
Reduction for Partially Contained Event			2.6	0.3
Detection Efficiency	upward stopping μ		1.3	-0.2
	upward through-going μ		0.5	-0.1
FC/PC Separation			0.9	-0.3
Hadron Simulation			1.0	-0.24
Non-ν Background	Sub-GeV	e-like	0.4	0.1
		μ-like	0.1	0.0
	Multi-GeV	e-like	0.2	0.0
		μ-like	0.1	0.0
	PC		0.2	0.0
Upward stopping/through-going muon separation			0.4	0.0

Table 8.4: Systematic errors in the event reconstruction for two flavor oscillations.

Chi-square Contribution			$\sigma\%$	Best-Fit
Systematic uncertainties in event reconstruction				
Ring separation	<400 MeV	e-like	6.3	2.6
		μ-like	2.4	1.0
	>400 MeV	e-like	3.4	1.4
		μ-like	1.3	0.5
	Multi-GeV	e-like	15.9	6.5
		μ-like	6.2	2.5
	Sub-GeV multi-ring μ		3.7	-1.5
	Multi-GeV multi-ring μ		7.2	-2.9
Particle identification	Sub-GeV	e-like	0.6	0.2
		μ-like	0.6	-0.2
	Multi-GeV	e-like	0.4	0.1
		μ-like	0.4	-0.1
	Sub-GeV multi-ring μ		3.4	-0.9
	Multi-GeV multi-ring μ		4.7	-1.2
Energy calibration for FC event			2.0	0.4
Energy cut for upward stopping muon			1.1	-0.2
Up/down symmetry of energy calibration			0.6	0.0
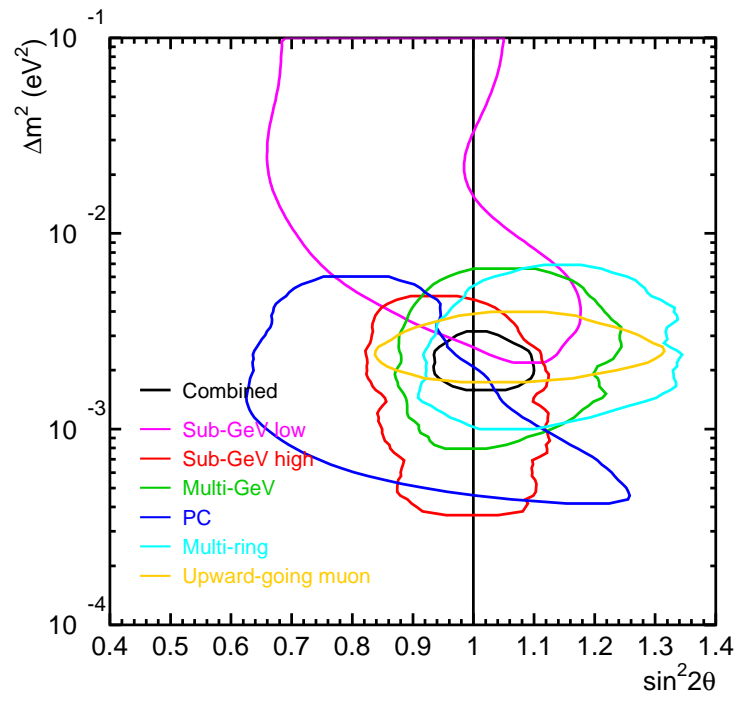
Figure 8.5: Contour for oscillation analysis applied to different event types and energy.

Chapter 9

ENVIRONMENT-DEPENDENT NEUTRINO OSCILLATIONS

Two-flavor $\nu_\mu - \nu_\tau$ oscillations have been shown to be a likely candidate to explain the atmospheric neutrino anomaly. But there are still many unanswered questions in nuclear physics and cosmology that could be answered with neutrinos. It is important to continue testing neutrino models that answer not only questions of neutrino disappearance but also other physics phenomena.

9.1 Matter-Only Neutrino Oscillations

Neutrino experiments with significant ($> 50\%$) air pathlength [12, 9, 40] have been consistent with no oscillations. Here a simple hypothesis that assumes oscillations only occur in high-density matter(HDM) (not air or vacuum) is tested. In this text "HDM" and "rock" are used interchangeably. The mixing angle is constant in HDM. The 2-flavor oscillation model becomes:

$$P(\nu_\mu \to \nu_\mu) = 1 - sin^2(2\theta)sin^2\left(\frac{1.27\Delta m^2(eV^2)L_{ROCK}(km)}{E\nu(GeV)}\right) \tag{9.1}$$

where L_{ROCK} is the neutrino pathlength in the HDM (Earth or mountain rock) going to Super-Kamiokande. This length is extremely sensitive to the direction that the neutrino travels. While an upward neutrino still passes through about 13000 kilometers, a downward neutrino passes through the surrounding mountain, which is less than 2-10 kilometers and not azimuth symmetric. The previous air and rock oscillation case has approximately 20-300 km downward pathlength, which is a large difference, while upward going is pathlength are nearly the same in the two models.

9.1.1 Neutrino Pathlength in Matter

A profile of the mountain surrounding Super-Kamiokande is needed to duplicate the neutrino pathlengh in rock. Terrain maps are taken from the United States Geological Survey (USGS) agency's Digital Elevation Maps (DEMs), with data points 7.5 minute (30 meters) spacing [1]. The surface data

---

[1]Downloaded April 2006 from http://seamless.usgs.gov

was obtained from the Shuttle Radar Topography Mission (SRTM), using a version of radio wave interferometry with two antenna separated by 60 meters aboard the Space Shuttle Endeavor. From the contour maps a 10 kilometer radius is considered around the Super-Kamiokande detector.
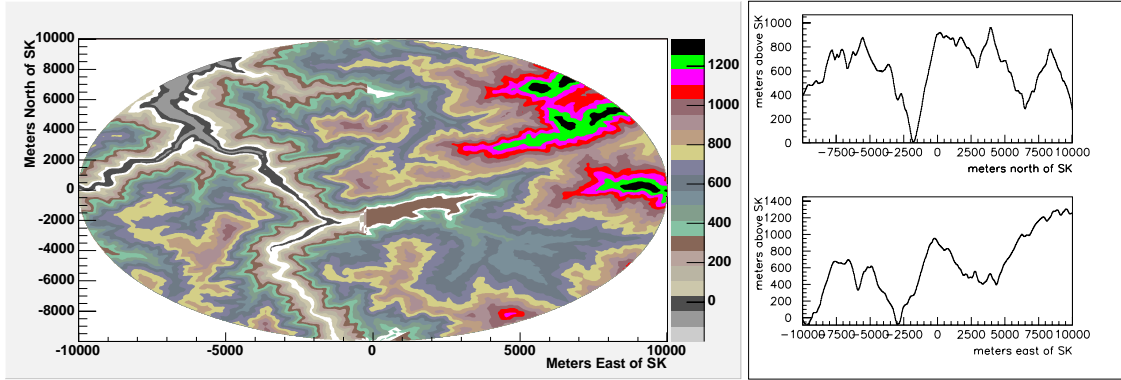
Figure 9.1: Profile of Mt.Ikeno surrounding Super-Kamiokande. The origin is located at the center of Super-Kamiokande's detector tank. The left figure shows a contour map of the area. On the right is the cross section view along the north-south and east-west axes, respectively.

9.1.2   Changes made to the Chi-squared analysis

The path length of a neutrino coming upward is calculated the same way as earlier after removing the production height from the algorithm. By using the zenith angle the path length is estimated at $2(R_{Earth})\cos\theta_{zenith}$. For a downward neutrino, the direction of the neutrino and profile of the mountain is used to calculate how much rock the neutrino passed through. In the case of a horizontal neutrino, a flat path of 12 km is used to account for surrounding mountain ranges.

Because it is not clear how the path length systematic error is used in this test, it is removed from the 39 systematic errors in the chi-squared calculation.

9.2   Results of Matter Neutrino Oscillation Analysis

Figures 9.2 compares the zenith angle distribution for both "standard" two flavor oscillations (which oscillate equally in all environments), and for a rock-oscillation case. There appear to be only minor discrepancies between the two models in the zenith angle bins. Figure 9.3 overlays the best

fit parameters on a χ^2 contour map for rock oscillations and the standard oscillations. The chi-squared likelihood of matter-only oscillations is 189.748/178 d.o.f. at $(\sin^2(2\theta_{23}), \Delta m^2_{23}(\text{eV}^2)) = (1.00, 2.6\times10^{-3})$ in the physical region. In the unphysical region, $\chi^2 = 188.931$/d.o.f. at $(\sin^2(2\theta_{23}), \Delta m^2_{23}(\text{eV}^2)) = (1.04, 2.6\times10^{-3})$.

9.2.1 Failure of Matter-Only Neutrino Oscillations

By the chi-squared statistic, matter-only neutrino oscillations are not a bad fit (26%) to the data. However, based on work by Lyons [70], the difference of the χ^2 value of two models can be used to discriminate hypotheses. Both models use the same parameters in the chi-squared calculation and are reasonable fits. The difference of the chi-squared is treated as having one degree of freedom, and the standard deviation is considered to be the square root of the difference. Computing this for the rock oscillation case χ^2_{ROCK}=189.748/178 d.o.f. and the standard case $\chi^2_{standard}$=174.976/178 d.o.f. (with path length systematic error removed), $\Delta\chi^2 = 14.772$. Therefore the rock-oscillation only case can be rejected at the 3.8σ level.

One major difference in the two hypothesis is the pathlength near the horizon. A rock-only oscillation experiences a sudden change in rock path length at the angle where neutrinos start to pass upward through the Earth. However, the total path length with air included is much smoother at this angle. This difference can be seen in Figure 9.2 and the standard oscillation model that considers the entire path length appears to fit the data better.

Examination of the 38 systematic errors (Tables 9.1, 9.2, 9.3, 9.4) finds several differences between the two hypotheses stand out. The largest contributing factor is the ν_μ/ν_e ratio, found in Table 9.1. A downward going neutrino has the largest difference of path length between the matter-only and total distances. The neutrino passes roughly through 15 km of air then passing through roughly 1-2 km of rock before interacting with the detector. A horizontal neutrino passes through 200+ km of air and 10 km of rock. In other words, a neutrino coming from just above the horizon for a given energy has roughly 8-20 times path length in air compared to matter-only distance. An oscillation model that uses the whole path length predicts many more oscillation cycles to occur for a given Δm^2, especially for neutrinos with lower energies. Compared with the Monte Carlo, the neutrino data counts are already low for downward going sub-GeV neutrinos. For a matter only oscillation
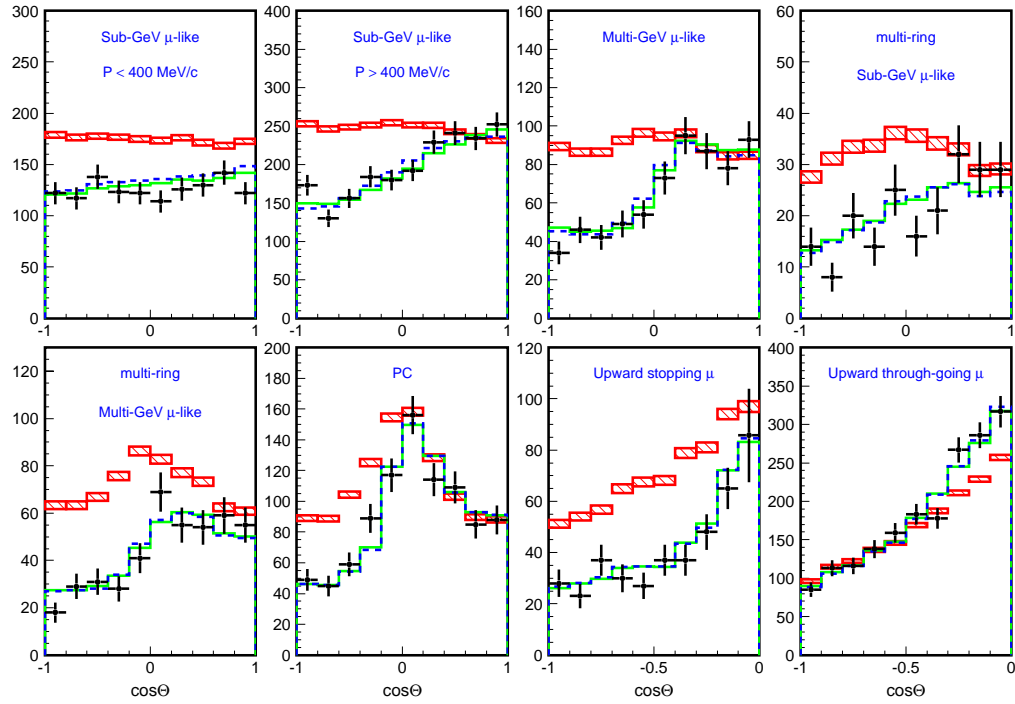
Figure 9.2: Zenith angle plots comparing "standard" 2 flavor oscillations and rock-only oscillations. The red boxes are the non-oscillated prediction. The green line are the standard 2 flavor oscillations, and the blue dashed line is the rock-only oscillations. The cross hairs are the data with statistic error only shown. The largest differences in the two models are seen near the horizon in the Sub and Multi-GeV single ring muons.
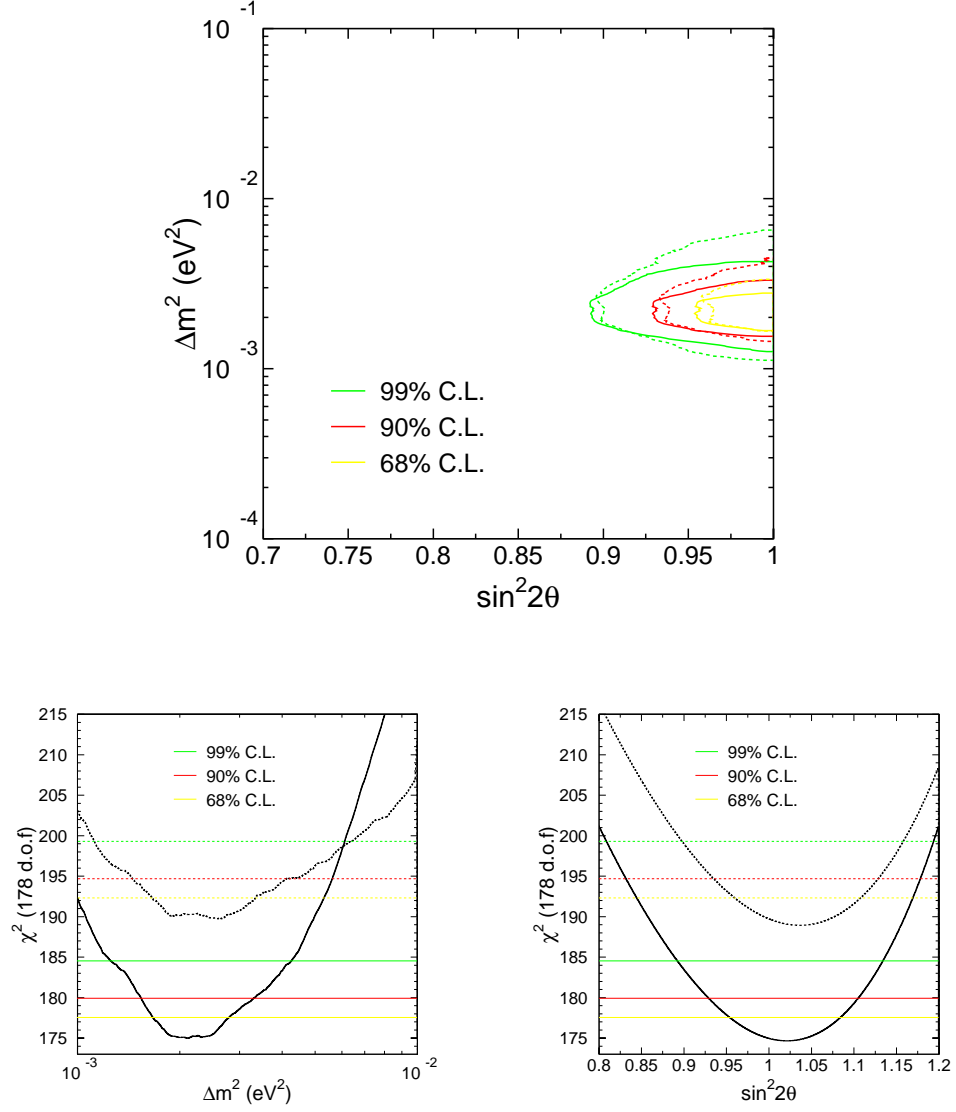
Figure 9.3: Contours of the best fit parameter for a rock only neutrino oscillation. "Standard" oscillations are represented by the solid lines, and rock oscillations are dashed. The lower plots show the cross sections of $\chi^2 - \chi^2_{min}$ at each model's χ^2 minima along the Δm^2 and $\sin^2(2\theta)$ axes, respectively. The upper dashed χ^2 lines represent the rock-only oscillations. HDM oscillations have a larger minimum χ^2_{ROCK}=189.748/178 d.o.f. compared with oscillations in all media which has $\chi^2_{Standard}$=174.976/178 in the physical region.

Table 9.1: Comparison of systematic errors in neutrino flux for "standard" two flavor oscillations and rock-only oscillations.

Chi-square Contribution			$\sigma\%$	Standard	Rock Only
Systematic Uncertainties in neutrino flux					
Absolute Normalization			free	11.0	7.8
$(\nu_\mu + \overline{\nu_\mu})/(\nu_e + \overline{\nu_e})$	$E_\nu < 5$ GeV		3.0	-2.4	-6.0
	$E_\nu > 5$ GeV		3.0	0.2	0.3
$\nu_e/\overline{\nu_e}$	$E_\nu < 10$ GeV		5.0	1.6	4.3
	$E_\nu > 10$ GeV		5.0	0.0	0.0
$\nu_\mu/\overline{\nu_\mu}$	$E_\nu < 10$ GeV		5.0	-1.3	-4.3
	$E_\nu > 10$ GeV		5.0	0.9	0.9
Up/down	< 400 MeV	e-like	0.5	0.2	0.2
		μ-like	0.8	0.3	0.4
	> 400 MeV	e-like	2.1	0.9	0.9
		μ-like	1.8	0.8	0.8
	Multi-GeV	e-like	1.5	0.7	0.7
		μ-like	0.8	0.3	0.4
	PC		0.4	0.2	0.2
	Sub-GeV multi-ring μ		0.8	0.3	0.4
	Multi-GeV multi-ring μ		0.7	0.3	0.3
Horizontal / Vertical	< 400 MeV	e-like	0.3	0.0	-0.2
		μ-like	0.3	0.0	-0.2
	> 400 MeV	e-like	1.2	0.1	-0.8
		μ-like	1.2	0.1	-0.8
	Multi-GeV	e-like	2.8	0.2	-1.2
		μ-like	1.9	0.1	-1.2
	PC		1.4	0.1	-0.9
	Sub-GeV multi-ring μ		1.5	0.1	-1.0
	Multi-GeV multi-ring μ		1.3	0.1	-0.8

K/π ratio		20.0	-6.3	-1.3
Energy spectrum	$E_k < 100$ GeV	0.03	0.031	0.031
	$E_k > 100$ GeV	0.05	0.052	0.051
Sample-by-sample	FC Multi-GeV	5.0	-5.2	-5.4
	PC + upward stopping μ	5.0	-4.2	-4.1

Table 9.2: Comparison of systematic errors in the neutrino interaction for "standard" two flavor oscillations and rock-only oscillations.

Chi-square Contribution	$\sigma\%$	Standard	Rock Only
Systematic uncertainties in neutrino interaction			
M_A in quasi-elastic and single-π	10.0	0.2	-1.3
Quasi-elastic scattering (model dependence)	1.0	-0.92	-.6
Quasi-elastic scattering (cross-section)	10.0	5.9	3.3
Single meson production (cross-section)	10.0	-4.9	-3.9
Multi-pion production (model dependence)	1.0	1.47	1.32
Multi-pion production (total cross-section)	5.0	-0.3	-0.1
Coherent pion production (total cross-section)	30.0	0.4	8.4
NC/CC ratio	20.0	3.5	-4.2
Nuclear effect in ^{16}O	30.0	-7.9	-20.5
Energy spectrum in pions	1.0	0.5	0.7
CC ν_τ interaction cross section	30.0	0.2	-1.3

Table 9.3: Comparison of systematic errors in the event selection for "standard" two flavor oscillations and rock-only oscillations.

Chi-square Contribution			$\sigma\%$	Standard	Rock Only
Systematic uncertainties in event selection					
Reduction for Fully Contained Event			0.2	0.0	
Reduction for Partially Contained Event			2.6	0.3	
Detection Efficiency	upward stopping μ		1.3	-0.2	
	upward through-going μ		0.5	-0.1	
FC/PC Separation			0.9	-0.3	
Hadron Simulation			1.0	-0.24	
Non-ν Background	Sub-GeV	e-like	0.4	0.1	
		μ-like	0.1	0.0	
	Multi-GeV	e-like	0.2	0.0	
		μ-like	0.1	0.0	
	PC		0.2	0.0	
Upward stopping/through-going muon separation			0.4	0.0	

Table 9.4: Comparison of systematic errors in the event reconstruction for "standard" two flavor oscillations and rock-only oscillations.

Chi-square Contribution			$\sigma\%$	Standard	Rock Only
Systematic uncertainties in event reconstruction					
Ring separation	<400 MeV	e-like	6.3	2.5	3.7
		μ-like	2.4	1.0	1.4
	>400 MeV	e-like	3.4	1.4	2.0
		μ-like	1.3	0.5	0.8
	Multi-GeV	e-like	15.9	6.4	9.4
		μ-like	6.2	2.5	3.7
	Sub-GeV multi-ring μ		3.7	-1.5	-2.2
	Multi-GeV multi-ring μ		7.2	-2.9	-4.3
Particle identification	Sub-GeV	e-like	0.6	0.2	0.5
		μ-like	0.6	-0.2	-0.5
	Multi-GeV	e-like	0.4	0.1	0.3
		μ-like	0.4	-0.1	0.3
	Sub-GeV multi-ring μ		3.4	-0.9	-0.4
	Multi-GeV multi-ring μ		4.7	-1.2	-0.5
Energy calibration for FC event			2.0	0.4	0.9
Energy cut for upward stopping muon			1.1	-0.2	-0.2
Up/down symmetry of energy calibration			0.6	0.0	0.1

hypothesis, the systematic errors try to compensate a lack of neutrinos by adjusting the neutrino flux. Some of these adjustments are quite large, particularly the ν_μ/ν_e ratio for energies below 5 GeV, and adjust the errors to greater than outside of one standard deviation. This does not happen in the standard case.

It is unlikely that neutrinos oscillate in only matter without any additional effects. One such effect described in the next chapter postulates that the neutrino mass (and the oscillation) may have dependence on the nuclear components of the matter it is passing through.

Chapter 10

MASS VARYING NEUTRINO OSCILLATIONS

There are theoretical models ([43, 65], or see Appendix C) that propose mass-varying neu-trinos (MaVaNs) as a source of unknown dark energy and a possible resolution to the LSND re-sults [17, 100]. The variation in the masses of such neutrinos depends on the neutrino density of its environment, and possibly even the charge density as well. If this hypothesis is correct, it may be possible to probe the electron density dependence on the mass with atmospheric neutrino oscilla-tions.

To check for the matter dependence, Δm^2 is replaced with $\Delta m^2 \times \frac{\rho_e}{\rho_o} n$, where ρ_e is the electron density of the matter in neutrino trajectory, in mole/cm^3, and n is some value of the density depen-dence. Several different values of n are be tested. ρ_0 is set at 1.00 mole/cm^3. It is assumed that the mixing angle is fixed for all densities. Two types of analysis will be carried out in this chapter. The first part only considers the pathlength in the HDM, and the second includes the air pathlength and its charge density in addition to the rock.

10.1 Electron-Density Modeling and Application

10.1.1 Earth Density

While there is a significant difference between mass densities between air and rock, there is also variation between the different layers of Earth.

- Air density is roughly 10^{-3} g/cm^3

- Rock and Earth crust density is roughly 2 g/cm^3

- Mantle density is about 5 g/cm^3

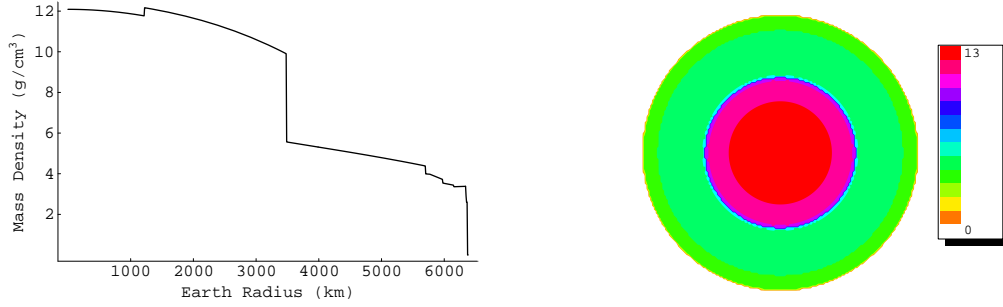- Core density is about $10 - 12$ g/cm^3

Figure 10.1: The left figure is the PREM profile of the Earth's mass density as a function of radius. The right figure shows a cross section of the Earth's density changes in units of g/cm ^{3}.

The Preliminary Reference Earth Model (PREM) model [42] is used to model the Earth's mass density profile. To approximate the electron density, the mass density of the Earth is multiplied by the mean charge to mass ratio (the sum of the relative mass abundance of elements in the dirt multiplied by its charge to mass ratio (Z/A),) quoted from [19]. The units for the electron density is mole/cm^3.

Since the electron density is not constant throughout the neutrino path in the mountain and Earth, the probability amplitude is segmented into:

$$A_{\alpha,\beta}(t) = \prod_j \sum_i U_{\alpha i} U_{i\beta}^\dagger exp \left(-i \frac{m_i^2 \times (\frac{\rho_j}{\rho_o})^n}{2p} t_j \right) \tag{10.1}$$

where t_j is the time (pathlength) spent that a neutrino takes traveling through a particular electron density ρ_j.

For a neutrino that goes through two different mediums A and B the disappearance probability becomes:

$$U_A(t_A) = \begin{pmatrix} e^{-i\frac{m_{1A}^2}{2E} t_A} & 0 \\ 0 & e^{-i\frac{m_{2A}^2}{2E} t_A} \end{pmatrix} \qquad U_B(t_B) = \begin{pmatrix} e^{-i\frac{m_{1B}^2}{2E} t_B} & 0 \\ 0 & e^{-i\frac{m_{2B}^2}{2E} t_B} \end{pmatrix}$$

$$U_B(t_B) \times U_A(t_A) = \begin{pmatrix} e^{-i\frac{m_{1B}^2 t_B + m_{1A}^2 t_A}{2E}} & 0 \\ 0 & e^{-i\frac{m_{2B} t_B^2 + m_{2A}^2 t_A}{2E}} \end{pmatrix}$$

where $m_{1A} = m_1 \times (\frac{\rho_A}{\rho_o})^n$, and similarly for m_{1B}, m_{2A}, m_{2B}. Referring back to Equation 7.11, the probability reduces to:

$$A = \langle \tau | U_B(t_B) U_A(t_A) | \mu \rangle \tag{10.2}$$

$$|A|^2 = \sin^2(2\theta_{23}) \sin\left(\frac{\Delta m_B^2}{4E} t_B + \frac{\Delta m_A^2}{4E} t_A\right) \tag{10.3}$$

This degenerates to Equations 7.11 in the case of one medium.

10.1.2 Averaging Over Oscillations

For Super-Kamiokande analysis, if a neutrino experiences more than two oscillation cycles, then the survival probability is averaged as $\frac{1}{2}\sin^2(2\theta_{23})$, because the oscillations are cycling too quickly compared to the resolution of the detector. This is done in the analysis described in Chapters 8 and 9, and there the process is relatively straightforward. A similar averaging procedure is done for testing these alternate oscillation models. For downward and horizontal neutrinos, a conservative assumption of 1 kilometer of mountain pathlength is used for angles between 0 to 89.37 degrees or 12 kilometers pathlength for horizontal neutrinos between 89.37 and 91.63 degrees, in order to speed processing time. A single average density is assumed in these cases. For upward neutrinos and muons, total pathlengths are calculated the same method as earlier. However, Equation 10.3 is used and assumes only two mediums of differing density: an average crust or mantle density, and an average core density. To approximate the densities, if the neutrino zenith angle is between 91.63 and 116.7 degrees, it uses mantle density, and after 146.9 degrees it goes through the outer core radius at 3480 kilometers. The pathlength is segmented into two mediums that have a majority of the pathlength.

10.2 Analysis without the Air Pathlength

10.2.1 $\Delta m^2 \rightarrow \Delta m^2 \times \rho/\rho_o$ Results

This analysis assumes that the mass differences between neutrinos is proportional to the electron density of the medium. The amplitude is replaced with:

$$A_{\alpha,\beta}(t) = \prod_j \sum_i U_{\alpha i} U_{i\beta}^\dagger exp\left(-i\frac{m_i^2 \times \frac{\rho_j}{\rho_o}}{2p} t_j\right) \tag{10.4}$$

The analysis finds the $\chi^2_{min} = 194.357/178$ d.o.f. of such an oscillation mode at $\sin^2(2\theta) = 1.0, \Delta m^2 = 1.23 \times 10^{-3} eV^2)$ in the physical region and $\chi^2_{min} = 193.833/178$ d.o.f. at $\sin^2(2\theta) = 1.03, \Delta m^2 = 1.19 \times 10^{-3} eV^2)$ in the unphysical region. Using the same method in Section 9.2.1, this means that this case of the mass difference being proportional to e^- density is ruled out at the 4.4 σ level when compared to the "standard" analysis (fixed mass squared difference and oscillations in all environments). The plots comparing the zenith angle bins between the two models are in Figure 10.2, and the contours are mapped in Figure 10.3 .

10.2.2 *Results of Other Density Dependences*

Other density dependent models from [75] are tested without the air pathlength. The case of no dependence (n=0) reverts back to the analysis in Section 9.1. The results are shown in Table 10.1. There appears to be no model tested that is not ruled out at the 99% confidence level. Contour and zenith angle plots can be found in Appendix D.

Table 10.1: Comparisons of χ^2 Values for Different Models without Air Path. There are 178 degrees of freedom in the χ^2 that is not reflected in the table.

| Model	Physical Region				Unphysical Region		
$\Delta m^2 \times (\rho/\rho_o)^n$	χ^2_{min}	Δm^2(eV^2)	$\sin^2(2\theta)$	$\Delta\sigma$	χ^2_{min}	Δm^2(eV^2)	$\sin^2(2\theta)$
"Standard"	174.976	2.11×10^{-3}	1.00	-	174.611	2.11×10^{-3}	1.02
$n = 2$	202.958	5.12×10^{-4}	1.00	5.3	202.585	4.95×10^{-4}	1.03
$n = 1$	194.357	1.23×10^{-3}	1.00	4.4	193.833	1.19×10^{-3}	1.03
$n = \frac{2}{3}$	193.281	1.35×10^{-3}	1.00	4.2	191.759	1.35×10^{-3}	1.05
$n = \frac{1}{3}$	191.728	1.68×10^{-3}	1.00	4.1	189.989	1.68×10^{-3}	1.06
$n = 0$	189.748	2.60×10^{-3}	1.00	3.8	188.931	2.60×10^{-3}	1.04
$n = -\frac{1}{3}$	187.346	2.92×10^{-3}	1.00	3.5	187.036	2.92×10^{-3}	1.02
$n = -\frac{2}{3}$	186.719	3.27×10^{-3}	1.00	3.4	186.469	3.27×10^{-3}	1.02
$n = -1$	187.528	3.89×10^{-3}	1.00	3.5	186.823	3.89×10^{-3}	1.03
$n = -2$	195.464	4.95×10^{-3}	1.00	4.5	193.076	4.95×10^{-3}	1.06
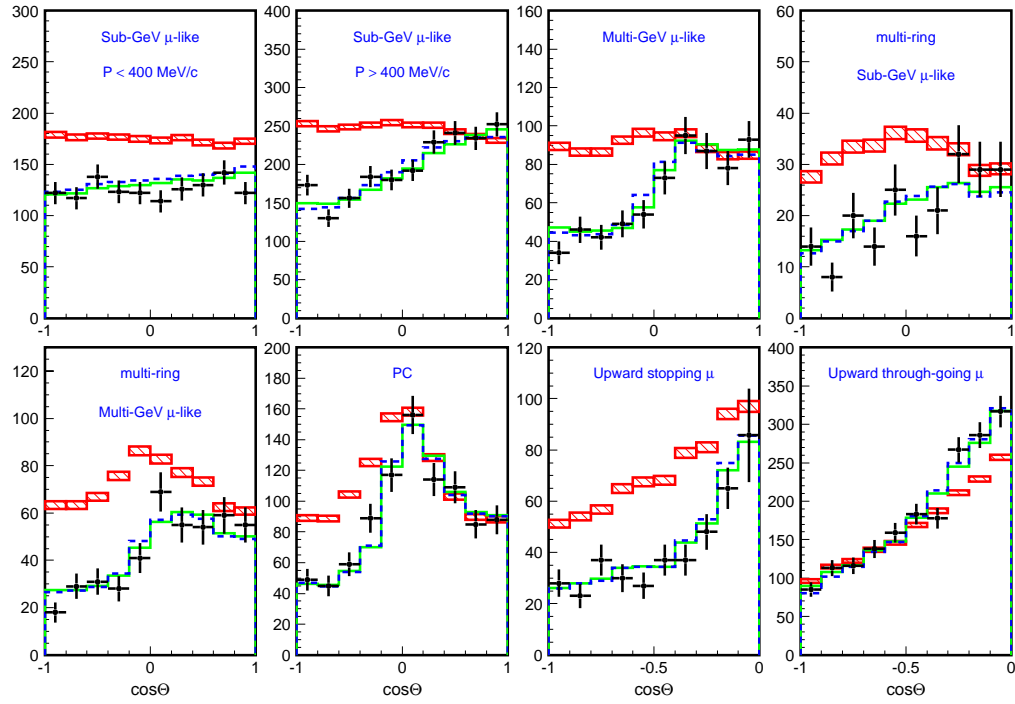
Figure 10.2: $\Delta m^2 \rightarrow \Delta m^2 \times \rho/\rho_o$ (without air pathlength). Zenith angle plots comparing "standard" 2 flavor oscillations and MaVaN oscillations. The red boxes are the non-oscillated prediction. The green line are the standard 2 flavor oscillations, and the blue dashed line is the simple MaVaN oscillations. The cross hairs are the data with statistic error only shown.
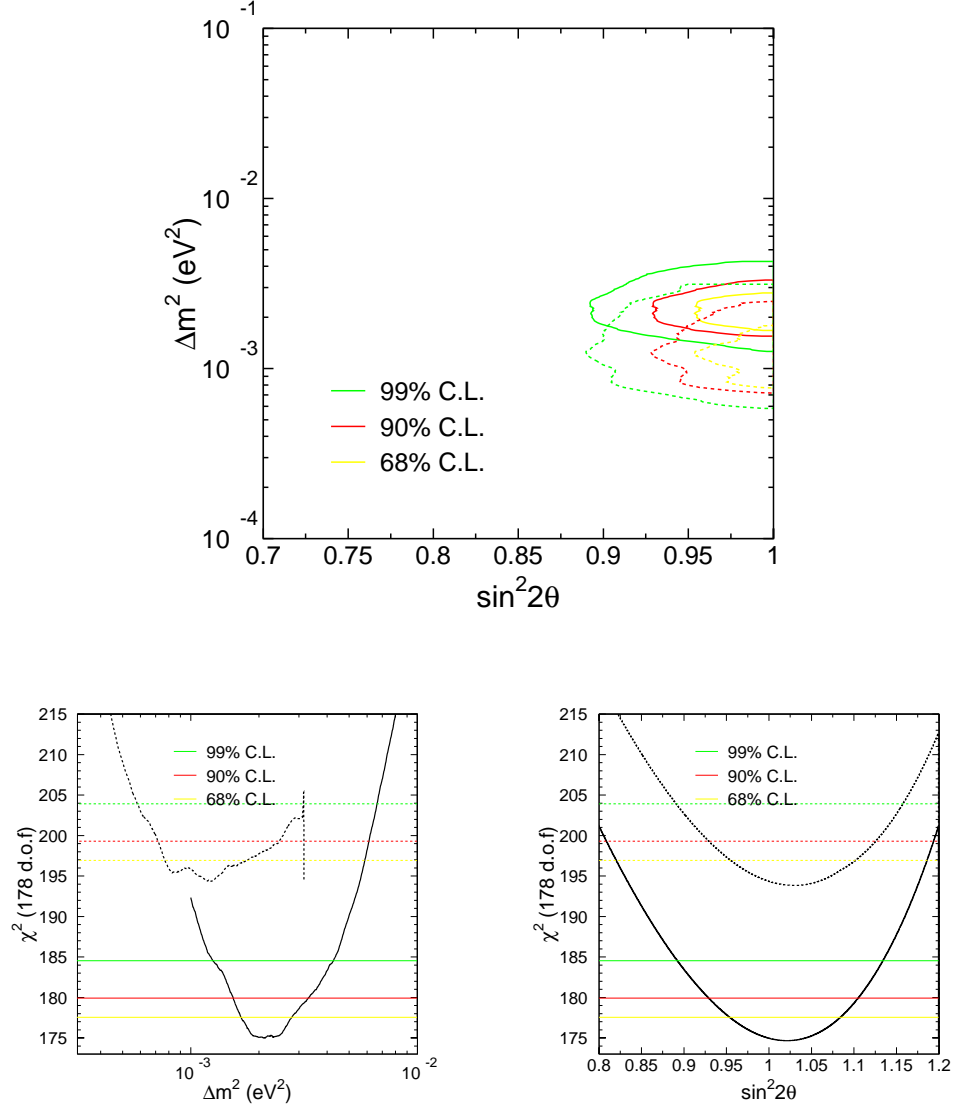
Figure 10.3: $\Delta m^2 \rightarrow \Delta m^2 \times \rho/\rho_o$ (without air pathlength). Contours of the best fit parameter for a rock only neutrino oscillation. The solid lines represent "standard" 2 flavor oscillations, and the dashed line are the simple MaVaN oscillations. The lower plots show the cross sections of the contour at the minimum point for each model. The higher dashed lines represent the MaVaN oscillations with $\chi^2_{min} = 194.357/178$ d.o.f. compared with the standard case of $\chi^2_{min} = 174.957/178$ d.o.f.

10.2.3   Unknown Density Dependence Assuming Maximal Mixing

A second analysis is done to find a best fit electron density dependence exponent in the case of matter-dependent oscillations assuming maximal mixing ($\sin^2(2\theta) = 1$) in all densities (except air). This analysis uses both Δm^2 and n as varied paramters. A Δm^2 domain of 10^-4 to 10^0 eV^2 is used over 81 bins, and considers density dependent powers from -3 to 3 over 61 bins. The results find a $\chi^2_{min} = 187.319/178$ d.o.f. (3.5 σ exclusion) for $(n, \Delta m^2) = (-0.30, 3.16 \times 10^{-3} eV^2)$. The contour is seen in Figure 10.4.

10.3   Analysis Including the air pathlength

The second analysis includes the air pathlength. In the case where there is no dependence ($n = 0$) on the electron density, this case reduces to the two flavor oscillations described in Chapter 8. The air mass density depends greatly on the altitude of the air above sea level. A graph of the mass density is seen in Figure 10.5. A conservative constant value of 10^{-3} g/cm^3 is used for the mass density, since atmospheric neutrinos are generated at roughly around 20 km altitude.

The constituents of dry air are:

- N_2: 75.52%, Z/A = 0.5

- O_2: 23.15%, Z/A = 0.5

- Ar: 1.28%, Z/A = 0.45

- CO_2: .05%, Z/A = 0.5 [23]

The value of Z/A is found by adding up the fractions multiplied by the Z/A, resulting in Z/A = 0.499. However, this does not include water vapor which also has Z/A = 0.5, so the mean Z/A value is approximated at 0.500, and the value of the electron charge density of air is 0.5×10^{-3} mol/cm^3.

10.3.1   Results of Various Density Dependence with Air Pathlength

The same models used in Section 10.2.2 are tested here to check various density dependent masses but with the air pathlength. The results are listed in Table 10.2. All models tested are excluded by $\geq 3.4\sigma$. The zenith angle and contour plots can be found in Appendix D.
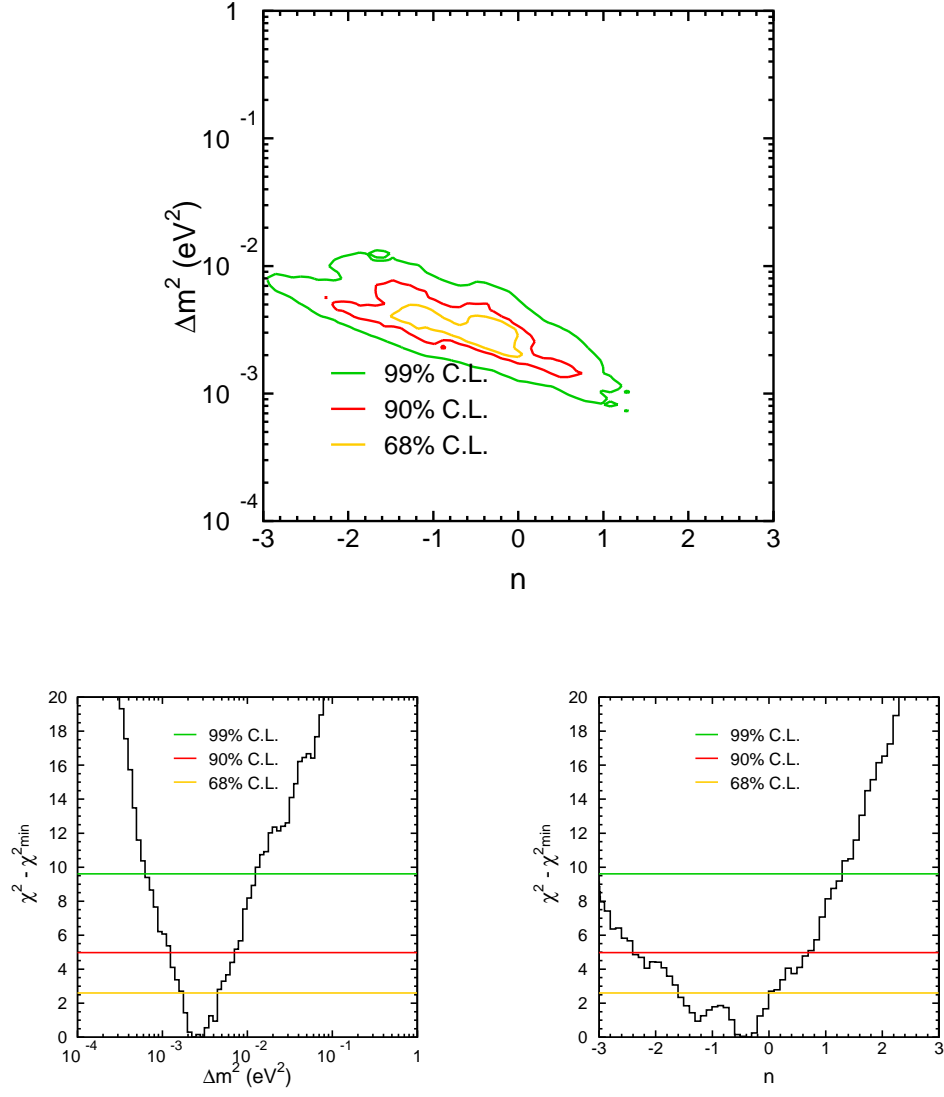
Figure 10.4: $\Delta m^2 \rightarrow \Delta m^2 \times (\rho/\rho_o)^n$ (without air pathlength). Contours of the varying e^--density dependence for a rock only neutrino oscillations. The lower plots show the cross sections of $\chi^2 - \chi^2_{min} = 187.319/178$ d.o.f. at $n = -0.30, \Delta m^2/(\rho_o)^n = 3.16 \times 10^{-3} eV^2$), respectively.
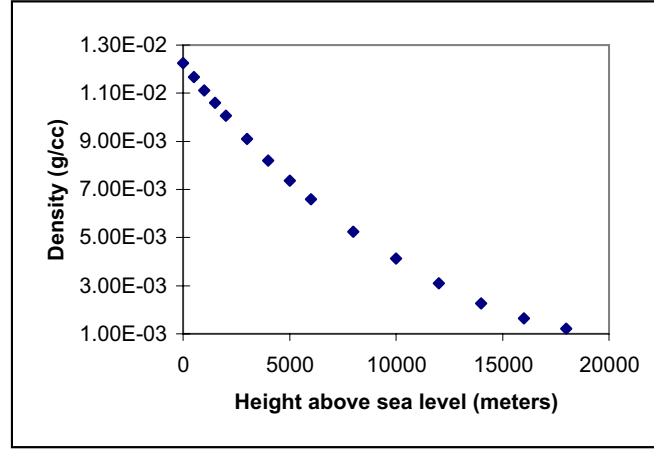
Figure 10.5: Average dry air density of the Standard Atmosphere as a function of altitude [23]

10.3.2   *Results Unknown Density Dependence Assuming Maximal Mixing with Air*

Another analysis is done which assumes maximal mixing and allows mass difference and density dependence n as floating parameters. The results are in figure 10.4. A minimum $\chi^2 = 173.167/178$ d.o.f. is found at $(n, \Delta m^2) = (-0.075, 2.00 \times 10^{-3} eV^2)$. Standard oscillations (n=0) is consistent with the minimum chi-squared within 1σ.
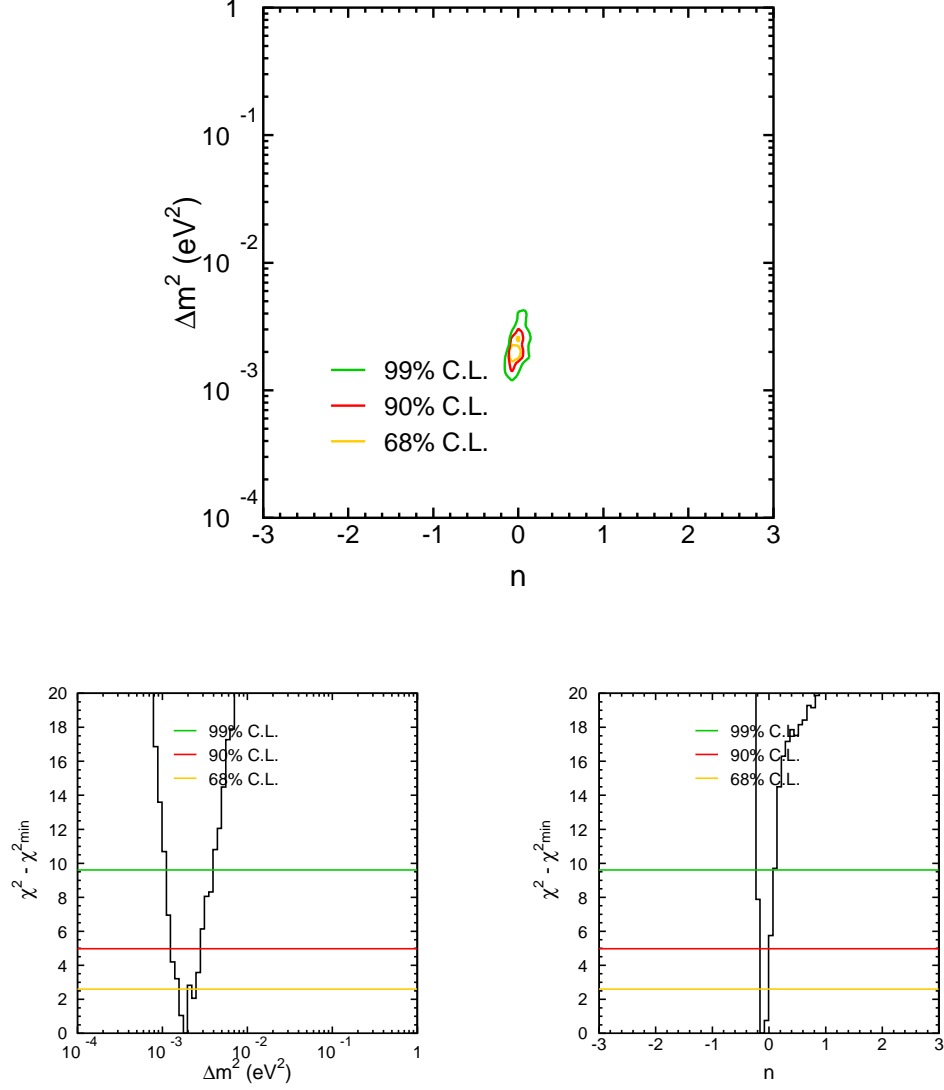
Figure 10.6: $\Delta m^2 \rightarrow \Delta m^2 \times \rho/\rho_o$ (with air pathlength). Contours of the varying e^--density dependence for a rock only neutrino oscillations. The lower plots show the cross sections of $\chi^2 - \chi^2_{min} = 173.167/178$ d.o.f. at $n = -0.075$, $\Delta m^2 = 2.00 \times 10^{-3} eV^2$), respectively. The case of no dependence (n=0) is within 1σ.

Table 10.2: Comparisons of χ^2 Values for Different Models with Air Path.

Model	Physical Region				Unphysical Region		
$\Delta m^2 \times (\rho/\rho_o)^n$	χ^2_{min}	Δm^2(eV^2)	$\sin^2(2\theta)$	$\Delta\sigma$	χ^2_{min}	Δm^2(eV^2)	$\sin^2(2\theta)$
Standard (n=0)	174.976	2.11×10^{-3}	1.00	-	174.611	2.11×10^{-3}	1.02
$n=2$	202.937	5.13×10^{-4}	1.00	5.3	202.622	5.13×10^{-4}	1.02
$n=1$	194.102	1.23×10^{-3}	1.00	4.3	193.538	1.19×10^{-3}	1.03
$n=\frac{2}{3}$	191.455	1.40×10^{-3}	1.00	4.1	190.715	1.40×10^{-3}	1.04
$n=\frac{1}{3}$	189.542	1.58×10^{-3}	1.00	3.8	188.311	1.58×10^{-3}	1.05
$n=-\frac{1}{3}$	229.867	7.16×10^{-4}	0.90	7.4	229.867	7.16×10^{-4}	0.90
$n=-\frac{2}{3}$	431.575	5.01×10^{-4}	0.57	16.0	431.575	5.01×10^{-4}	0.57
$n=-1$	447.477	4.47×10^{-2}	0.60	16.5	447.477	4.47×10^{-2}	0.60
$n=-2$	447.432	5.31×10^{-3}	0.60	16.5	447.432	5.31×10^{-3}	0.60

Chapter 11

CONCLUSIONS

The first phase of Super-Kamiokande ran from April 1996 until July 2001. During this period it detected 12,180 full-contained events and 911 partially-contained events in 1489 live-days. It also found 417.7 upward-going stopping muons and 1841.6 upward though-going muons in 1646 live-days. Due to its high statistics and event resolution, Super-Kamiokande was able to explain the small value of the muon to electron neutrino double ratio. It was caused by muon neutrino disappearance created by neutrino oscillations. Using a zenith angle chi-squared analysis with the pull method, Super-K found that a 2 flavor neutrino oscillation from muon flavor to tau flavor neutrinos could well fit the distribution of the muon neutrino data.

In this thesis, data from the Super-Kamiokande-I period is used to look at variant neutrino oscillation models to include a mass-varying effect dependent on the matter environment of the neutrino path by substituting Δm_{23}^2 with $\Delta m_{23}^2 \times \left(\frac{\rho_e}{\rho_o}\right)^n$ for different values of n. ($\rho_o = 1.0$ mol/cm^3.) The first model tested is that neutrinos only have an effective mass which oscillates only within dense matter. Such oscillations were revealed to be disfavored at a 3.8 σ level in comparison to a fixed mass with oscillations in all environments. The second set of models assumed a bias on a varying neutrino mass from the electron density of the material in a neutrino's path, a possible consequence of the MaVaN theory. Several different biases were tested, in two steps. The first step assumed only oscillations in matter, in the surrounding mountain and the Earth to Super-K. The second incorporated oscillations to also occur in air. In all cases tested, a mass difference with electron dependence is disfavored by at least a 3-σ level when compared with neutrino oscillations with a fixed mass. In addition, a floating density dependence analysis was performed assuming maximal mixing. It found a minimum chi-squared value of $\chi_{min}^2 = 173.167/178$ d.o.f. at ($n = -0.075$, $\Delta m^2 = 2.00 \times 10^{-3} eV^2$). The $n = 0$ (no density dependence) case lies within 1σ.

The results of this analysis show that the electron density does not significantly affect the neutrino masses. This does not exclude models where the mixing angle is not constant in all densities,

or which assume 3 flavor oscillations. Nor does it exclude all MaVaN models, which only predicts a neutrino mass dependence on neutrino density of the medium. One may conclude that neutrino oscillations must occur in air, however, future work is needed to determine if there exists any neutrino mass variance based on the medium.

BIBLIOGRAPHY

[1] M. Aglietta et al. Experimental study of atmospheric neutrino flux in the NUSEX experiment. *Europhys. Lett.*, 8:611–614, 1989.

[2] Vivek Agrawal, T. K. Gaisser, Paolo Lipari, and Todor Stanev. Atmospheric neutrino flux above 1 gev. *Phys. Rev.*, D53:1314–1323, 1996.

[3] B. Aharmim et al. Electron energy spectra, fluxes, and day-night asymmetries of B-8 solar neutrinos from the 391-day salt phase SNO data set. *Phys. Rev.*, C72:055502, 2005.

[4] M. H. Ahn. Measurement of neutrino oscillation by the K2K experiment. 2006.

[5] E. Kh. Akhmedov. Neutrino physics. 2000.

[6] Evgeny Akhmedov. Theory and phemomenology of neutrino oscillations. In *Neutrino 2006, Santa Fe, New Mexico*, 2006. Available from World Wide Web: `http://neutrinosantafe06.com/downloads/Session2/2.5Akhmedov.pdf`.

[7] M. Ambrosio et al. Low energy atmospheric muon neutrinos in MACRO. *Phys. Lett.*, B478:5–13, 2000.

[8] V. B. Anikeev et al. Total cross-section measurements for muon-neutrino, anti- muon-neutrino interactions in 3-gev - 30-gev energy range with IHEP-JINR neutrino detector. *Z. Phys.*, C70:39–46, 1996.

[9] M. Apollonio et al. Limits on neutrino oscillations from the CHOOZ experiment. *Phys. Lett.*, B466:415–430, 1999.

[10] M. Apollonio et al. Search for neutrino oscillations on a long base-line at the CHOOZ nuclear power station. *Eur. Phys. J.*, C27:331–374, 2003.

[11] T. Araki et al. Measurement of neutrino oscillation with KamLAND: Evidence of spectral distortion. *Phys. Rev. Lett.*, 94:081801, 2005.

[12] B. Armbruster et al. Upper limits for neutrino oscillations anti-nu/mu → anti- nu/e from muon decay at rest. *Phys. Rev.*, D65:112001, 2002.

[13] N. Armenise et al. Charged current elastic anti-neutrino interactions in propane. *Nucl. Phys.*, B152:365–375, 1979.

[14] Y. Ashie et al. Evidence for an oscillatory signature in atmospheric neutrino oscillation. *Phys. Rev. Lett.*, 93:101801, 2004.

[15] Y. Ashie et al. A measurement of atmospheric neutrino oscillation parameters by Super-Kamiokande I. *Phys. Rev.*, D71:112005, 2005.

[16] K. Assamagan et al. Upper limit of the muon-neutrino mass and charged pion mass from momentum analysis of a surface muon beam. *Phys. Rev.*, D53:6065–6077, 1996.

[17] C. Athanassopoulos et al. Evidence for nu/mu –¿ nu/e neutrino oscillations from LSND. *Phys. Rev. Lett.*, 81:1774–1777, 1998.

[18] Priscilla S. Auchincloss et al. Measurement of the inclusive charged current cross-section for neutrino and anti-neutrino scattering on isoscalar nucleons. *Z. Phys.*, C48:411–432, 1990.

[19] John N. Bahcall and P. I. Krastev. Does the sun appear brighter at night in neutrinos? *Phys. Rev.*, C56:2839–2857, 1997.

[20] N. J. Baker et al. Total cross-sections for muon-neutrino n and muon-neutrino p charged current interactions in the 7-ft bubble chamber. *Phys. Rev.*, D25:617–623, 1982.

[21] S. J. Barish et al. Study of neutrino interactions in hydrogen and deuterium. 1. description of the experiment and study of the reaction neutrino d → mu- p p(s). *Phys. Rev.*, D16:3103, 1977.

[22] G. D. Barr, T. K. Gaisser, P. Lipari, Simon Robbins, and T. Stanev. A three-dimensional calculation of atmospheric neutrinos. *Phys. Rev.*, D70:023006, 2004. Uses a slightly different flux from paper after private communication.

[23] G. K. Batchelor. *Introduction to Fluid Dynamics*. Cambridge University Press, 1967.

[24] G. Battistoni, A. Ferrari, T. Montaruli, and P. R. Sala. High energy extension of the FLUKA atmospheric neutrino flux. 2003.

[25] R. Becker-Szendy et al. The electron-neutrino and muon-neutrino content of the atmospheric flux. *Phys. Rev.*, D46:3720–3724, 1992.

[26] S. V. Belikov et al. Quasielastic neutrino and anti-neutrinos scattering: Total cross-sections, axial vector form-factor. *Z. Phys.*, A320:625, 1985.

[27] V. S. Berezinskii et al. *Astrophysics of Cosmic Rays*. North-Holland, 1990.

[28] J. P. Berge et al. Total neutrino and anti-neutrino charged current cross- section measurements in 100-gev, 160-gev and 200-gev narrow band beams. *Z. Phys.*, C35:443, 1987.

[29] Hans-Gerd Berns. Notes about the radon hut system [online]. Available from World Wide Web: `http://neutrino.phys.washington.edu/~berns/SUPERK/RADON/`.

[30] Hans-Gerd Berns. OD-DAQ description [online]. Available from World Wide Web: `http://neutrino.phys.washington.edu/~superk/hardware/`.

[31] Hans-Gerd Berns. Super-K OD DAQ - GPS subsystem [online]. Available from World Wide Web: `http://neutrino.phys.washington.edu/~berns/SUPERK/GPS/`.

[32] D. J. Bird et al. Detection of a cosmic ray with measured energy well beyond the expected spectral cutoff due to cosmic microwave radiation. *Ap. J.*, 441:144, 1995.

[33] S. Bonetti et al. Study of quasielastic reactions of neutrino and anti- neutrino in Gargamelle. *Nuovo Cim.*, A38:260–270, 1977.

[34] D. Casper. The NUANCE neutrino physics simulation, and the future. *Nucl. Phys. Proc. Suppl.*, 112:161–170, 2002.

[35] D. Casper et al. Measurement of atmospheric neutrino composition with IMB- 3. *Phys. Rev. Lett.*, 66:2561–2564, 1991.

[36] S. Ciampolillo et al. Total cross-section for neutrino charged current interactions at 3-gev and 9-gev. *Phys. Lett.*, B84:281, 1979.

[37] R. Clark et al. Atmospheric muon-neutrino fraction above 1-gev. *Phys. Rev. Lett.*, 79:345–348, 1997.

[38] C. L. Cowan, F. Reines, F. B. Harrison, H. W. Kruse, and A. D. McGuire. Detection of the free neutrino: A confirmation. *Science*, 124:103–104, 1956.

[39] K. Daum et al. Determination of the atmospheric neutrino spectra with the Frejus detector. *Z. Phys.*, C66:417–428, 1995.

[40] Y. Declais et al. Search for neutrino oscillations at 15-meters, 40-meters, and 95-meters from a nuclear power reactor at Bugey. *Nucl. Phys.*, B434:503–534, 1995.

[41] Shantanu Desai. *High energy neutrino astrophysics with Super-Kamiokande*. PhD thesis, Boston University, January 2004. Available from World Wide Web: `http://www-sk.icrr.u-tokyo.ac.jp/sk/pub/desai.ps.gz`.

[42] A. M. Dziewonski and D. L. Anderson. Preliminary reference Earth model. *Phys. Earth Planet. Interiors*, 25:297–356, 1981.

[43] Rob Fardon, Ann E. Nelson, and Neal Weiner. Dark energy from Mass Varying Neutrinos. *J. Cosmol. Astropart. Phys.*, 10:005, 2004.

[44] G. L. Fogli, E. Lisi, A. Marrone, D. Montanino, and A. Palazzo. Getting the most from the statistical analysis of solar neutrino oscillations. *Phys. Rev.*, D66:053010, 2002.

[45] G. William Foster. Crude calculation of pressure spike from underwater photomultiplier implosion [online]. Available from World Wide Web: `http://tdserver1.fnal.gov/foster/BooNE_Photomultiplier_Implosion.pdf`.

[46] W. Frati, T. K. Gaisser, A. K. Mann, and Todor Stanev. Atmospheric neutrino data and neutrino oscillations. *Phys. Rev.*, D48:1140–1149, 1993.

[47] S. Fukuda et al. Tau neutrinos favored over sterile neutrinos in atmospheric muon neutrino oscillations. *Phys. Rev. Lett.*, 85:3999–4003, 2000.

[48] Y. Fukuda et al. Atmospheric muon-neutrino / electron-neutrino ratio in the multigev energy range. *Phys. Lett.*, B335:237–245, 1994.

[49] Y. Fukuda et al. The Super-Kamiokande detector. *Nucl. Instrum. Meth.*, A501:418–462, 2003.

[50] Murray Gell-Mann and A. Pais. Behavior of neutral particles under charge conjugation. *Phys. Rev.*, 97:1387–1389, 1955.

[51] M. Gluck, E. Reya, and A. Vogt. Dynamical parton distributions of the proton and small x physics. *Z. Phys.*, C67:433–448, 1995.

[52] Kenneth Greisen. End to the cosmic ray spectrum? *Phys. Rev. Lett.*, 16:748–750, 1966.

[53] Space Physics Data System Group. Space physics data system: Climax and Haleakala neutron monitor datasets [online]. Available from World Wide Web: `http://ulysses.sr.unh.edu/NeutronMonitor/`.

[54] N. Hayashida et al. Updated AGASA event list above 4*10**19-ev. *Astron. J.*, 120:2190, 2000.

[55] Y. Hayato. NEUT. *Nucl. Phys. Proc. Suppl.*, 112:171–176, 2002.

[56] K. S. Hirata et al. Experimental study of the atmospheric neutrino flux. *Phys. Lett.*, B205:416, 1988.

[57] K. S. Hirata et al. Observation of a small atmospheric ν_μ/ν_e ratio in Kamiokande. *Phys. Lett.*, B280:146–152, 1992.

[58] M. Honda, T. Kajita, K. Kasahara, and S. Midorikawa. Calculation of the flux of atmospheric neutrinos. *Phys. Rev.*, D52:4985–5005, 1995.

[59] M. Honda, T. Kajita, K. Kasahara, and S. Midorikawa. Comparison of 3-dimensional and 1-dimensional schemes in the calculation of atmospheric neutrinos. *Phys. Rev.*, D64:053011, 2001.

[60] M. Honda, K. Kasahara, K. Hidaka, and S. Midorikawa. Atmospheric neutrino fluxes. *Phys. Lett.*, B248:193–198, 1990.

[61] Morihiro Honda, T. Kajita, K. Kasahara, and S. Midorikawa. A new calculation of the atmospheric neutrino flux in a 3- dimensional scheme. *Phys. Rev.*, D70:043008, 2004.

[62] J. Hosaka et al. Solar neutrino measurements in Super-Kamiokande-I. *Phys. Rev.*, D73:112001, 2006.

[63] J. Hosaka et al. Three flavor neutrino oscillation analysis of atmospheric neutrinos in Super-Kamiokande. *Phys. Rev.*, D74:032002, 2006.

[64] Masaki Ishitsuka. *L/E analysis of the atmospheric neutrino data from Super-Kamiokande*. PhD thesis, University of Tokyo, February 2004. Available from World Wide Web: `http://www-sk.icrr.u-tokyo.ac.jp/sk/pub/ishitsuka_thesis.ps.gz`.

[65] David B. Kaplan, Ann E. Nelson, and Neal Weiner. Neutrino oscillations as a probe of dark energy. *Phys. Rev. Lett.*, 93:091801, 2004.

[66] T. Kitagaki et al. Charged current exclusive pion production in neutrino deuterium interactions. *Phys. Rev.*, D34:2554–2565, 1986.

[67] Yusuke Koshio. *Study of Solar Neutrinos at Super-Kamiokande*. PhD thesis, University of Tokyo, 1998. Available from World Wide Web: `http://www-sk.icrr.u-tokyo.ac.jp/sk/pub/d.ps.gz`.

[68] P. Lipari and T. Stanev. Propagation of multi - tev muons. *Phys. Rev.*, D44:3543–3554, 1991.

[69] C. H. Llewellyn Smith. Neutrino reactions at accelerator energies. *Phys. Rept.*, 3:261, 1972.

[70] Louis Lyons. Selecting between two hypotheses. OUNP-99-12.

[71] D. MacFarlane et al. Nucleon structure functions from high-energy neutrino interactions with iron and QCD results. *Z. Phys.*, C26:1, 1984.

[72] Z. Maki, M. Nakagawa, and S. Sakata. Remarks on the unified model of elementary particles. *Prog. Theor. Phys.*, 28:870, 1962.

[73] Mark Messier. *Evidence for Neutrino Mass from Observations of Atmospheric Neutrinos with Super-Kamiokande*. PhD thesis, Boston University, 1999. Available from World Wide Web: `http://www-sk.icrr.u-tokyo.ac.jp/sk/pub/messier_thesis.ps.gz`.

[74] S. P. Mikheev and A. Yu. Smirnov. Resonance enhancement of oscillations in matter and solar neutrino spectroscopy. *Sov. J. Nucl. Phys.*, 42:913–917, 1985.

[75] Ann E. Nelson and Neal Weiner. Private communications.

[76] Kazunori Nitta. *Neutrino Oscillation Analysis of Upward Through-going and Stopping Muons in Super-Kamiokande*. PhD thesis, Osaka University, February 2002. Available from World Wide Web: `http://www-sk.icrr.u-tokyo.ac.jp/sk/pub/nitta.ps.gz`.

[77] Michael R. Nolta et al. First year Wilkinson Microwave Anisotropy Probe (WMAP) observations: Dark energy induced correlation with radio sources. *Astrophys. J.*, 608:10–15, 2004.

[78] B. Pontecorvo. Mesonium and antimesonium. *Sov. Phys. JETP*, 6:429, 1957.

[79] B. Pontecorvo. Inverse beta processes and nonconservation of lepton charge. *Sov. Phys. JETP*, 7:172–173, 1958.

[80] G. M. Radecky et al. Study of single pion production by weak charged currents in low-energy neutrino d interactions. *Phys. Rev.*, D25:1161–1173, 1982.

[81] D. Rein. Angular distribution in neutrino induced single pion production processes. *Z. Phys.*, C35:43–64, 1987.

[82] Dieter Rein and Lalit M. Sehgal. Neutrino excitation of baryon resonances and single pion production. *Ann. Phys.*, 133:79, 1981.

[83] Dieter Rein and Lalit M. Sehgal. Coherent pi0 production in neutrino reactions. *Nucl. Phys.*, B223:29, 1983.

[84] J. M. Roney. Review of the tau neutrino mass. *Nucl. Phys. Proc. Suppl.*, 91:287–292, 2001.

[85] Mayly C. Sanchez et al. Observation of atmospheric neutrino oscillations in Soudan 2. *Phys. Rev.*, D68:113004, 2003.

[86] F. A. Scott. Energy spectrum of the beta-rays of radium E. *Phys. Rev.*, 48(5):391–395, Sep 1935.

[87] Uros Seljak et al. Cosmological parameter analysis including SDSS Ly-alpha forest and galaxy bias: Constraints on the primordial spectrum of fluctuations, neutrino mass, and dark energy. *Phys. Rev.*, D71:103515, 2005.

[88] Y. Shikaze et al. Solar modulation effect on the cosmic-ray proton spectra measured by BESS. Prepared for 28th International Cosmic Ray Conferences (ICRC 2003), Tsukuba, Japan, 31 Jul - 7 Aug 2003.

[89] G. Sigl. Ultrahigh energy neutrinos and cosmic rays as probes of new physics. 2001.

[90] Torbjorn Sjostrand. High-energy physics event generation with PYTHIA 5.7 and JETSET 7.4. *Comput. Phys. Commun.*, 82:74–90, 1994.

[91] R. A. Smith and E. J. Moniz. Neutrino reactions on nuclear targets. *Nucl. Phys.*, B43:605, 1972.

[92] Andrew Stachyra. *A Search for Astrophysical Point Sources of Neutrinos with Super-Kamiokande*. PhD thesis, University of Washington, February 2002. Available from World Wide Web: `http://www-sk.icrr.u-tokyo.ac.jp/sk/pub/stachyra-thesis.ps.gz`.

[93] L. V. Volkova. Energy spectra and angular distributions of atmospheric neutrinos. *Sov. J. Nucl. Phys.*, 31:784–790, 1980.

[94] A. S. Vovenko et al. Energy dependence of total cross-sections for neutrino and anti-neutrino interactions at energies below 35-gev. *Sov. J. Nucl. Phys.*, 30:528, 1979.

[95] Neal Weiner. Neutrinos and dark energy. In *Neutrino 2006, Santa Fe, New Mexico*, 2006.

[96] C. Weinheimer et al. High precision measurement of the tritium beta spectrum near its endpoint and upper limit on the neutrino mass. *Phys. Lett.*, B460:219–226, 1999.

[97] L. Wolfenstein. Neutrino oscillations in matter. *Phys. Rev.*, D17:2369, 1978.

[98] S. Yoshida et al. Search for spin coupled WIMPs with the large volume NaI(Tl) scintillators. Prepared for 14th International Spin Physics Symposium (SPIN 2000), Osaka, Japan, 16-21 Oct 2000.

[99] G. T. Zatsepin and V. A. Kuzmin. Upper limit of the spectrum of cosmic rays. *JETP Lett.*, 4:78–80, 1966.

[100] Kathryn M. Zurek. New matter effects in neutrino oscillation experiments. *JHEP*, 10:058, 2004.

Appendix A

SUPER-KAMIOKANDE II AND SUPER-KAMIOKANDE III

A.1   Super-Kamiokande Accident

In the summer of 2001, Super-Kamiokande temporarily shut itself down for maintenance after running continuously for five years. As the tank was slowly drained, crews on rafts replaced bad photomultiplier tubes as well as some deteriorated wall structure. After the repairs had been completed, Super-Kamiokande began to be refilled. During this refilling on November 12th, when the tank was about 3/4 full of water, an inner detector photomultiplier tube near the bottom of the inner detector imploded. Because the ID tubes are so large and hold a vacuum, it is believed the implosion sent a shockwave through the water, which caused the PMT next to it to also implode. A chain reaction began which eventually destroyed about 60% of the PMTs. (A summary of the PMT damage is in Table A.1.) Most of these tubes were more than 5 meters below the water surface. The sound of the implosions could be heard for about 5-10 seconds and had shown up on a nearby earthquake detector. The total energy released had been estimated by G. W. Foster [45] to be around 170 MegaJoules, or about 510 sticks of dynamite.

A.1.1   Super-Kamiokande Damage

Table A.1: Number of Dead and Installed PMTs.

	Dead	Installed
Bottom	1,748	1,748
Side	4,917	7,650
Top	0	1,748
Total	6,665	11,146

Summaries of the inner and outer detector damage are in Tables A.2 and A.3.

Table A.2: Summary of the damage in the Inner Detector.

	Status
Dead PMTs	6,777 (out of 11,146 50cm PMTs)
Live PMTs	4,369
Electronics	No damage
HV supplies	No damage
Cables	Unknown
PMT support parts	Many damaged
Black plastic sheets	All to be replaced (for light shield)
Tank outer wall	Some leak (4.2 tons/hour)

A.1.2   Cause and Effect

Fortunately, the detector was running during the filling as a supernova detector. The implosion and resulting light caused many events recorded into data stream. A thorough scan of the event displays leading up to and just after the initial implosion deduced the location of the faulty PMT to two possible candidates along the bottom wall. One of these was an original tube installed back in 1995 during the Super-Kamiokande construction; the other was a replacement tube installed that summer during the refurbishing. An investigative committee determined the cause to be one of two scenarios:

- During the summer upgrade, while working on the bottom wall, foam blocks were put on top of the older PMTs to allow people to work upon. There had been some extensive tests prior to the accident to insure the integrity of the PMT. However, an accumulation of stress may have led to a weakening which led to an implosion.

- A new PMT may have been somehow damaged in the transportation or installation process due to mishandling. This could have led to a small crack in the base of the PMT.

Table A.3: Summary of the damage in the Outer Detector.

	Status
Dead PMTs	1,110 (out of 1,885 20cm PMTs)
Live PMTs	785
Electronics	No damage
HV supplies	Slight damage
Wavelength shifters	700 damaged (out of 1,885)
Tyvek sheets	All to be replaced (for light reflection)
Cables	Unknown
PMT support parts	Many damaged

To prevent future occurences, a prophylactic cover was designed to fit over the ID PMT. A acrylic sheath with holes was made to protect the sides of the tube and a clear acrylic dome was put over the main light collection area of the photocathode. In case of an implosion, the holes limit rapid water movement into the PMT volume. Tests have shown that this cover absorbs the implosion shockwave and should prevent any future accidents of this type.

A.2 Super-Kamiokande II

However, this did not solve the problem that 6000+ custom made $3000 photomultiplier tubes were needed to completely repair Super-Kamiokande to its state before the accident. In the following summer of 2002, Super-Kamiokande was again drained of it water and cleaned out. A few more custom ID PMTs were manufactured in the months that had passed since the accident, and they plus any surviving tubes were redistributed uniformly throughout the detector. The OD PMTs and wavelength shifter plates were all replaced due to the availability of these supplies. By the end of summer 2002 the repair work had been completed and Super-Kamiokande was ready to take data, but with only 5183 inner detector PMTs, or about 47% of original tubes. This meant only a 20% photocathode coverage, which was adequate for most aspects of the experiment, including the atmospheric neutrino analysis.

In addition to the detector itself getting an overhall, the radon hut also received an upgrade. The outside air blower was changed in 2002 with the removal of the carbon tanks and replacement of the dehumidifier. A new large blower was also installed which increased air movement to about 50 m^3/min to improve overall air quality and account for new experimental areas surrounding the tank. This data taking period after the summer of 2002 is referred to Super-Kamiokande II, or SK-II. SK-II lasted until mid-2005, where once more the experiment was temporarily stopped and drained so that the remaining 5963 tubes that have been manufactured since 2002 could be put into place.

A.3   Super-Kamiokande III

After the accident, the intention was always to return Super-K to its original photomultiplier capacity. By 2006 enough replacement PMTs had been manufactured and the detector was shut down in order to install the tubes. In addition to the remaining 5963 missing ID PMTs, 105 OD PMTs were also replaced, and 18 possible leaks in the tank were repaired. In September of 2005 the tank was opened and the upgrade began. Water filling started on April 18th, 2006, and finished on July 11 of that year. This data taking period after being returned to full capacity is referred to as SK-III. This is nearly identical to the SK-I setup with major addition of the PMT acrylic covers.

Appendix B

3-FLAVOR NEUTRINO OSCILLATIONS IN VACUUM

Expanding Equation 7.2 to include 3-flavor oscillations yields:

$$
\begin{pmatrix} \nu_e \\ \nu_\mu \\ \nu_\tau \end{pmatrix} = \begin{pmatrix} U_{e1} & U_{e2} & U_{e3} \\ U_{\mu 1} & U_{\mu 2} & U_{\mu 3} \\ U_{\tau 1} & U_{\tau 2} & U_{\tau 3} \end{pmatrix} \begin{pmatrix} \nu_1 \\ \nu_2 \\ \nu_3 \end{pmatrix}
\tag{B.1}
$$

It is assumed here than there is no sterile neutrino, though a 4x4 matrix may be used to include one. The MNS matrix is commonly parametrized in the form:

$$
U = \begin{pmatrix} c_{12}c_{13} & s_{12}c_{13} & s_{13}e^{-i\delta} \\ -s_{12}c_{23} - c_{12}s_{23}s_{13}e^{i\delta} & c_{12}c_{23} - s_{12}s_{23}s_{13}e^{i\delta_{CP}} & s_{23}c_{13} \\ s_{12}s_{23} - c_{12}c_{23}s_{13}e^{i\delta} & -c_{12}s_{23} - s_{12}c_{23}s_{13}e^{i\delta_{CP}} & c_{23}c_{13} \end{pmatrix} \times \begin{pmatrix} e^{i\sigma_1/2} & & \\ & e^{i\sigma_2/2} & \\ & & 1 \end{pmatrix}
\tag{B.2}
$$

where $c_{ij} = \cos\theta_{ij}$ and $s_{ij} = \sin\theta_{ij}$. Notice that if all mixing angles were zero then the MNS matrix would reduce to the identity meaning the mass eigenstates would be the same as the flavor eigenstates. δ_{CP} is a possible Dirac-type CP-violating phase, and $\sigma_1, 2$ are Majorana type CP violating phases [1]. The MNS matrix can be broken up into three matrices:

$$
U = \begin{pmatrix} c_{12} & s_{12} & \\ -s_{12} & c_{12} & \\ & & 1 \end{pmatrix} \underbrace{\begin{pmatrix} c_{13} & & s_{13}e^{-i\delta} \\ & 1 & \\ -s_{13}e^{i\delta} & & c_{13} \end{pmatrix}}_{\text{solar}} \underbrace{\begin{pmatrix} 1 & & \\ & c_{23} & s_{23} \\ & -s_{23} & c_{23} \end{pmatrix}}_{\text{atmospheric}}
\tag{B.3}
$$

which looks like three distinct 2-flavor oscillations, which include both the atmospheric neutrino oscillations and the solar neutrino oscillations.

---

[1] In the case of Dirac neutrino, the phases are zero.

B.1   Current Results Pertaining to 3-Flavor Oscillations

Current experiments such as Super-K, K2K, KamLAND, and SNO have concluded that both the solar mixing angle [62, 3, 11] and the atmospheric neutrino mixing angle [15, 4] are large (about 30 $^{\circ}$ 45°, respectively,) which implies significant mixing between the flavor and mass eigenstates. The best limits from the CHOOZ [10] experiment finds that the last mixing angle θ_{13} is small ($\sin^2(2\theta)<$ 0.2). In addition, KamLAND results have found the mass difference $\Delta m_{21}^2 = \Delta m_{solar}^2 = 8.0 \times 10^{-5}$eV, which is much smaller than Super-K's result of $\Delta m_{31}^2 = \Delta m_{atmos}^2 = 2.1 \times 10^{-3}$eV. This means that the solar and atmospheric neutrino oscillations can be treated as two independent 2-flavor oscillations to a first order approximation.

Appendix C

MAVANS

C.1   Dark Energy

Measurement of the cosmic microwave background by WMAP have found that the universe is very close to being flat [77]. The concept of "dark energy" was created to be the unknown unobserved energy that must exist to bring mass/energy density of the universe to within the measured critical density required for the shape of the universe to be flat. It acts as a "negative gravity" which permeates all space.

One possible solution of the energy is what Einstein called "quintessence", a dynamic field whose energy density varies both in space and time. If this is the case, then the predicted mass density of such a constant ($\Lambda^4 = 7 \times 10^{-30}g/cm^3 \approx (10^{-2.5}eV)^4$)would be near the neutrino mass separation scales ($\Delta m_{23}^2 = 10^{-2.5}$eV), making neutrinos a possible source of dark energy. Relic neutrinos from the big bang also form a smooth background, similar to that of dark energy.

C.2   Mass Varying Neutrino Model (MaVaN) (from [43])

In the Standard Model of particle physics, the Lagrangian for a lepton looks like:

$$\mathcal{L}_{mass} = m\overline{\psi}\psi \tag{C.1}$$

where the lepton field ψ is made up of left and right handed chirality components. For e$^-$, μ, and τ neutrinos, these active flavor fields are only left handed.

Dark energy does not exist within the Standard Model. Suppose there exists outside of the Standard Model: "A", a dark scalar field and functions as an acceleron, and a sterile (right-handed chirality) neutrino "n". The dark scalar field only couples to the sterile neutrinos, while the sterile neutrinos can also couple to the active flavor neutrinos. Since active neutrinos ν are left-handed chirality and the sterile neutrino n is right handed, $\psi = \psi_{LH} + \psi_{RH} = (\nu + \bar{n}) + (\bar{\nu} + n)$. The mass term of the

Lagrangian is:

$$\mathcal{L}_{mass} = m(\overline{\psi_{LH} + \psi_{RH}})(\psi_{LH} + \psi_{RH}) \tag{C.2}$$

$$= m(\overline{\psi_{LH}}\psi_{RH} + \overline{\psi_{RH}}\psi_{LH}) \tag{C.3}$$

$$= m_{Dirac}\nu\bar{n} + m_{2,Majorana}nn + m_{1,Majorana}\nu\nu + h.c. \tag{C.4}$$

The MaVaN model assumes $m_{1,Majorana}$ and $m_{2,Majorana}$ to be zero. The new dark scalar field and sterile neutrino also couple together and add another term to the Lagrangian:

$$\mathcal{L}_{MaVaN} = \langle A \rangle nn \tag{C.5}$$

where $\langle A \rangle$ is the vacuum expectation value (vev) of the dark scalar A. The total Lagrangian is written in short form as:

$$\mathcal{L}_{mass+MaVaN} = \begin{pmatrix} & m_{Dirac} \\ m_{Dirac} & \langle A \rangle \end{pmatrix} \begin{pmatrix} \nu \\ n \end{pmatrix} \tag{C.6}$$

Reduction of the matrix yields the eigenvalues:

$$\lambda_{\pm} = \frac{\langle A \rangle \pm \sqrt{\langle A \rangle^2 + 4m_{Dirac}^2}}{2} \approx \left(\langle A \rangle, -\frac{m_{Dirac}^2}{\langle A \rangle} \right) \tag{C.7}$$

in the case that $\langle A \rangle \gg m_{Dirac}$. With these eigenvalues the eigenvectors are now:

$$v_{\lambda=\langle A \rangle} = \frac{m_{Dirac}}{\langle A \rangle}\nu + n \tag{C.8}$$

$$v_{\lambda=-\frac{m_{Dirac}^2}{\langle A \rangle}} = \nu - \frac{m_{Dirac}}{\langle A \rangle}n \tag{C.9}$$

The first eigenstate has a mass of $\langle A \rangle$ and is primarily the right handed sterile neutrino. The second eigenstate has a mass of $\frac{m_{Dirac}^2}{\langle A \rangle}$, and is mostly made up of the active flavor neutrinos. Since $\langle A \rangle \gg m_{Dirac}^2$, this means that these have very light neutrino masses. This is the same idea as the seesaw mechanism often used to explain the radically light mass of neutrinos compared with other particles.

C.3 How the MaVaN model makes a mass-varying neutrino

According to Equation C.9 the flavor neutrino mass is inversely proportional to $\langle A \rangle$. The neutrino and acceleron's contribution to the dark energy would be:

$$\text{Total Energy} = n_\nu \times \frac{m_{Dirac}^2}{\langle A \rangle} + V(A)$$

n_ν being the number of neutrinos in the universe. However, the vacuum expectation value of A is dynamic. The neutrino background creates an effective potential preventing the active neutrino mass from getting too large and leaving the negative pressure on the universe (see Fig. C.1). Generically, this says that as the universe continues to expand, the density of neutrinos decreases, pushing A to larger values and the active neutrinos masses decrease. Conversely, in areas of high neutrino density (e.g. a supernova) there could also be a significant increasing effect on the neutrino masses. The minima of the energy corresponds to m_ν, the mass of the flavor neutrinos in vacuum.

However, arguments made in [65] claim that the existence of MaVaNs can lead to possible ad-
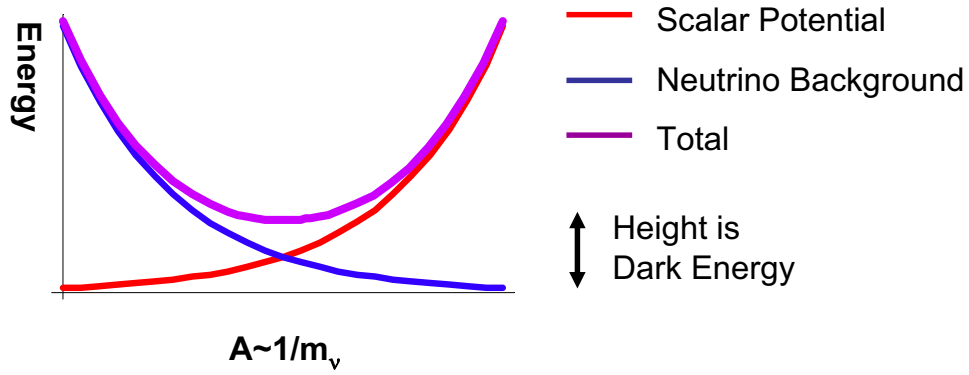
Figure C.1: MaVaN Potential, from [95]

ditional matter effects on the neutrino mass due to radiative couplings. These matter effects can come from Yukawa couplings with proton, neutrons, and electrons in the neutrino's pathlength. Zurek [100] considers such a possibility to account for the results of various neutrino experiments, including LSND.

Appendix D

OTHER PLOTS OF MAVAN MODELS

All models tested have zenith angle bin figures and contour plots.

- For the zenith angle bins figures, red boxed areas are the non-oscillated MC prediction, solid green lines are "standard" oscillations (as described in Chapter 8), blue dashed lines are MaVaN oscillations, and black crosshairs are data.

- In the contour plots, the upper plot overlays the best-fit contours for MaVaN and "standard" oscillations in dotted and solid lines, respectively. The lower plots show cross sections of the upper graph along each models χ^2_{min} axes. The upper dashed line are MaVaN oscillations and the lower lines are "standard" oscillations. The "standard" case has $\chi^2_{min} = 174.975/178$ d.o.f.
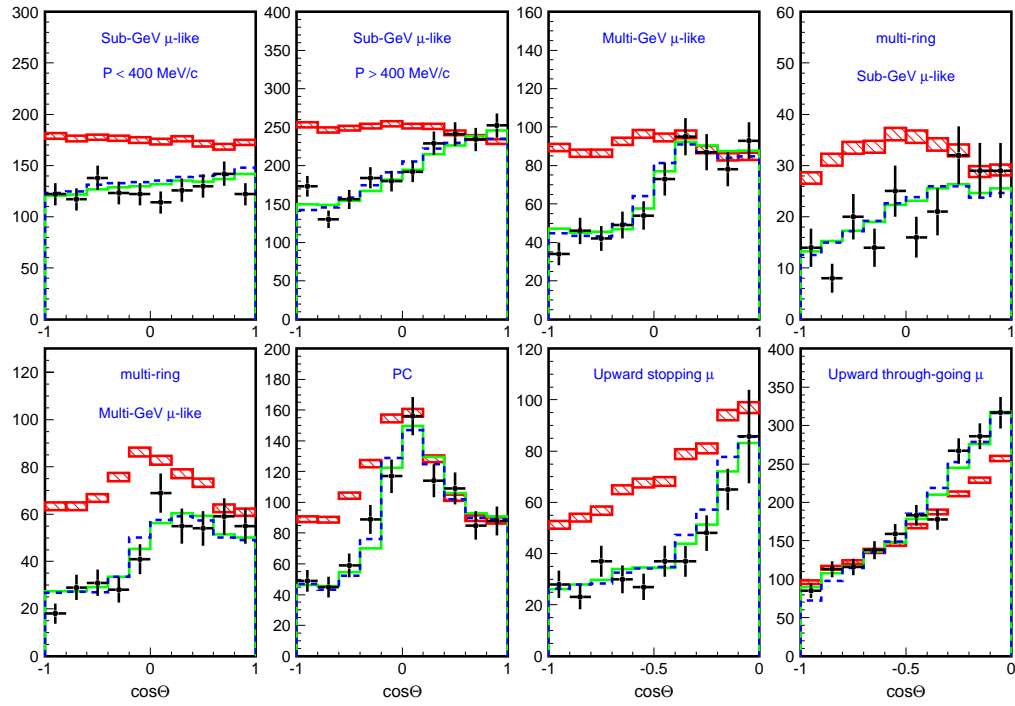
Figure D.1: Zenith angle bins for $\Delta m^2 \rightarrow \Delta m^2 \times \left(\frac{\rho}{\rho_o}\right)^2$ (no air pathlength).
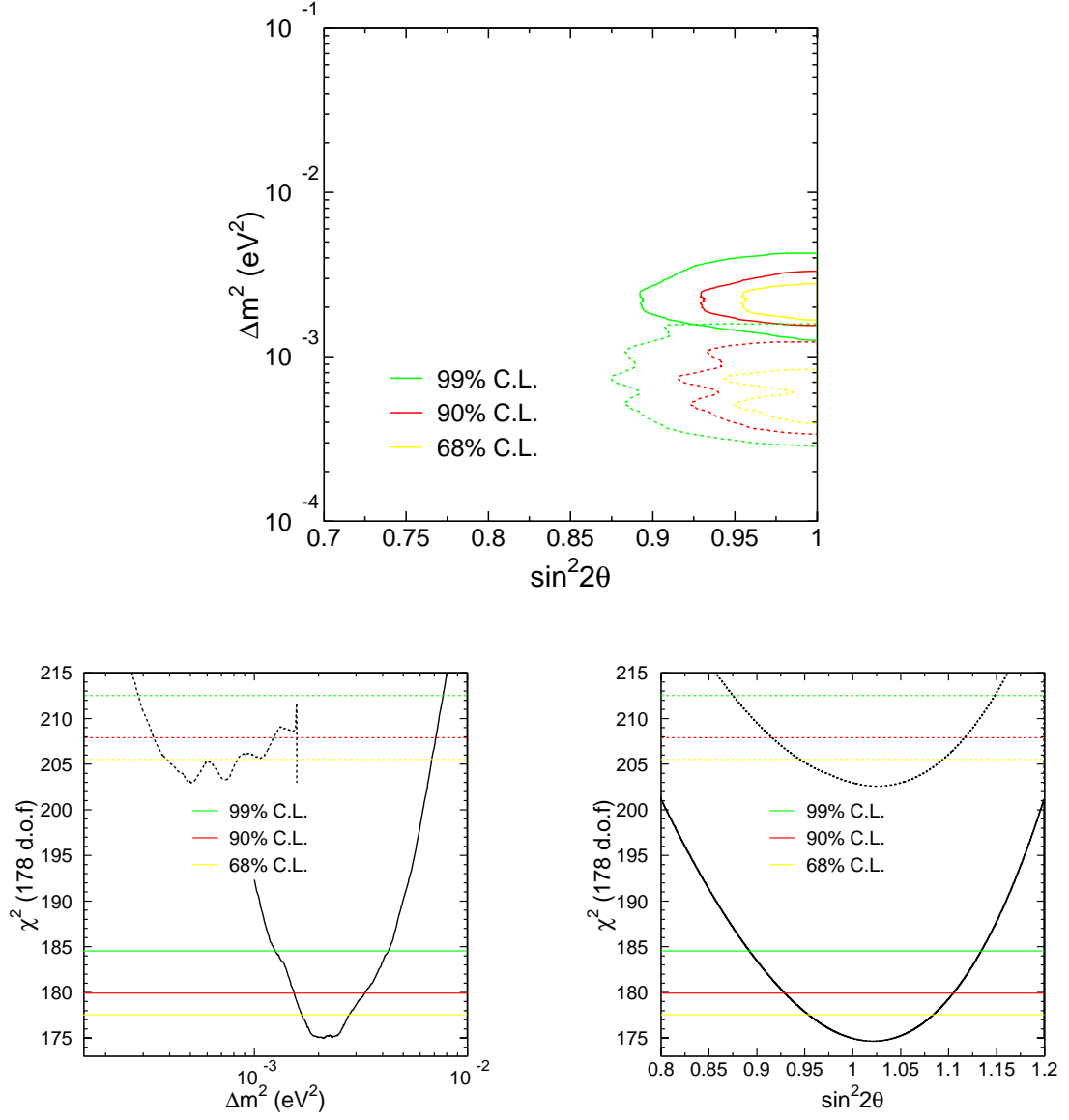
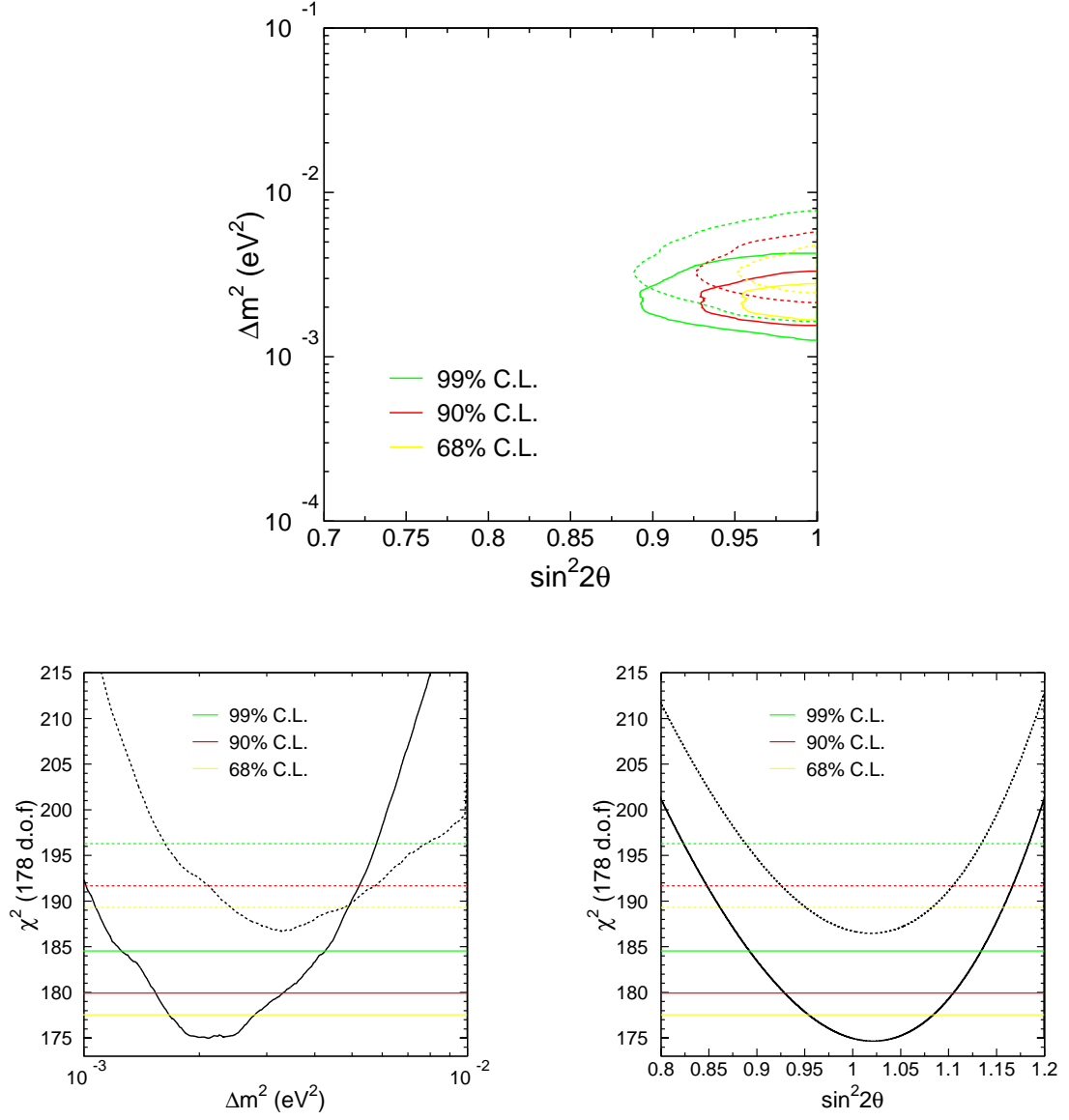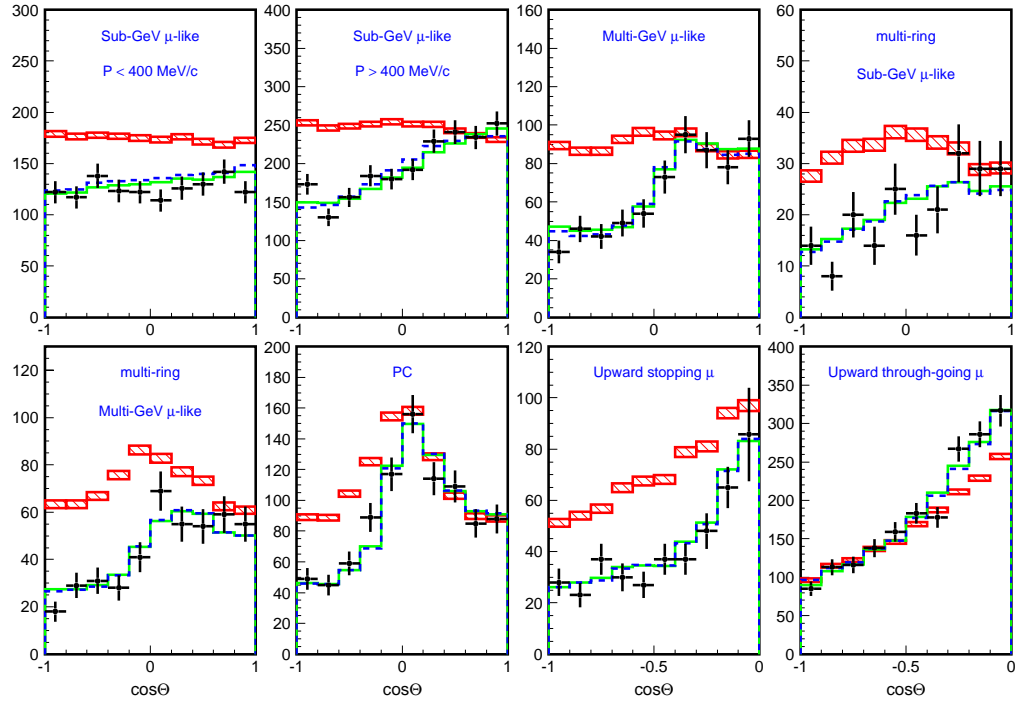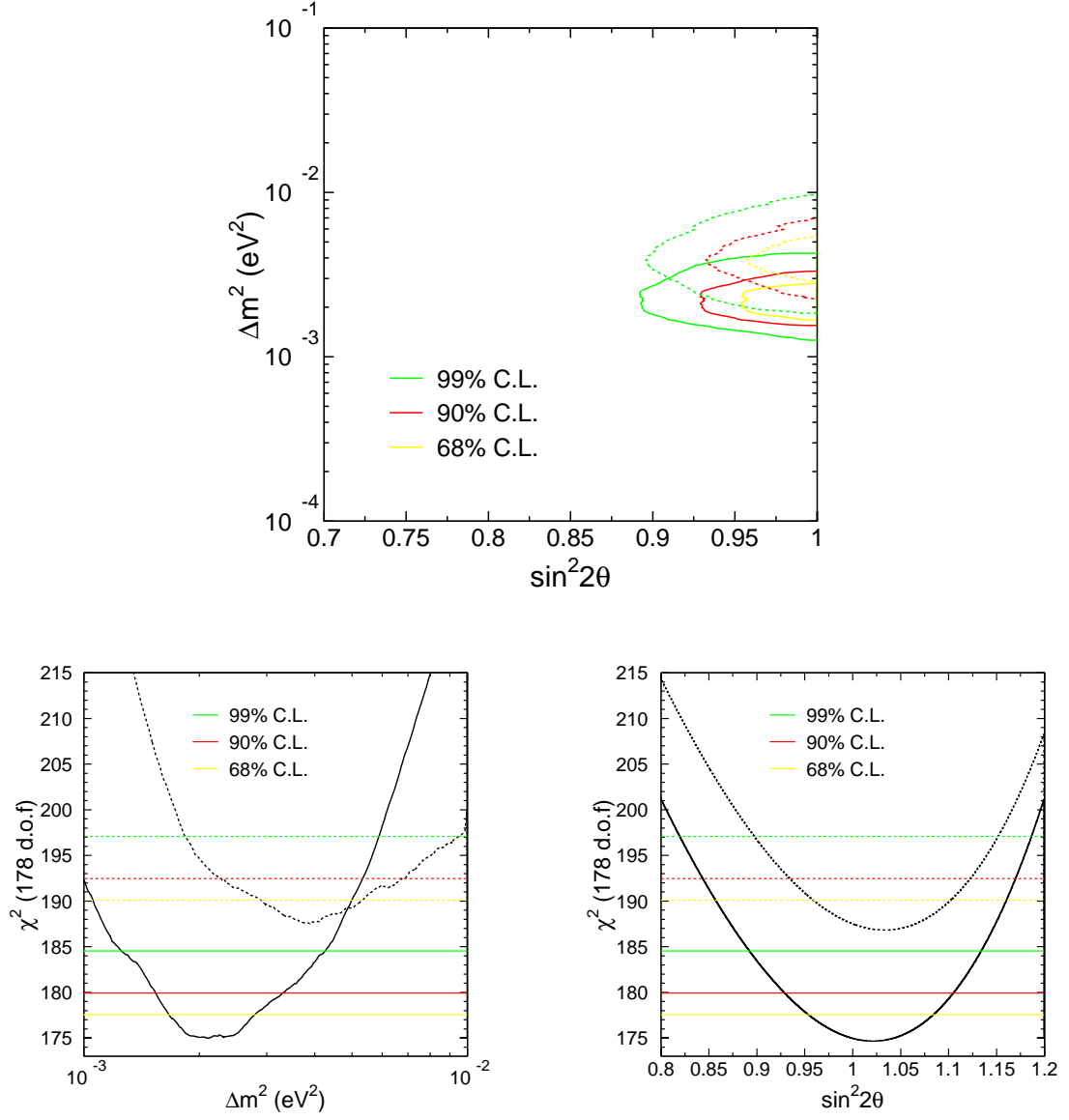Figure D.2: Contour plots for $\Delta m^2 \;\rightarrow\; \Delta m^2 \times \left(\frac{\rho}{\rho_o}\right)^2$ (no air pathlength), with a $\chi^2_{min} = 202.958/178$ d.o.f.
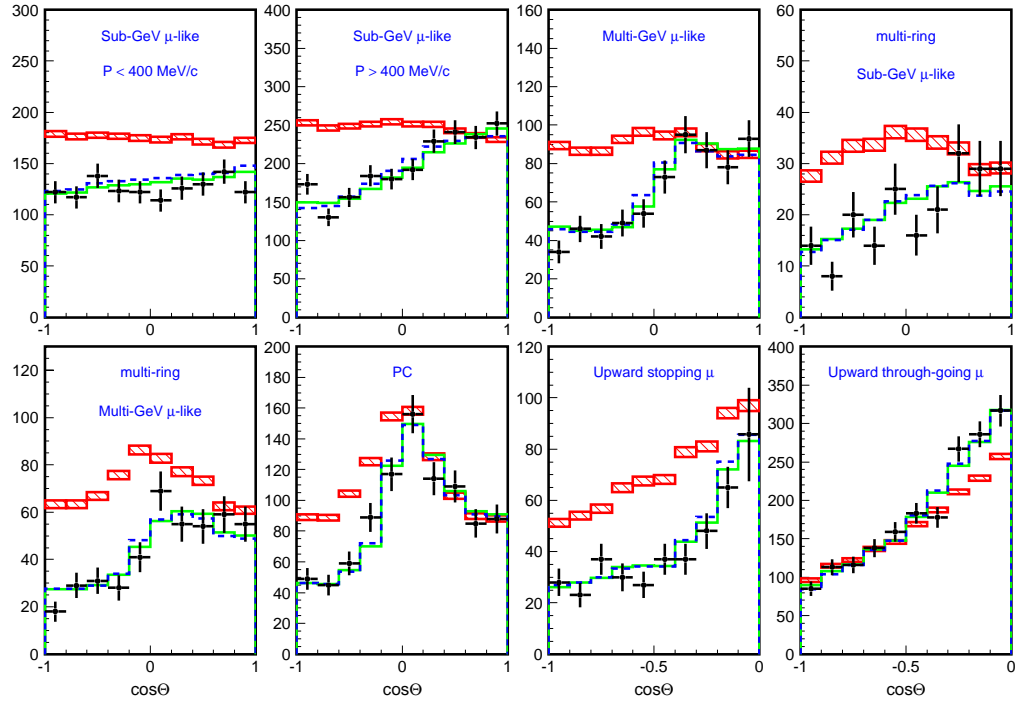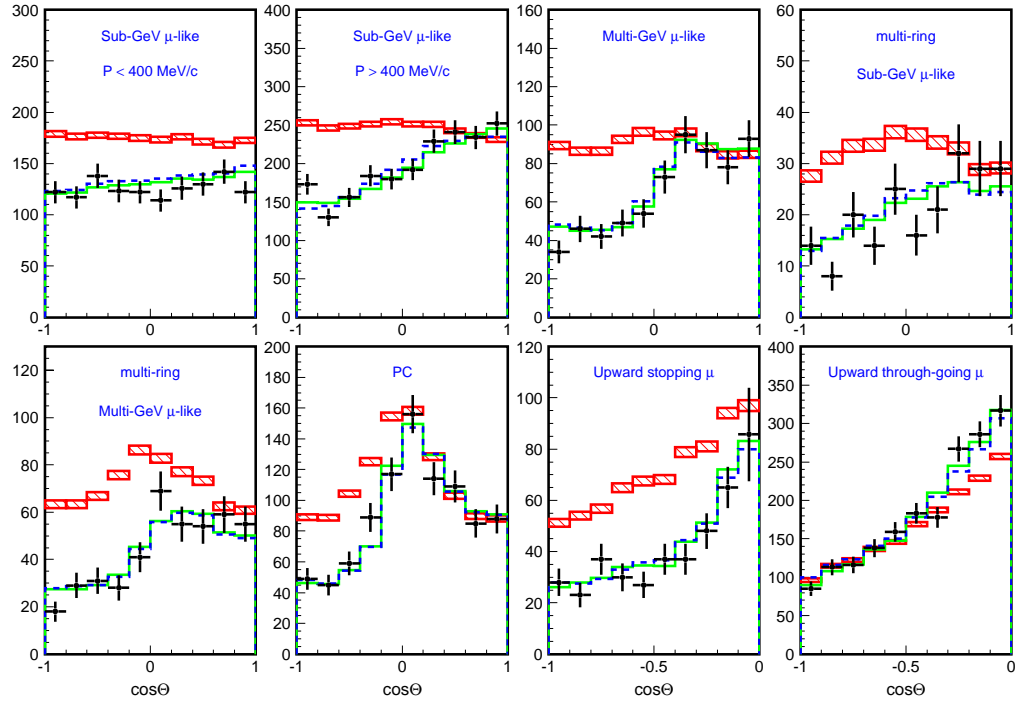
Figure D.3: Zenith angle bins for $\Delta m^2 \to \Delta m^2 \times \left(\frac{\rho}{\rho_o}\right)^{2/3}$ (no air pathlength).
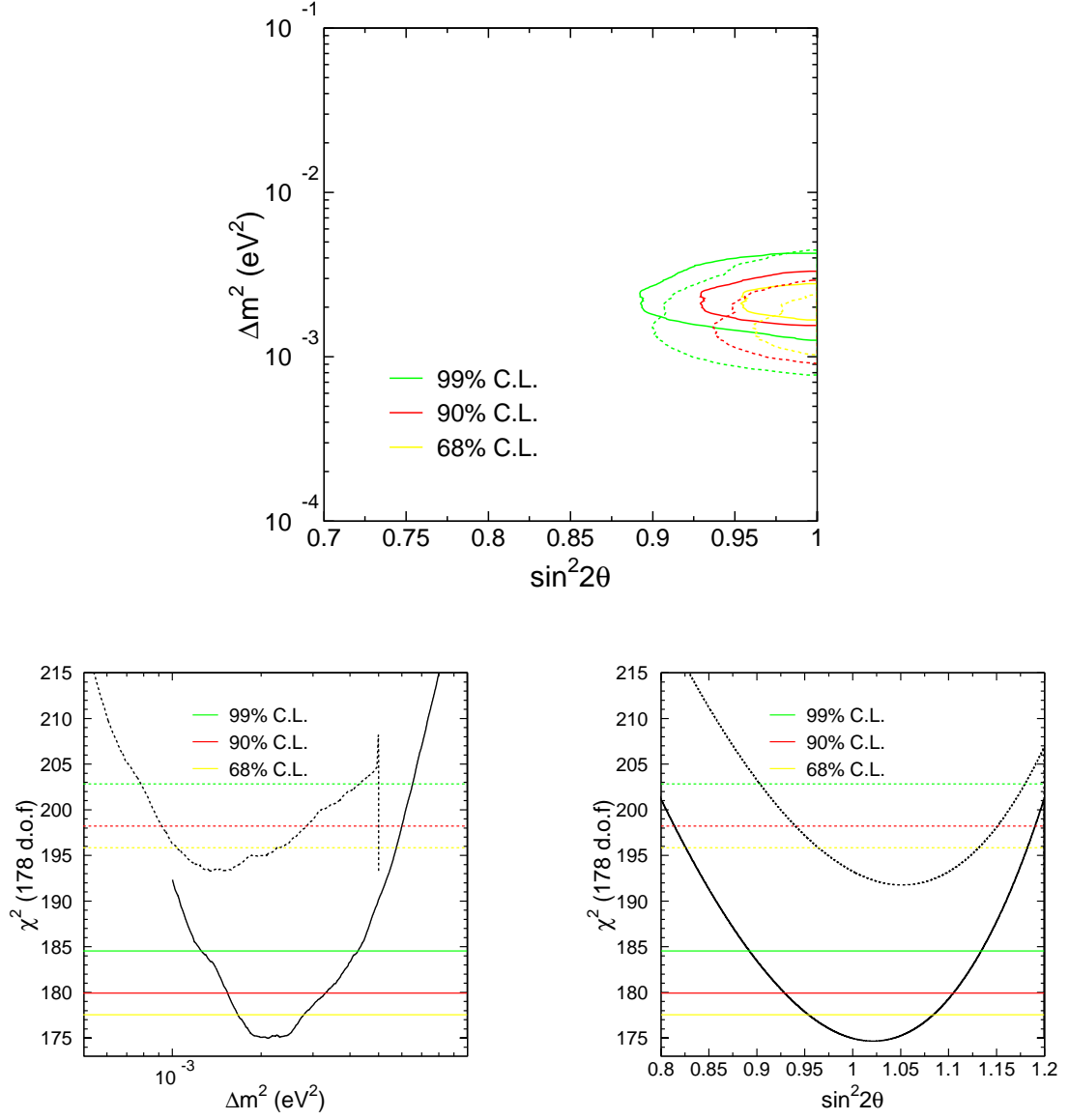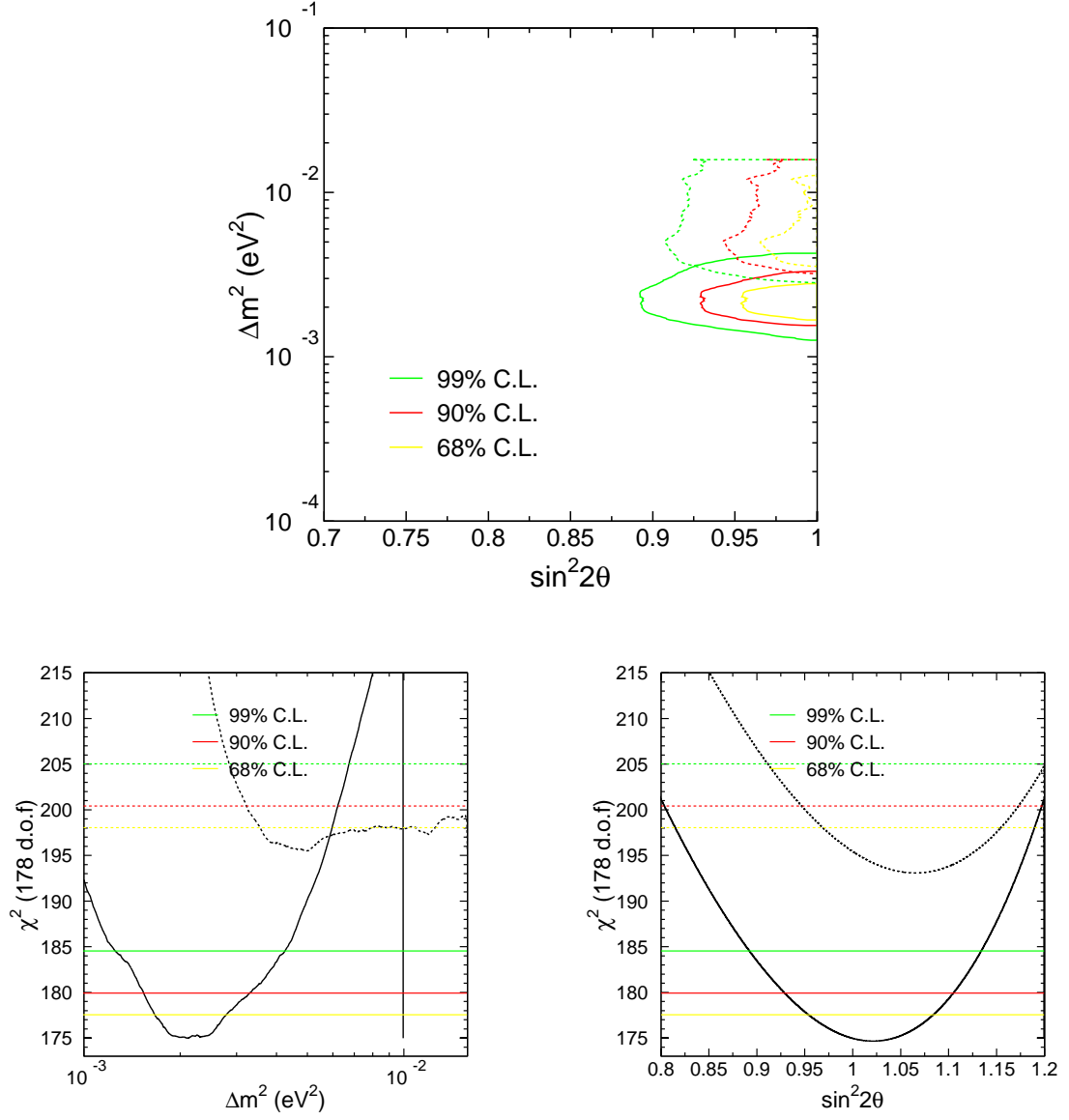
Figure D.4: Contour plots for $\Delta m^2 \rightarrow \Delta m^2 \times \left(\frac{\rho}{\rho_o}\right)^{2/3}$ (no air pathlength), with a $\chi^2_{min} = 193.281/178$ d.o.f.
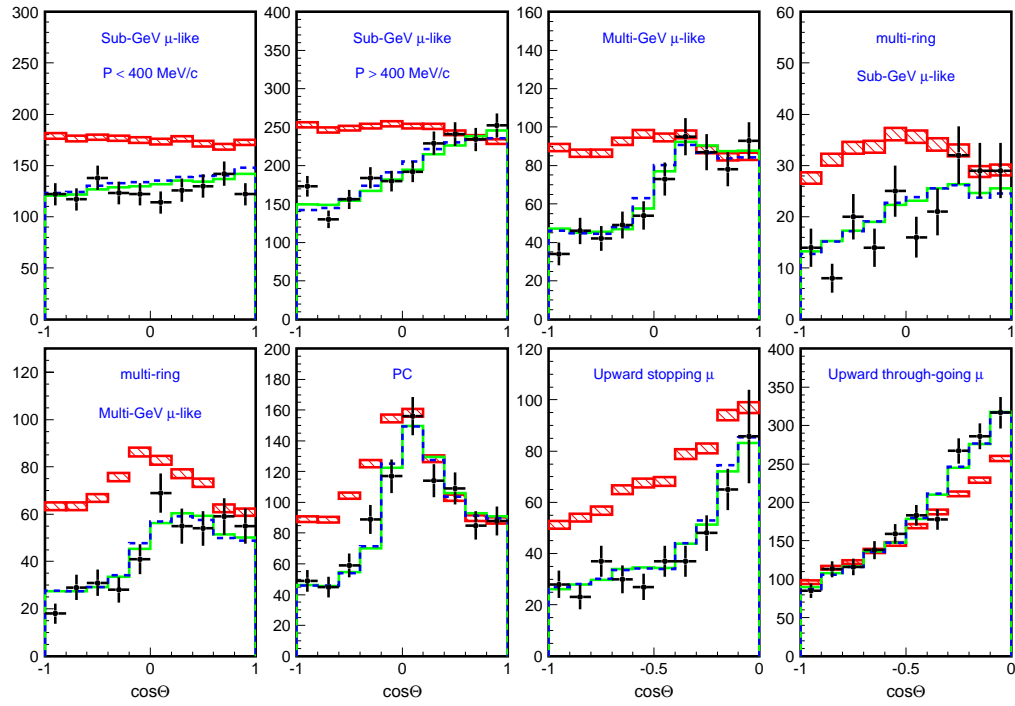
Figure D.5: Zenith angle bins for $\Delta m^2 \rightarrow \Delta m^2 \times \left(\frac{\rho}{\rho_o} \right)^{1/3}$ (no air pathlength).
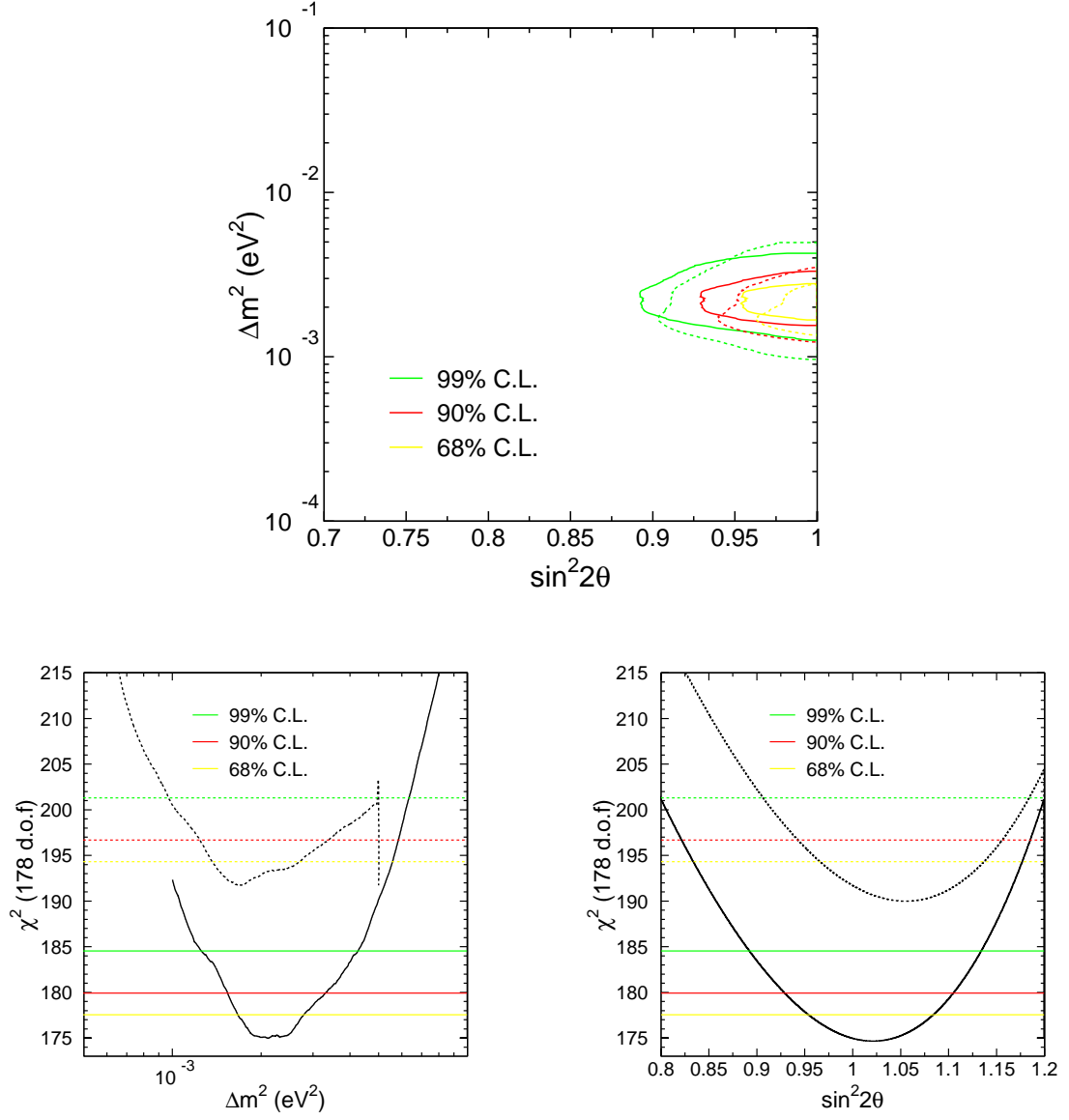
Figure D.6: Contour plots for $\Delta m^2 \rightarrow \Delta m^2 \times \left(\frac{\rho}{\rho_o}\right)^{1/3}$ (no air pathlength), with a $\chi^2_{min} = 191.728/178$ d.o.f.
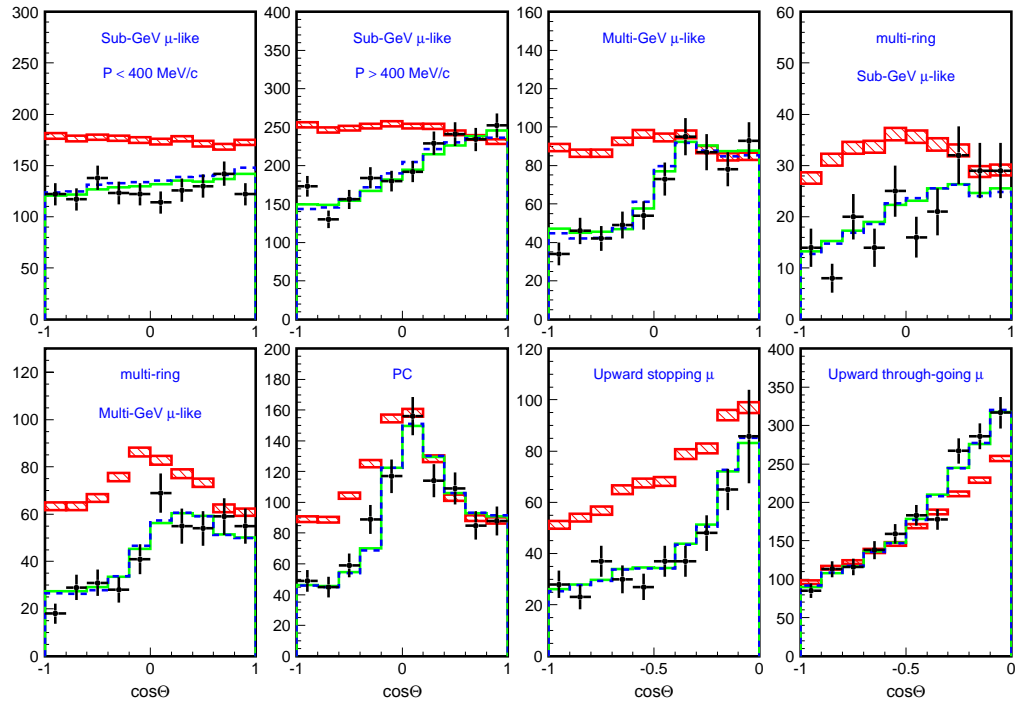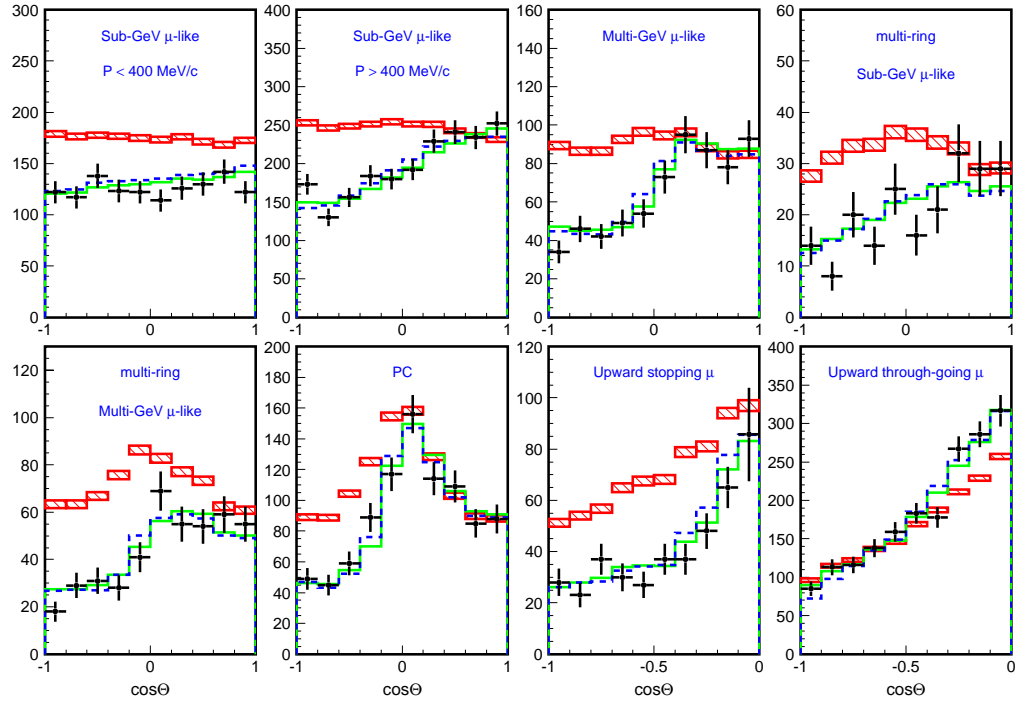
Figure D.7: Zenith angle bins for $\Delta m^2 \to \Delta m^2 \times \left(\frac{\rho}{\rho_o}\right)^{-1/3}$ (no air pathlength).
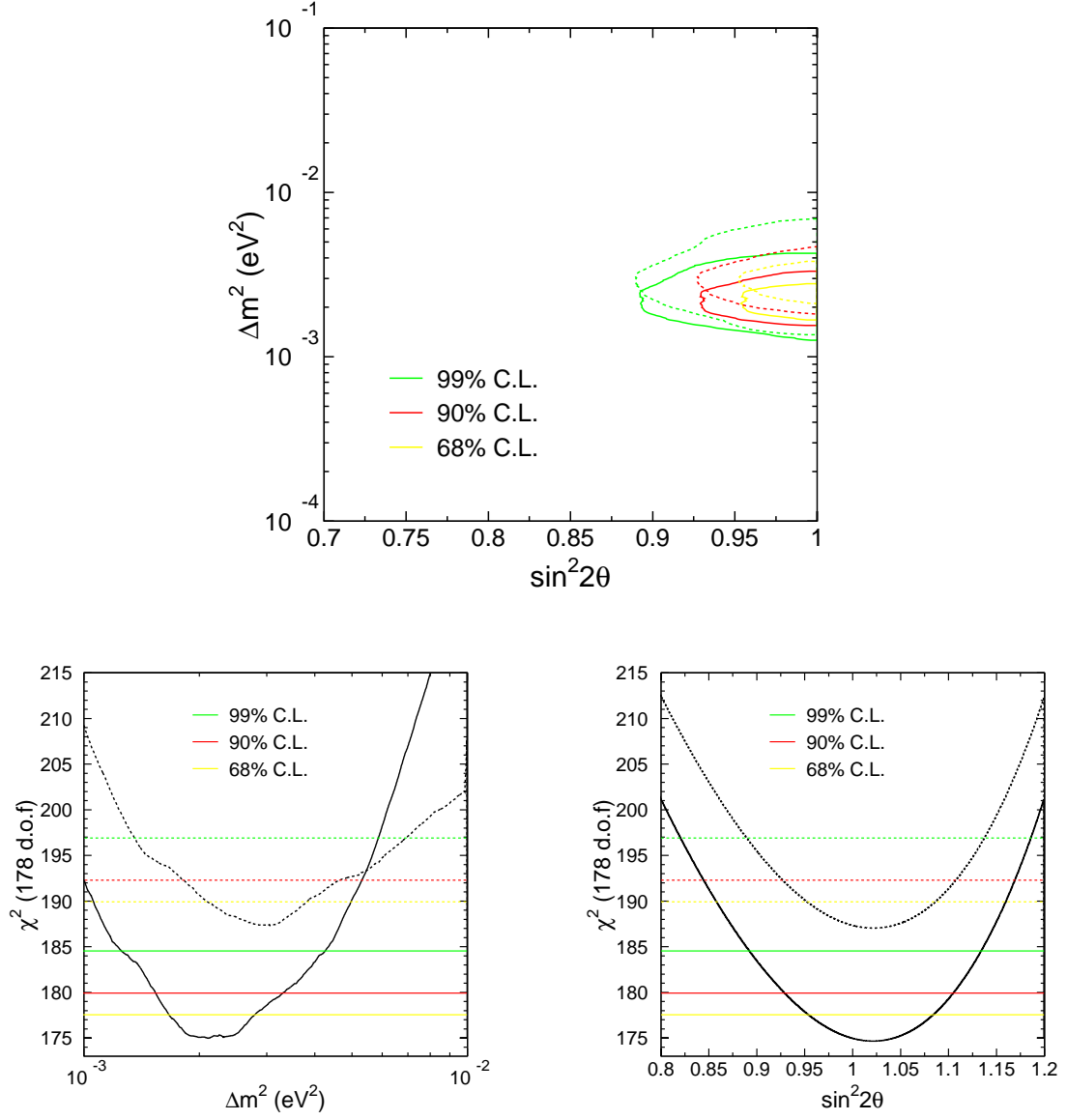
Figure D.8: Contour plots for $\Delta m^2 \rightarrow \Delta m^2 \times \left(\frac{\rho}{\rho_o}\right)^{-1/3}$ (no air pathlength), with a $\chi^2_{min} = 187.346/178$ d.o.f.
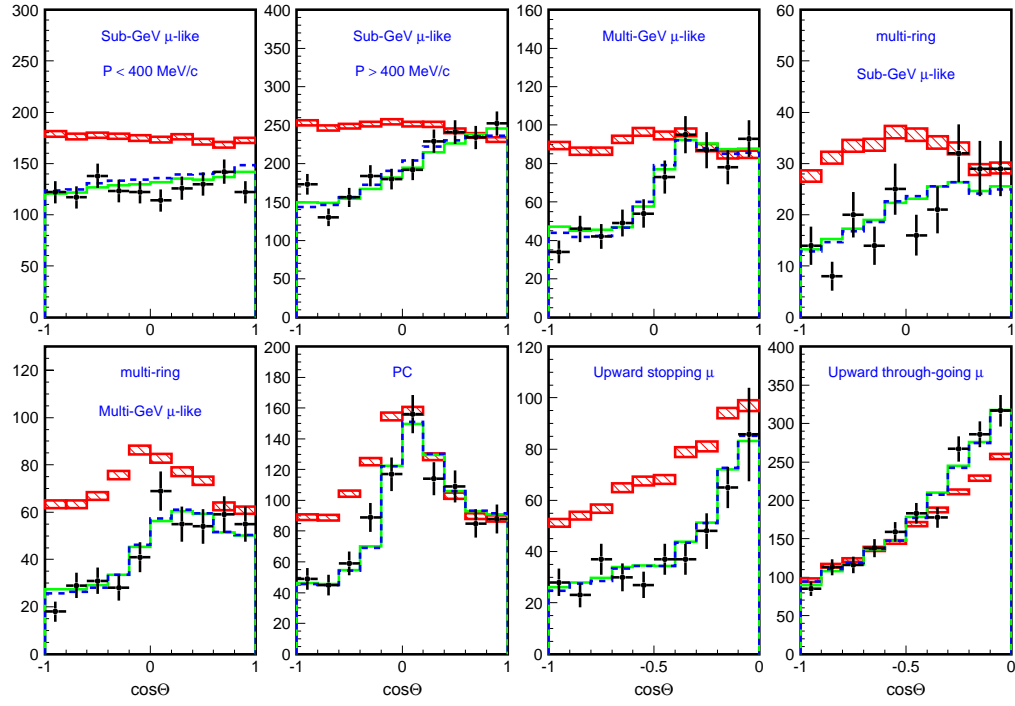
Figure D.9: Zenith angle bins for $\Delta m^2 \rightarrow \Delta m^2 \times \left(\frac{\rho}{\rho_o}\right)^{-2/3}$ (no air pathlength).
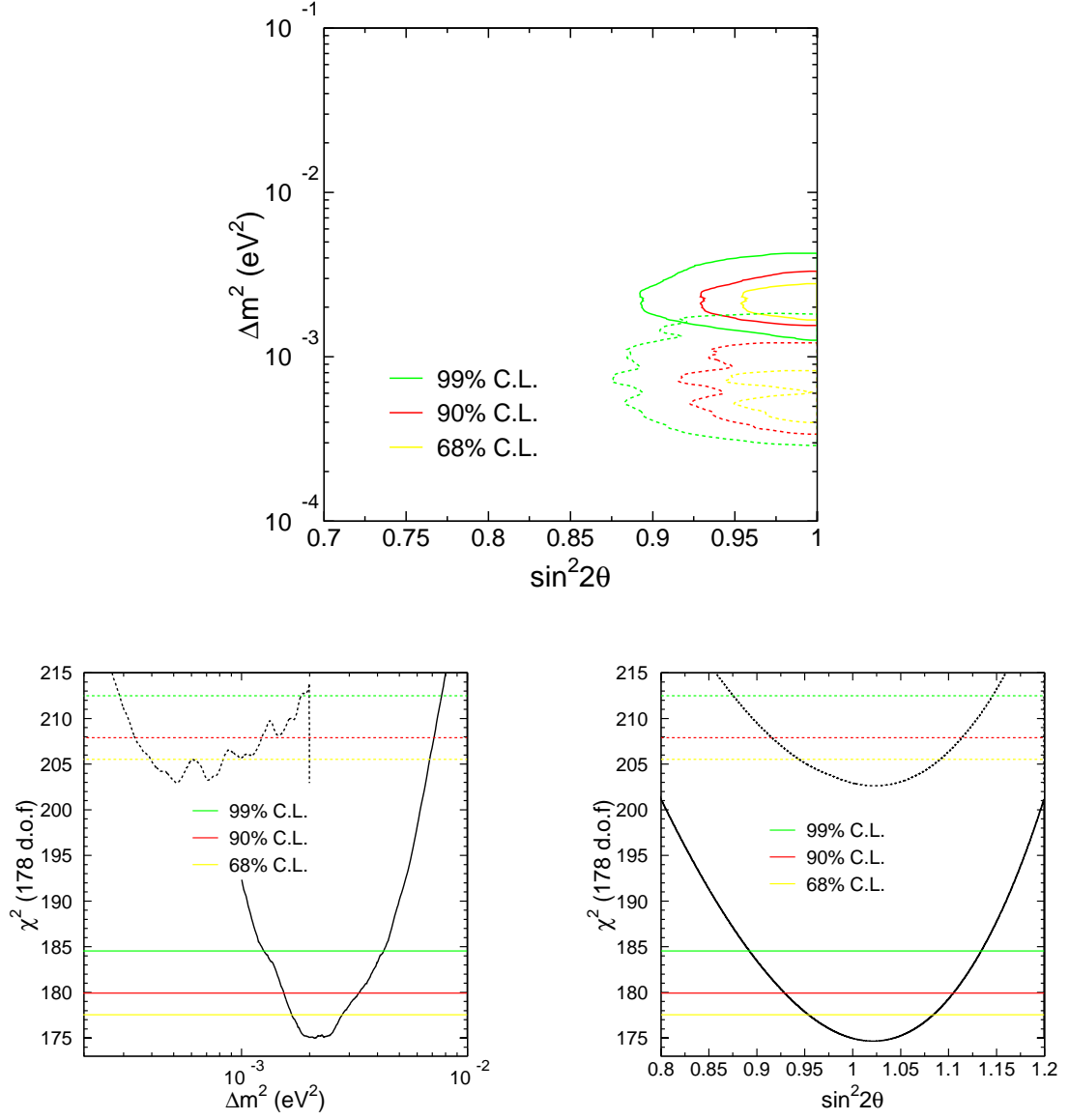
Figure D.10: Contour plots for $\Delta m^2 \rightarrow \Delta m^2 \times \left(\frac{\rho}{\rho_o}\right)^{-2/3}$ (no air pathlength), with a $\chi^2_{min} = 186.719/178$ d.o.f.
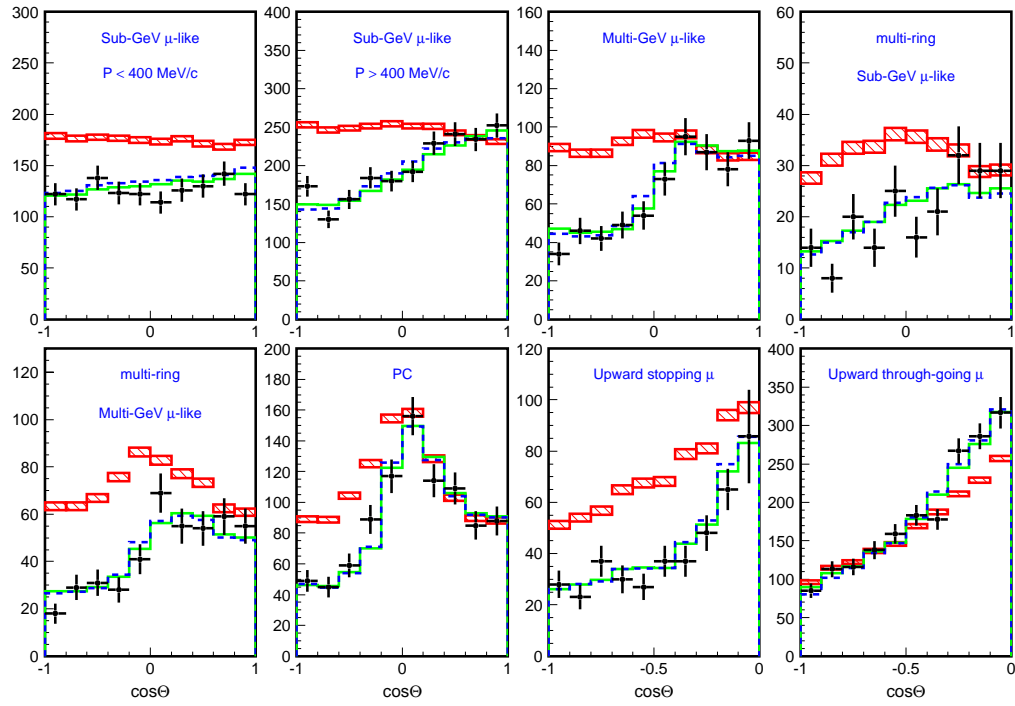
Figure D.11: Zenith angle bins for $\Delta m^2 \to \Delta m^2 \times \left(\frac{\rho}{\rho_o}\right)^{-1}$ (no air pathlength).

Figure D.12: Contour plots for $\Delta m^2 \rightarrow \Delta m^2 \times \left(\frac{\rho}{\rho_o}\right)^{-1}$ (no air pathlength), with a $\chi^2_{min} = 187.528/178$ d.o.f.

Figure D.13: Zenith angle bins for $\Delta m^2 \to \Delta m^2 \times \left(\frac{\rho}{\rho_o}\right)^{-2}$ (no air pathlength).

Figure D.14: Contour plots for $\Delta m^2 \rightarrow \Delta m^2 \times \left(\frac{\rho}{\rho_o}\right)^{-2}$ (no air pathlength), with a $\chi^2_{min} = 195.464/178$ d.o.f.

Figure D.15: Zenith angle bins for $\Delta m^2 \rightarrow \Delta m^2 \times \left(\frac{\rho}{\rho_o}\right)^2$ (with air pathlength).
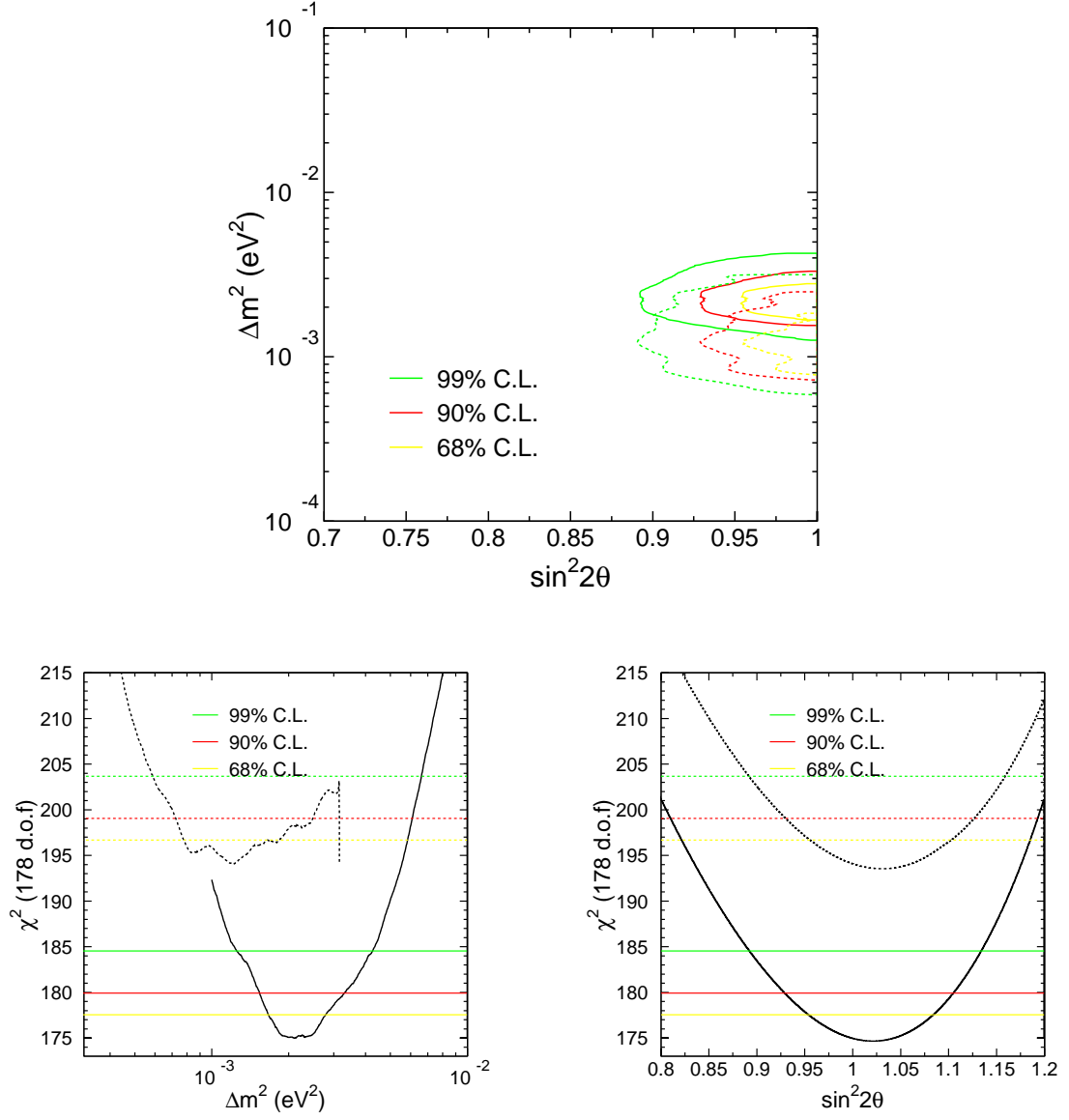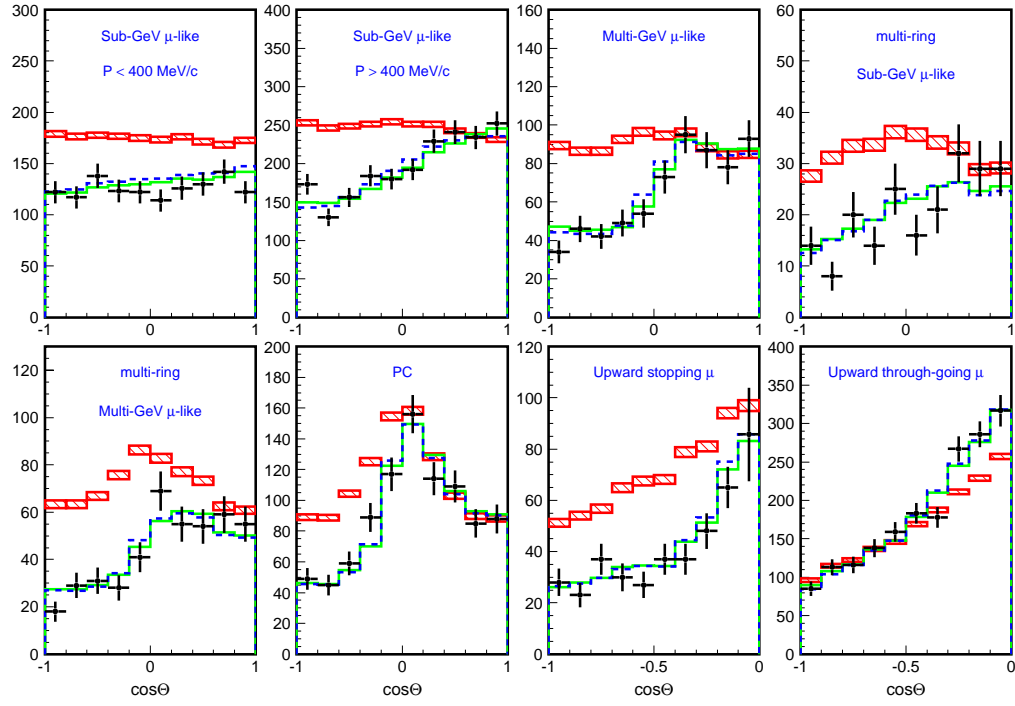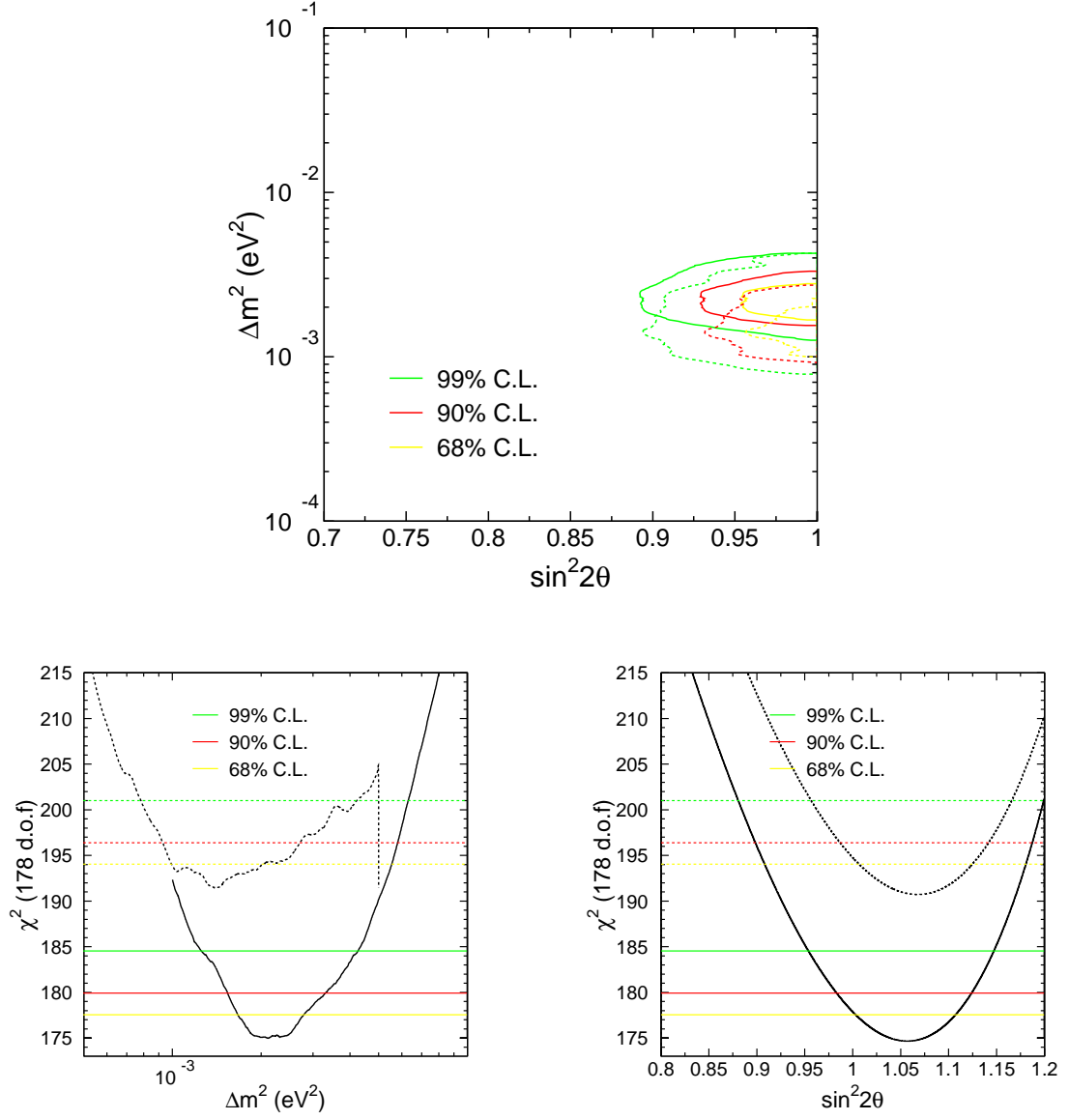
Figure D.16: Contour plots for $\Delta m^2 \rightarrow \Delta m^2 \times \left(\frac{\rho}{\rho_o}\right)^2$ (With Air Pathlength), with a $\chi^2_{min} = 202.937/178$ d.o.f.

Figure D.17: Zenith angle bins for $\Delta m^2 \rightarrow \Delta m^2 \times \left(\frac{\rho}{\rho_o}\right)$ (with air pathlength).

Figure D.18: Contour plots for $\Delta m^2 \rightarrow \Delta m^2 \times \left(\frac{\rho}{\rho_o}\right)$ (With Air Pathlength), with a $\chi^2_{min} = 194.102/178$ d.o.f.

Figure D.19: Zenith angle bins for $\Delta m^2 \rightarrow \Delta m^2 \times \left(\frac{\rho}{\rho_o}\right)^{2/3}$ (with air pathlength).

Figure D.20: Contour plots for $\Delta m^2 \rightarrow \Delta m^2 \times \left(\frac{\rho}{\rho_o}\right)^{2/3}$ (with air pathlength), with a $\chi^2_{min} = 191.455/178$ d.o.f.
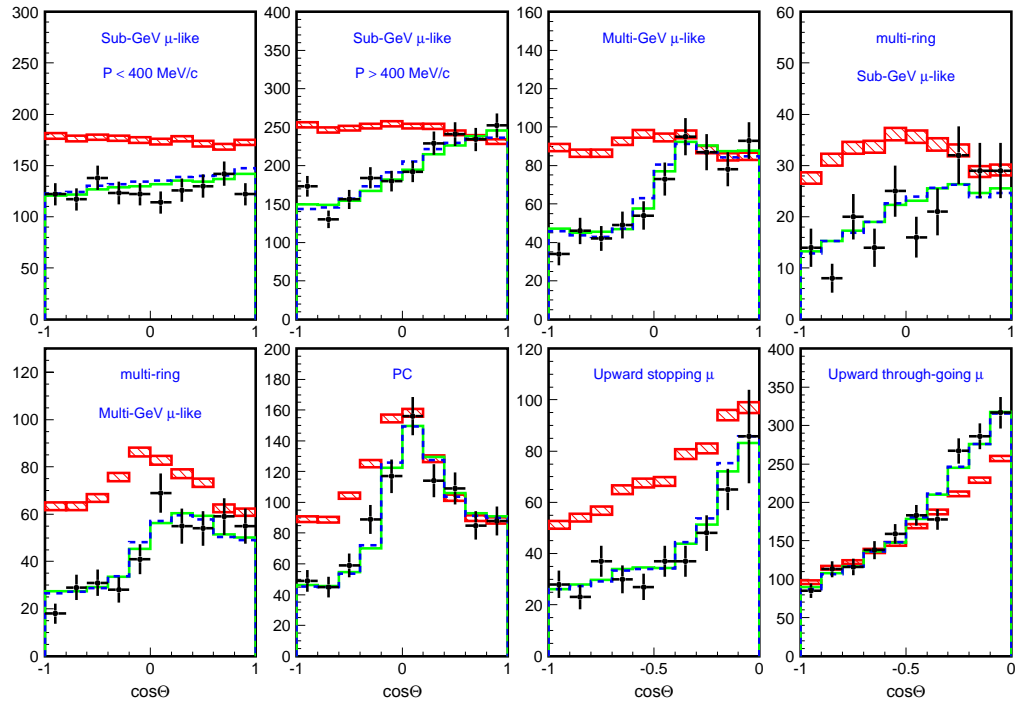
Figure D.21: Zenith angle bins for $\Delta m^2 \rightarrow \Delta m^2 \times \left(\frac{\rho}{\rho_o}\right)^{1/3}$ (with air pathlength).
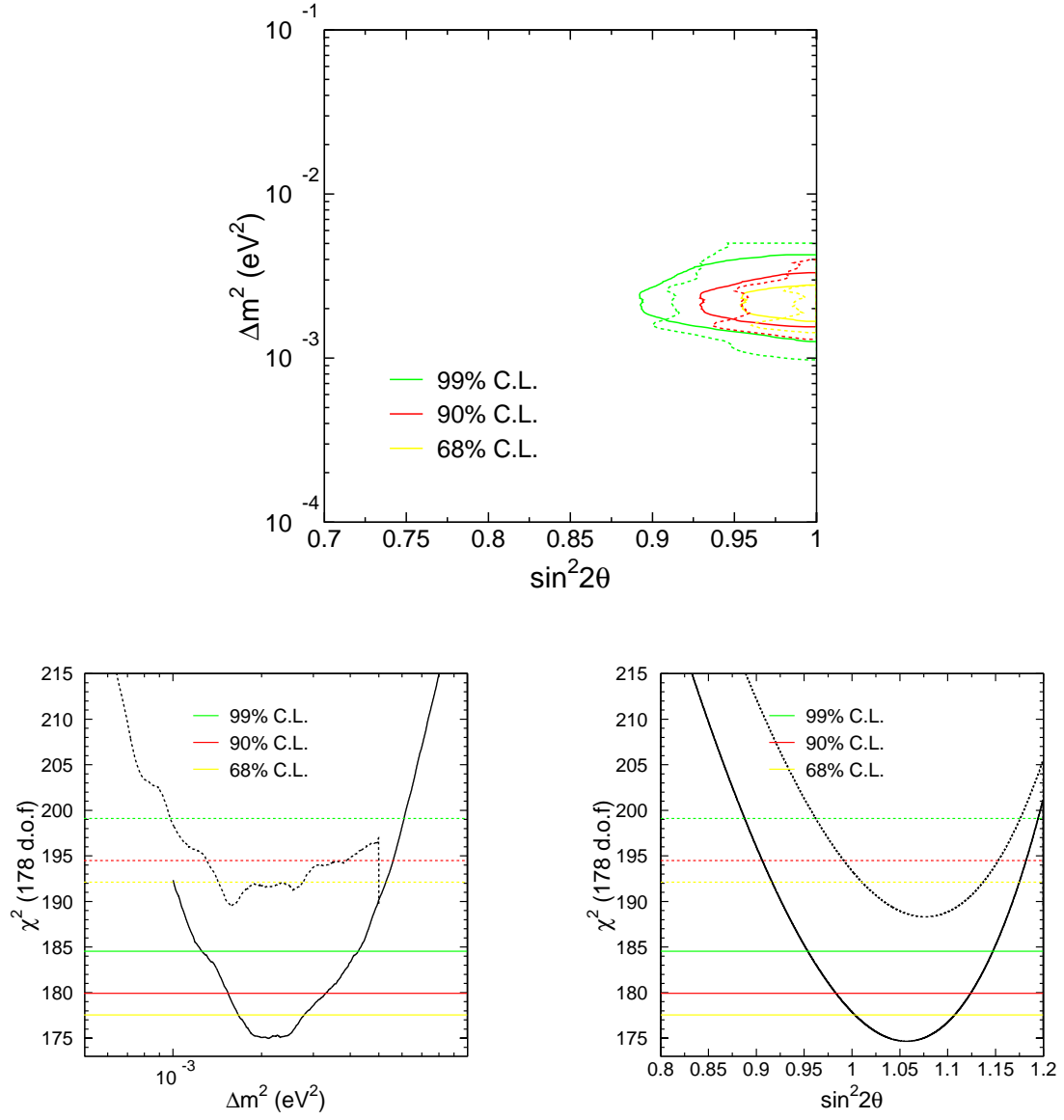
Figure D.22: Contour plots for $\Delta m^2 \rightarrow \Delta m^2 \times \left(\frac{\rho}{\rho_o}\right)^{1/3}$ (with air pathlength), with a $\chi^2_{min} = 189.542/178$ d.o.f.
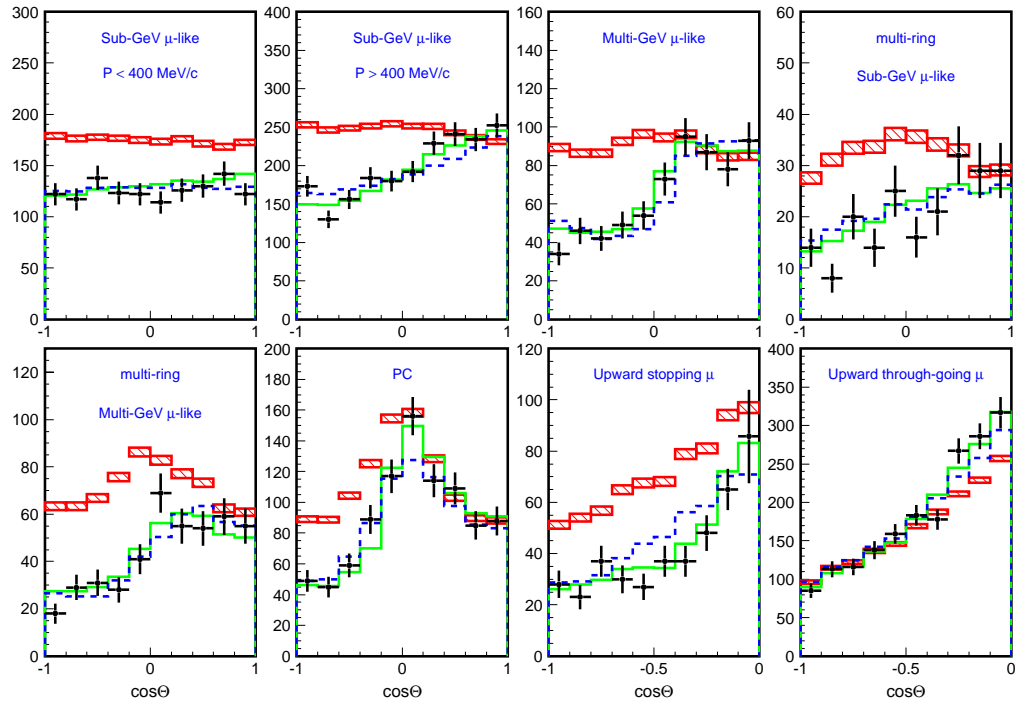
Figure D.23: Zenith angle bins for $\Delta m^2 \rightarrow \Delta m^2 \times \left(\frac{\rho}{\rho_o}\right)^{-1/3}$ (with air pathlength).
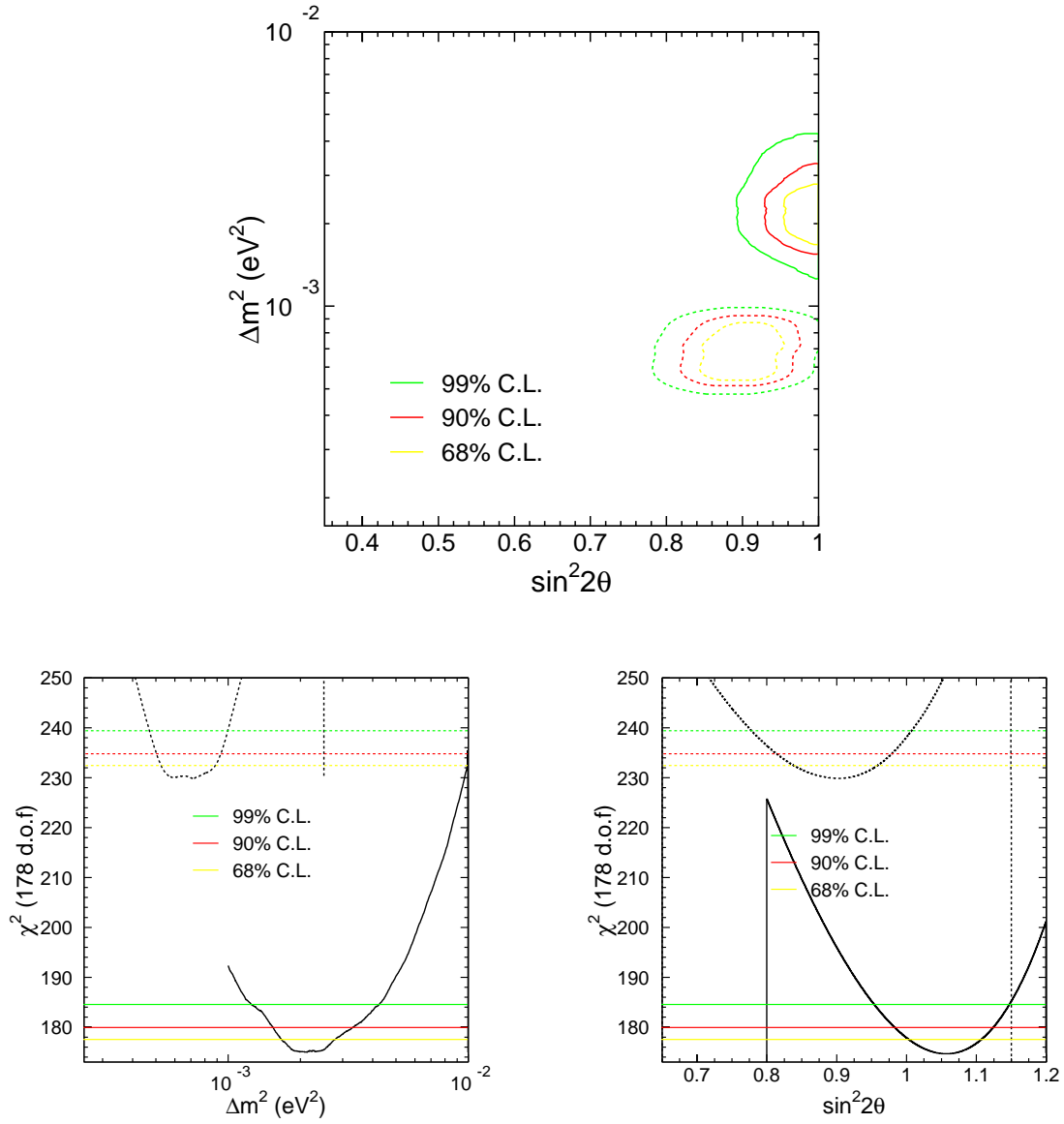
Figure D.24: Contour plots for $\Delta m^2 \rightarrow \Delta m^2 \times \left(\frac{\rho}{\rho_o}\right)^{-1/3}$ (with air pathlength), with a $\chi^2_{min} = 229.867/178$ d.o.f.

VITA

Kiyoshi Keola Shiraishi was born on October 3rd, 1978, to Larry and Amy Shiraishi. Raised in Pearl City, Hawaii and educated in its public schools, "Yosh" realized his love for learning and managed to scrape by as a valedictorian from Pearl City High School in 1996. He would go on to receive double B.S. degrees in Physics and Mathematics from the University of Puget Sound in 2000, and a M.S. degree in Physics from the University of Washington in 2003. To his great surprise he is now leaving with a Ph.D. in 2006. After completing all of the schooling he could, Kiyoshi now begins the next phase of his life a bit fearful but mostly wide-eyed to a life outside of academia for the first time.